Advances in Acoustics and Vibration

Advanced Materials for Applications in Acoustics and Vibration

Guest Editors: Yehia A. Bahei-El-Din and Mohammad Tawfik

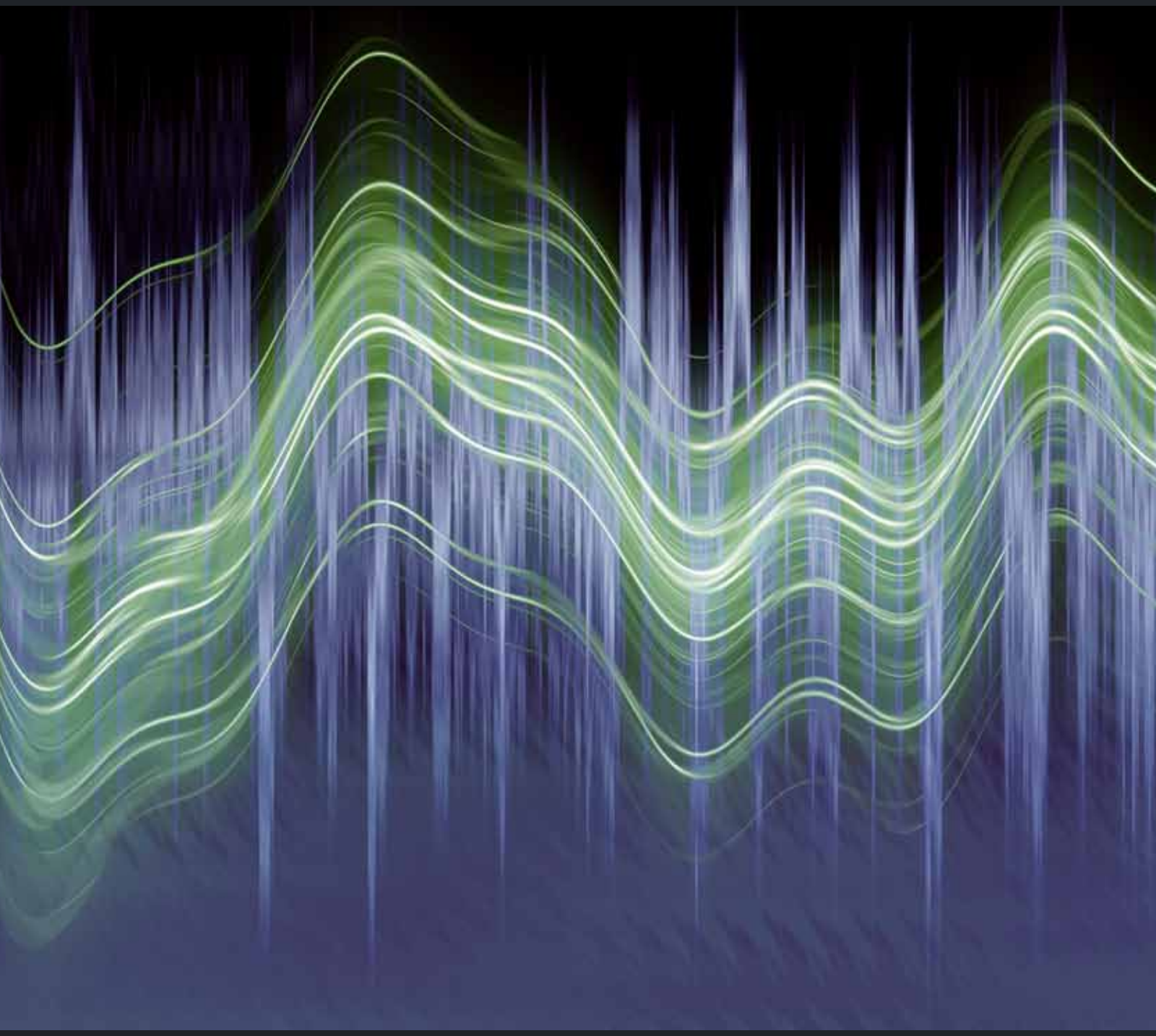

Advanced Materials for Applications in Acoustics and Vibration

Advanced Materials for Applications in Acoustics and Vibration

Guest Editor: Yehia A. Bahei-El-Din and Mohammad Tawfik

Editorial Board

Contents

Hindawi Publishing Corporation
Advances in Acoustics and Vibration
Volume 2009, Article ID 656741, 1 page
doi:10.1155/2009/656741

Editorial
Advanced Materials for Applications in Acoustics and Vibration

Yehia A. Bahei-El-Din[1] and Mohammad Tawfik[2]

[1] *Centre for Advanced Materials, The British University in Egypt, El-Shorouk City 11837, Cairo, Egypt*
[2] *Noon for Research and Development, Cairo, Egypt*

Correspondence should be addressed to Yehia A. Bahei-El-Din, ybahei@bue.edu.eg

Received 8 November 2009; Accepted 8 November 2009

Research in advanced materials is progressing on many fronts with significant developments in composite, smart and nano-scale materials. Industrial applications have also benefited from advances in material science and engineering. Substantial work, however, lies ahead to integrate advanced materials in engineering applications. One such application which has significant impact on both the economy and quality of life is acoustics and vibrations of materials and mechanical systems. Generally, however, materials and dynamics are considered by different groups with little or no interaction. The purpose of the International Conference on Advanced Materials for Application in Acoustics and Vibration (AMAAV)—held in Cairo, Egypt from January 4 to 6, 2009—was to bridge the gap between research and application in the significant field of dynamics, with emphasis on materials, by bringing together regional and international researchers and engineers to present and discuss recent developments in utilizing advanced materials in applications related to acoustics and vibration. It provided a forum for disseminating the latest research findings in material development, modeling, and testing under service loads and environments, derived from real life applications in which acoustics and vibrations play a major role in their design and performance.

This special issue of Advances in Acoustics and Vibration contains papers contributed to AMAAV conference. The contributions contained in this issue address both purely dynamic problems and dynamics of/advanced materials. In the latter category, Buonsanti et al. investigate detection of defects in carbon/epoxy composites using ultrasonic testing, and Eldalil and Baz study active control of cylindrical shells subjected to internal pressure pulse using piezoelectric materials. Vibration problems are investigated in four contributed papers; Buonsanti et al. considered the effect of railway-induced vibrations on buildings; Di Mino et al. also considered vibrations caused by railways and investigated the role of open trenches in their reduction; Eldalil and Baz studied the effect of periodic stiffeners on the dynamic stability of cylindrical shells subjected to internal pressure pulse; Patwari et al. presented a method for dynamic characterization of vertical machining. In acoustics, Ivansson considered the design of acoustic frequency insulators using phononic crystals.

The time and effort spent by the authors in participating in the meeting and preparing the manuscripts for this special issue is greatly appreciated.

Yehia A. Bahei-El-Din
Mohammad Tawfik

Hindawi Publishing Corporation
Advances in Acoustics and Vibration
Volume 2009, Article ID 647658, 8 pages
doi:10.1155/2009/647658

Research Article

Evaluation of Defects in Multilayer Carbon Fibre Epoxy for Aeronautics Applications

M. Buonsanti,[1] M. Cacciola,[2] S. Calcagno,[2] G. Megali,[2] F. C. Morabito,[2] D. Pellicanò,[2] and M. Versaci[2]

[1] *MECMAT Department, Faculty of Engineering, University "Mediterranea" of Reggio Calabria, Via Graziella Feo di Vito, 89100 Reggio Calabria, Italy*
[2] *DIMET Department, Faculty of Engineering, University "Mediterranea" of Reggio Calabria, Via Graziella Feo di Vito, 89100 Reggio Calabria, Italy*

Correspondence should be addressed to M. Cacciola, matteo.cacciola@unirc.it

Received 23 February 2009; Accepted 3 June 2009

Recommended by Mohammad Tawfik

Production of carbon fibre reinforced polymers is an elaborate process unfree from faults and problems. Problems during the manufacturing, such as plies' overlapping, can cause flaws in the resulting material, so compromising its integrity. Compared with metallic materials, carbon epoxy composites show a number of advantages. Within this framework, ultrasonic tests are effective to identify the presence of defects. In this paper a Finite Element Method approach is proposed for evaluating the most effective incidence angle of an ultrasonic probe with regard to defects' identification. According to our goal, the analysis has been carried out considering a single-line plane emitting source varying the probe angle of inclination. The proposed model looks promising to specially emphasize the presence of delaminations as well as massive breaking in a specimen of multilayer carbon fibre epoxy. Subsequently, simulation parameters and results have been exploited and compared, respectively, for a preliminary experimental in-lab campaign of measurements with encouraging results.

1. Introduction

Within the framework of the aeronautic industry, the attention is focused on the quality check of the manufacture process, especially for the composite materials used in energy production (nuclear plants), transportation (aeronautic), workpiece manufacturing, and so forth. Composite materials, in particular Carbon Fibre Epoxy (CFRP/E), are also applied to various fields of aeronautic industry. Particularly, multi-layers CFRP/E are the basic product for constructing main parts of modern airplanes, which are subjected to a continuous degradation. Mechanic solicitations and atmospheric agents are responsible for a relatively rapid degradation of airplanes' structures. Therefore, they must be produced in an almost perfect state, in order to not introduce other dangerous risk factors. The manufacture process of CFRPs can induce a number of characteristic flaws, for example, delaminations, inclusions, and porosities. Therefore, it is absolutely necessary to carry out cheap tests of conformity and integrity. In particular Ultrasonic Testings (UTs) are useful for our aims, as it is possible to easily analyze even highly thick metallic as well as nonmetallic materials, with a good resolution and a remarkable operative versatility. The paper is structured as follows. Section 2 describes physical characteristics of CFRP/E materials. Section 3 is an overview of UTs technique. Section 4 presents the Finite Element Analysis (FEA) approach. Section 5 illustrates the results of the proposed approach to detect the kind of defect.

2. Physical Characteristics and Problems in CFRP/E

CFRPs are widely used in military and aerospace industries and in such applications in which high costs are justified by the increased performance of the final product (e.g., and racing cars, high-end automotive products, aerospace). Two major advantages are offered by CFRPs. First of all, high

mechanical properties are offered in terms of high stiffness-to-weight and resistance to weight ratios. The Ashby charts presented in Figure 1 show that fibre-reinforced materials in general, and particularly CFRP/E, have a combination of high mechanical properties in terms of stiffness, strength, and fracture toughness. If compared with engineering alloys, that have specific stiffness similar to CFRP/Es, higher specific strength and higher specific fracture toughness are offered. Moreover, if CFRP/Es are compared to engineering ceramics, a better fracture toughness is evident. Compared with common engineering materials, such as steels or cast irons, fibre-reinforced polymers present lower absolute values for Young modulus and tensile strength, but they offer much better specific properties (they have ten times smaller density). However, in terms of fracture toughness, the values are reasonably similar. The second main advantage offered by fibre-reinforced composites concerns the possibility to prepare customized materials in relation to final product requirements. In composite materials, the shape, the thickness, and the mechanical properties of the specimen can be controlled in order to satisfy specific requirements. Material form and fibre orientations can be chosen in relation to the design process and the material can be minutely controlled, minimizing weight and optimizing overall properties. If the stresses encountered by a load-bearing composite component in service are known, it is possible to design the fibre in order to optimize the stiffness-to-weight and strength-to-weight parameters of the component [1].

As pointed out in the introduction section, in recent years there is a growing interest in the use of low-cost heavy carbon fibre tows in textile composite applications, including Multi-Layers Fabrics (MLFs). The mechanical properties of these materials depend on the obtained crystallization. It depends on the peak value of the temperature and the speed during its manufacturing. Generally speaking, a brief final treatment at a temperature of 3000 °C increases significantly the fibres quality, increasing the value of Young modulus. It is possible to increase the strength and elastic modulus of these fibres through a hot-stretching. In this way, we obtain a poly-crystalline structure of carbon with the following excellent mechanical properties:

(i) tensile (R_m) = 1980 – 2570 N/mm^2

(ii) elastic module (E) = 220000 – 400000 N/mm^2

(iii) density (γ) = 1.75 Kg/dm^3.

The use of "nude" fibres does not allow to achieve structural parts subjected to a tension variable field. For this reason, the fibres are intimately linked (impregnated) with resins, which constitutes the previously introduced matrix.

The elementary structure of carbon fibres has a diameter range from 7 to 10 μm: typically the structure consists of filaments and about 3000 fibres compose a single filament. The carried out structure can be ordered with parallel filaments in order to form "unidirectional" specimen. Frequently, in aeronautic industry, preimpregnated fibres are usually purchased; its thickness goes from 0.1 to 0.3 mm. In order to have a good resistance with a tension variable field, the prefilled is layered with different orientation, forming a structure called "laminate". The thickness of the laminate goes from 10 to 20–25 mm.

The mechanical properties of a laminate structure are typically lower than "nude" fibres, and in particular:

(i) tensile (R_m) = 1270 – 1370 N/mm^2

(ii) elastic module (E) = 150000 – 200000 N/mm^2

(iii) density (γ) = 1.5 – 1.57 Kg/dm^3.

Composite materials are also subject to the presence of defects compromising the structural integrity of the same materials and, consequently, of aeronautic vehicles.

(i) *Delamination*. separation between two close layers along a horizontal plane; it is due to existing (air) or created (contamination) gas during the polymerization. Grouped little delaminations (resembling to flattened pores), distributed at different depths, are sometimes called microdelaminations.

(ii) *Inclusion* foreign material (e.g., the one used for the bag) accidentally left in the part during the lay-up.

(iii) *Porosity*. spherical/elliptical microvoid distributed within a volume or in parallel plane to a lay-up. Generally it is induced by incorrect pressure and temperature gradients during polymerization.

These factors may affect the performance of the composite material. However, the entity of the risk depends on the geometry of structure and on the effective localization and orientation of the defects. Similarly to metal structures, aeronautic composite structures are formed by several components assembled through pasting and screwing. This manufacturing techniques can produce the presence of defects, such as abscission between layers (due to pasting) or drilling (due to screwing). The presence of this kind of defects can cause the reduction of cohesion and adhesion resistance. Thus, the final properties of composite materials are intrinsically linked to the manufacturing process. In this framework, a good compromise between resistance, weight, and cost of aircraft structures is the main goal. In the next section the Ultrasound technique and the Finite Elements approach will be shown in order to inspect multi-layer plates, with oriented layer at 0°, 90°, 0° respectively, and reinforced with epoxy resin.

3. The Principle of the Ultrasound Method

When ultrasound method is used for imaging, one or two directional tones are transmitted via a transducer into the air. Subsequently, the reflections of the acoustic waves are recorded and exploited in order to determine various properties of the object under examination. Therefore, the propagation of directed single tone ultrasound is examined. This section presents a detailed background on acoustic propagation, focusing on the propagation of single tone plane waves. For this purpose, it is worthwhile to resume the fundamentals of particle oscillation governing the transmission of acoustic waves through a medium. This section gives a general overview of the physical equations that govern both

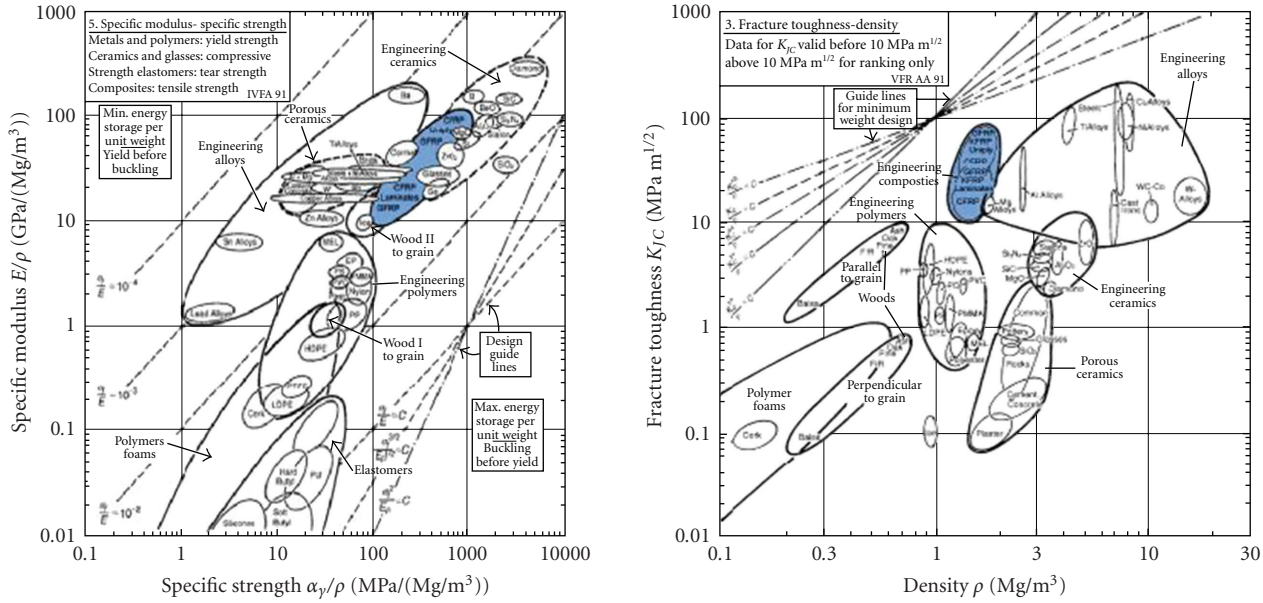

(a) Specific Young modulus is plotted versus specific strength.

(b) Fracture toughness is plotted versus density.

Figure 1: Ashby Material Property.

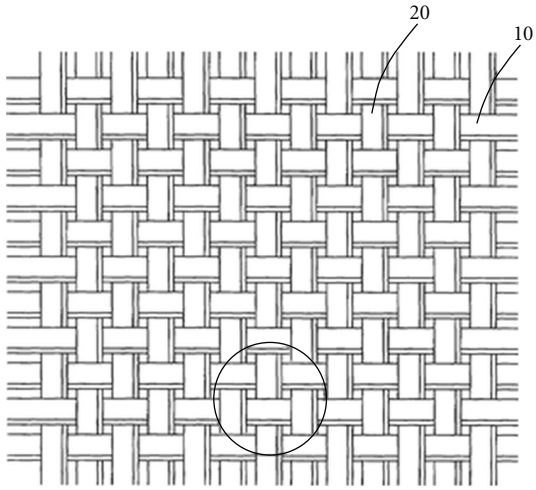

Figure 2: Example of the architecture of MLFs. Layers of unidirectional oriented fibres, made of adjacent spread tows, are stacked together automatically and then fixed with stitching.

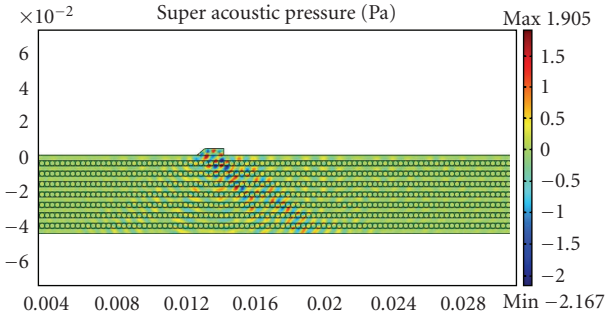

Figure 3: FEM-based implemented model.

linear and nonlinear wave motion through the air. It presents the partial differential equation that describes the pressure variation of a medium when a single frequency acoustic wave propagates.

Acoustic waves are pressure disturbances in the form of vibrational waves that propagate through a compressible medium. These vibrational waves displace the molecules of the medium from their quiescent point, after which a restoring elastic force pulls the molecules back. This elastic force, along with inertia, causes the oscillation of the molecules, allowing acoustic waves propagation.

The oscillatory motion is analogous to the motion of a spring when it is displaced from its rest position, while the propagation of the wave is analogous to the movement of a wave down a piece of string. The most well-known acoustic waves are those of sound. The audible frequency range for an average person is included from 20 Hz to 20 kHz; the range above the audible (greater than 20 kHz) is called the ultrasonic region. When we consider planar waves we mean that each acoustic variable has constant amplitude on any given plane perpendicular to the direction of propagation. This assumption greatly simplifies the derivations of acoustic equations and relationships. It is valid in most experimental situations because wave fronts of any divergent wave in a homogeneous medium become approximately planar, when sufficiently far from the source:

$$R = \frac{l^2}{\lambda}, \tag{1}$$

where l is the length of the source, λ is the wavelength of the wave and, R is the measuring distance from the source [2]. The acoustic waves are caused by pressure fluctuations in a compressible mean. In order to develop an equation for

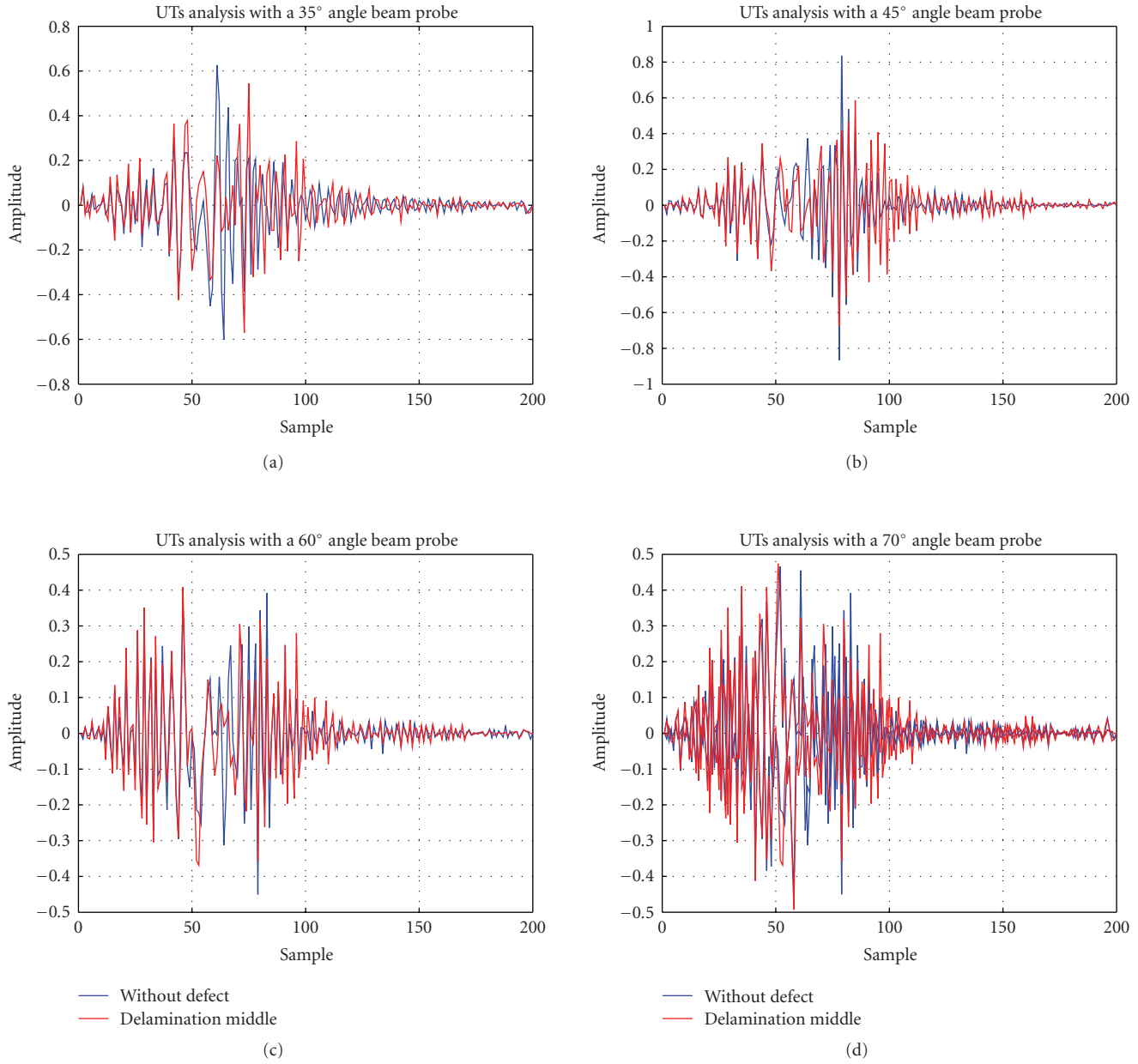

Figure 4: Ultrasound wave propagations results of FEA model.

acoustic wave propagation, it is possible to begin with the ideal case of propagation through a fluid. A nonviscose fluid is a particular fluid in which the effects of friction due to viscosity can be ignored, meaning that the viscous effects are relatively small compared with the inertial restoring forces of the fluid.

It also means that losses due to attenuation through the media can be ignored, making this a lossless equation for acoustic propagation. This equation is often a valid approximation, because, frequently, dissipation is so small that it can be ignored for the frequencies or distances of interest. Using the governing physical equations for sound, the linear wave equation can be derived [3]. These equations are the linear equation of state (2), the linear equation of continuity (3), and the linear equation of force (4), also known as Euler's Equation:

$$p \approx B^* s_c, \tag{2}$$

$$\frac{\partial \rho}{\partial t} + \rho_0 \nabla \vec{u} = 0, \tag{3}$$

$$\rho 0 \frac{\partial \vec{u}}{\partial t} = -\nabla p. \tag{4}$$

Combining (2), (3), and (4), it is possible to consider a single differential equation with one dependant variable

$$\nabla^2 p - \frac{1}{c^2} \frac{\partial^2 p}{\partial t^2} = 0. \tag{5}$$

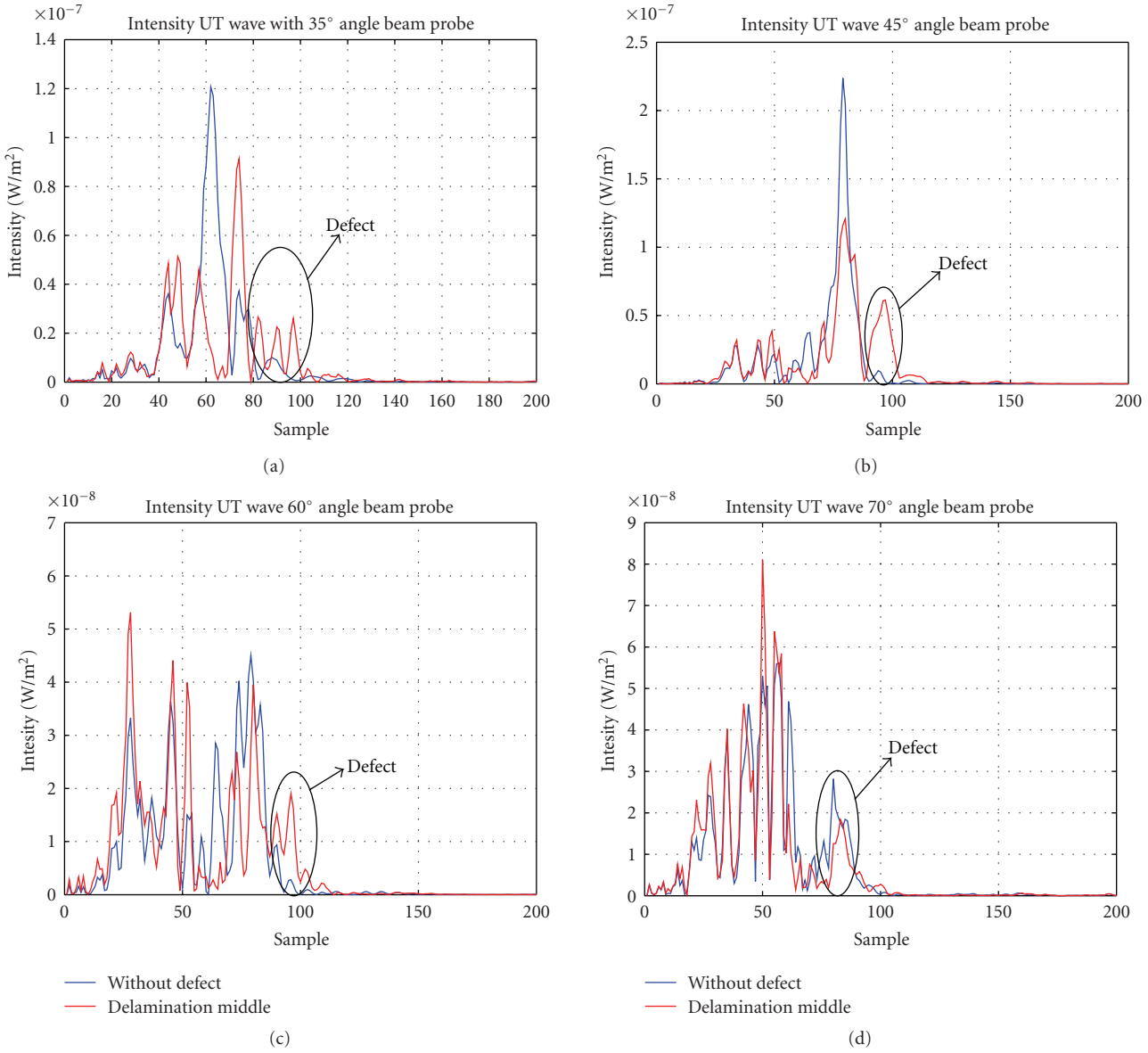

Figure 5: Intensity of the UT wave.

This equation is the linear, lossless wave equation for the propagation of sound in fluids with phase speed c_0. The equation for one-dimensional wave propagation, whose solutions is known, can be written as follows:

$$p(x,t) = P_0 \cos(\omega_0 t - kx). \tag{6}$$

Including the viscosity, the ideal hypothesis is not valid and the Euler's equation must be changed with the inclusion of viscosity effects term to the right side:

$$\rho \frac{\partial \vec{u}}{\partial t} + \nabla p = \left(\frac{3}{4}\eta + \eta_B\right) \nabla(\nabla \cdot \vec{u}) - \frac{1}{2}\rho_0 \nabla^2 \vec{u}, \tag{7}$$

where η is the shear viscosity coefficient and η_B is the coefficient of bulk viscosity. Combining (2), (3), and (7) is possible to obtain a single differential equation with one dependant variable:

$$\nabla^2 p - \frac{1}{c^2}\frac{\partial^2 p}{\partial t^2} + \frac{0.75\eta + \eta_B}{\rho_0 {c_0}^2} \nabla^2 \frac{\partial p}{\partial t} = 0. \tag{8}$$

This equation is the linear, dissipative wave equation for the propagation of sound in fluids.

Note that it is identical to the lossless equation except for the added third term on the left hand side, that is, the viscous dissipative term.

For a plane wave travelling in the positive x direction, the solution of (8) is defined as follows:

$$p(x,t) = P_0 e^{(-\alpha x)} \cos(\omega_0 t - kx), \tag{9}$$

where α is the attenuation coefficient in Np/m which causes the amplitude to decay in an exponential form. Plane waves

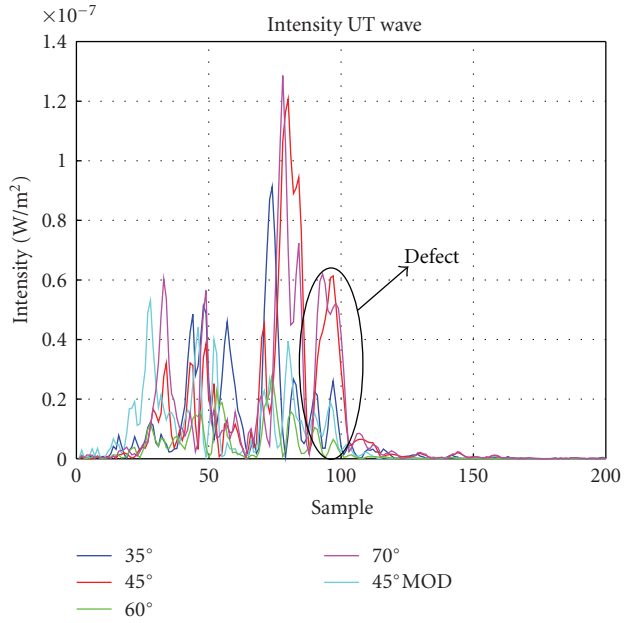

Figure 6: Comparison of UT waves' intensities.

are a special case in the study of acoustic propagation because they propagate in a single direction and they also have constant amplitude and phase on any plane perpendicular to the direction of propagation. Generally, the majority of waves can be considered as planar when sufficiently far from the source point. The solution for the pressure field $p(x,t)$ of a plane wave is described by (6). So, the velocity and velocity potential equations of a plane wave can easily be derived. Due to inherent properties of the plane wave, above described, the velocity of the wave differs from pressure by a constant:

$$\vec{u}(x,t) = \frac{\vec{p}(x,t)}{\rho_0 c_0}, \tag{10}$$

where $\rho_0 c_0$ is defined for a specific acoustic impedance Z_0 of the media. This impedance is analogous to the wave impedance $\sqrt{\mu/\varepsilon}$ of a dielectric medium for electromagnetic waves, or to the characteristic impedance of a transmission line. The velocity potential equation is similarly obtained and it is related to pressure by a complex constant

$$\vec{\Psi}(x,t) = \frac{\vec{p}(x,t)}{j\omega_0\rho_0}. \tag{11}$$

The linear relationship between pressure and velocity is very useful, especially with the development of equations for acoustic intensity.

The instantaneous intensity in W/m^2 of an acoustic wave is

$$I(t) = \vec{p}(x,t) * \vec{u}(x,t). \tag{12}$$

Theoretical approach described in this section has been exploited for the simulation step in order to obtain software measurements. FEA-based approach and data collection will be described in the next section.

Table 1: Geometrical parameters of the model.

Parameter	Dimension
Plate dimension	50 mm × 5 mm
Fibre diameter	0.3 mm
Number of layers	15

4. FEA Approach

In this section we show the proposed model. We propose an Ultrasound FEA model in order to evaluate the presence of delaminations in multi-layer plates of carbon fibre reinforced. They are characterized by different layers, oriented at 0°, 90°, 0° respectively, and reinforced with epoxy resin [4]. The UTs technique is analysed by a numerical model. Finite Element Method- (FEM) based approach can supply an important support for a preliminary in-lab campaign of measurements. The model requires the geometrical and physical definition of the UTs probe and the CFRP/E specimen. The geometry of the system is presented in Figure 2; Table 1 resumes geometrical settings.

The proposed approach, based on UT inspection, exploits the acoustic pressure p [5–7] and has been carried out by a commercial code (Comsol Multiphysics).

In this way we calculated the acoustic pressure p in a general subdomain Ω:

$$\nabla\left(-\left(\frac{1}{\rho_c}\right)(\nabla p - q)\right) + \left(\frac{{k_z}^2}{\rho_c} - \frac{\omega^2}{(\rho_c {c_c}^2)}\right)p = Q, \tag{13}$$

where $\rho_c = k_c Z_c/\omega$ represents the complex fluid density; $c_c = \omega/k_c$ represents the complex speed of sound; $k_c = \omega/c_s - ia$ represents the complex wave number; $Z_c = \rho_0 c_s$ is the complex impedance; ρ_0 is the material density; c_s is the speed of the sound; a is the attenuation coefficient; ω is the angular pulsation; p represents the pressure; Q is the dipole source. For simulating the ultrasound wave, cylindrical wave formulation has been exploited in boundaries setting [8, 9]:

$$\begin{aligned}\mathbf{n}\cdot\frac{1}{\rho_0(\nabla p - q)} &= \left(ik + \frac{1}{2r} - \frac{1}{(8r(1+ikr))}\right)\frac{\left(p_0 e^{-i\mathbf{kr}} - p\right)}{\rho_0} \\ &\quad + \frac{r}{(2\rho_0(1+ikr))}\Delta_T\left(p - p_0 e^{-i\mathbf{kr}}\right) - \frac{i(\mathbf{k}\cdot\mathbf{n})p_0 e^{-j\mathrm{kr}}}{\rho_0},\end{aligned} \tag{14}$$

where p_0 is the source pressure.

All boundaries are modelled with the following conditions: absorbing and reflecting boundary conditions. Reflecting boundary conditions are modelled as Neumann conditions. Absorbing boundary conditions are also modelled as Neumann but with a weak constrain on the time term. In detail, boundaries conditions are set as follows.

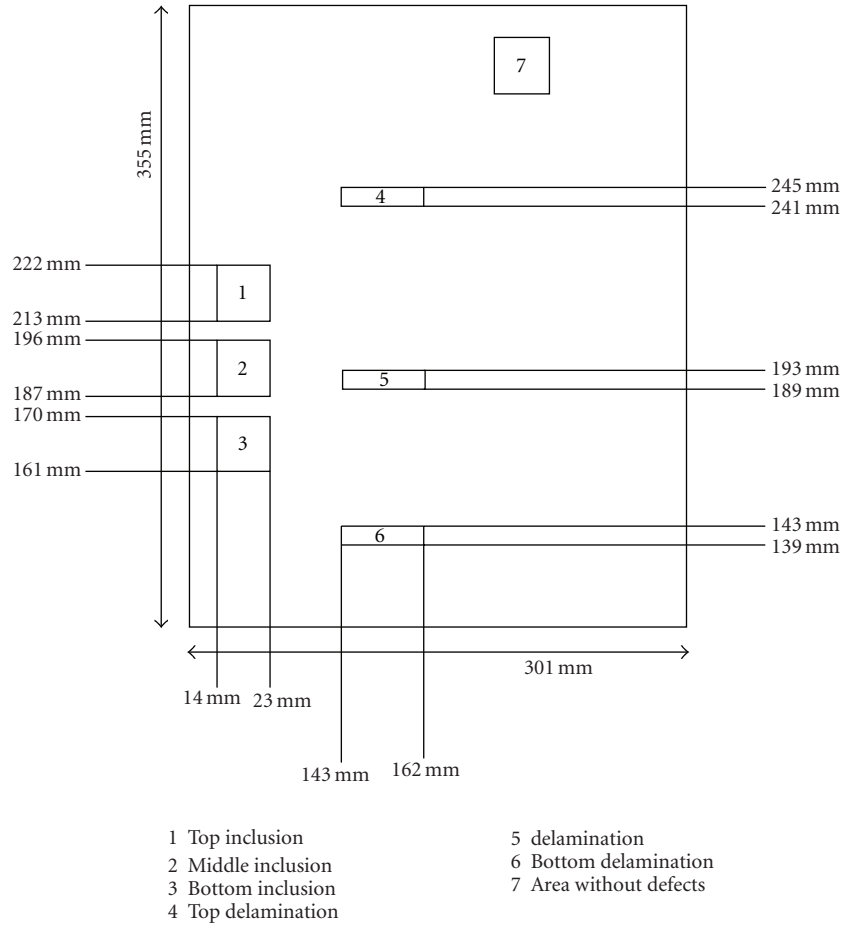

Figure 7: Specimen used for UTs measures.

Continuity Conditions. set to internal boundary of subdomain that represents the UTs wave interaction with the internal structure of examined material:

$$\mathbf{n}\cdot\left(\left(-\left(\frac{1}{\rho_0}\right)(\nabla p - q)\right)_1 - \left(-\left(\frac{1}{\rho_0}\right)(\nabla p - q)\right)_2\right) = 0. \tag{15}$$

Soft-Boundary Conditions. All boundary perimeter they are set up with this condition since the plate has a finite dimension:

$$p = 0. \tag{16}$$

Matched Boundary Conditions. Set to bottom boundary that represents the interaction of the UTs wave with the bottom of examined plate:

$$\mathbf{n}\cdot\left(\frac{1}{\rho_0(\nabla p - q)}\right) = \frac{\left(i(\omega^2/c^2 + k_1k_2)\left(p_0e^{-j\mathbf{kr}} - p\right) + \left(\Delta_T p_0 e^{-j\mathbf{kr}} - \Delta_T p\right)\right)}{(\rho_0(k_1 + k_2)) - i/\rho_0\mathbf{k}\cdot\mathbf{n}p_0e^{-j\mathbf{k}\cdot\mathbf{r}}}. \tag{17}$$

Table 2: Physical subdomain settings.

Parameter	Dimension
Speed Sound/Density [0°] fibres orientation	2000 m/s / 2.1 Kg/m^3
Speed Sound/Density [90°] fibres orientation	1360 m/s / 1.7 Kg/m^3
Speed Sound/Density Epoxy Resin	3000 m/s / 1.2 Kg/m^3
Attenuation Coefficient Carbon Fibre	4.3 e^{-6}
Attenuation Coefficient Epoxy Resin	50

The line source is modelled with a length equal to 0.6 mm. The final results of simulations are shown in Figures 3, 4, 5 and 6.

5. Simulations Results and In-Lab Measures

According our FEM approach, we obtained the useful information, resumed by Table 4, in order to detect the presence of defect during in-lab experimentations.

Table 3: Geometrical parameters of the probe.

Parameter	Dimension			
Height	20 mm			
Length	30 mm			
Source diameter	0.6 mm			
Angle	35°	45°	60°	70°

Table 4: Parameters of built probe.

Parameter	Dimension
Probe height	20 mm
Probe length	30 mm
Source diameter	0.6 mm
Best angle for defects detection	45°

They have been carried out on a specimen of $301 \times 355 \times 4$ mm panel containing delamination-like and no defect area (see Figure 7) in order to validate the results of our FEM approach, with the proposed UTs probe. On the basis of simulations arrangements, the measurements have been carried out with a fixed frequency value (5 MHz). During the scanning along x-axis the maximum of the UTs signal is placed under the probe, and decreasing away from the source [10]. Experimentations confirm the FEA simulations.

6. Conclusions

In this paper, a Finite Element Method (FEM) approach has been proposed. Single-line plane waves emitting sources have been modelled in order to investigate the most effective incidence angle with regard to defects' identification.

According to the FEM approach performances, it is possible to detect the presence of a delamination in the analysed structure. The exploited UT-based experimental methodology has satisfactory confirmed the model increases the ability of detecting very small delaminations in CFRP/Epoxy. This ability has been confirmed from the results obtained by experimental analysis. The UTs signal propagates inside the specimen. The interaction of the wave with the defect causes a reflection of the signal that generated the defect peak. Varying the angle of the probe, there is a different kind of detection of the flaw, as shown in Figure 6. From the numerical results, it is possible to note that the best resolution of defect detection is obtained by a probe inclination equal to 45 degree. Our FEA approach has been subsequently and successfully validated with in-lab measurements.

In conclusion, a future work would be predicting signal affected by noise for the probe used during simulations, that is, reduce the presence of echoes. Authors are actually engaged in this direction.

Nomenclature

$a(x,t)$: Particle acceleration
A: Oscillation amplitude
b: Nonlinear restoring force
c: Speed of wave propagation
c_s : Speed of sound propagation
f_0 : Source frequency
I : Intensity
I_{ref}: Reference intensity
K : Wave number
l : Length of source
m : Mass
p': Perturbation pressure
p_o: Equilibrium pressure
P_o: Initial pressure amplitude
$p(x,t)$: Acoustic pressure
R_m: Mechanical resistance
t: Time
u_o: Initial velocity
$u(x,t)$: Particle velocity

Acknowledgment

Many thanks to the scientists and technicians of Alenia Aeronautica SpA, Pomigliano d'Arco, Naples, Italy, for technical support and data disposal useful to write this paper. Property of collected data belongs to Alenia Aeronatica SpA, Turin, Italy.

References

[1] M. F. Ashby, *Material Selection in Mechanical Design*, Butterworth Heinemann, Oxford, UK, 2nd edition, 1999.
[2] B. A. Auld, *Acoustic Fields and Waves in Solids*, vol. 1, Krieger Publishing, Malabar, Fla, USA, 1990.
[3] A. Chakraborty and S. Gopalakrishnan, "A spectral finite element model for wave propagation analysis in laminated composite plate," *Journal of Vibration and Acoustics*, vol. 128, no. 4, pp. 477–488, 2006.
[4] A. A. Baker and B. C. Hoskin, *Composite Materials for Aircraft Structures*, AIAA Education Series, AIAA, 1986.
[5] D. T. Blackstock, *Fundamentals of Physical Acoustics*, Wiley, New York, NY, USA, 2000.
[6] O. C. Zienkiewicz, *The Finite Element Method*, McGraw-Hill, New York, NY, USA, 1989.
[7] R. B. Thompson and H. N. G. Wadley, "The use of elastic wave-material structure interaction theories in NDE modeling," *Critical Reviews in Solid State and Materials Sciences*, vol. 16, no. 1, pp. 37–89, 1989.
[8] J. M. Whitney, *Structural Analysis of Laminated Anisotropic Plates*, Technomic, Lancaster, Pa, USA, 1987.
[9] F. L. Matthews and R. D. Rawlings, *Composite Materials: Engineering and Science*, Chapman & Hall, Boca Raton, Fla, USA, 1996.
[10] M. Buonsanti, M. Cacciola, S. Calcagno, F. C. Morabito, and M. Versaci, "Ultrasonic pulse-echoes and eddy current testing for detection, recognition and characterisation of flaws detected in metallic plates," in *Proceedings of the 9th European Conference on Non-Destructive Testing*, Berlin, Germany, 2006.

Hindawi Publishing Corporation
Advances in Acoustics and Vibration
Volume 2009, Article ID 927078, 7 pages
doi:10.1155/2009/927078

Research Article

Dynamic Stability of Cylindrical Shells under Moving Loads by Applying Advanced Controlling Techniques—Part II: Using Piezo-Stack Control

Khaled M. Saadeldin Eldalil[1] and Amr M. S. Baz[2]

[1] *Department of Mechanical Engineering, Tanta University, Sperbay, Tanta, Egypt*
[2] *Department of Mechanical Engineering, University of Maryland, College Park, MD 20742, USA*

Correspondence should be addressed to Khaled M. Saadeldin Eldalil, eldalil01@msn.com

Received 2 April 2009; Accepted 6 July 2009

Recommended by Mohammad Tawfik

The load acting on the actively controlled cylindrical shell under a transient pressure pulse propelling a moving mass (gun case) has been experimentally studied. The concept of using piezoelectric stack and stiffener combination is utilized for damping the tube wall radial and circumferential deforming vibrations, in the correct meeting location timing of the moving mass. The experiment was carried out by using the same stiffened shell tube of the experimental 14 mm gun tube facility which is used in part 1. Using single and double stacks is tried at two pressure levels of low-speed modes, which have response frequencies adapted with the used piezoelectric stacks characteristics. The maximum active damping ratio is occurred at high-pressure level. The radial circumferential strains are measured by using high-frequency strain gage system in phase with laser beam detection system similar to which used in part 1. Time resolved strain measurements of the wall response were obtained, and both precursor and transverse hoop strains have been resolved. A complete comparison had been made between the effect of active controlled and stepped structure cases, which indicate a significant attenuation ratio especially at higher operating pressures.

1. Introduction

The production of long slender gun systems to meet increased exit velocity requirements of rounds has subsequently increased the effect of precision and accuracy of firing as well as barrel/round interactions during firing. A lightweight, low-cost method is desired to damp the induced vibrations thereby increasing performance of the gun system.

Some experimental and theoretical methods are suggested for damping and controlling vibrations in the gun tubes. A relatively inexpensive and lightweight method of damping vibrations in some structures is to apply a surface treatment of a viscoelastic material and a constraining layer, as a passive control combination [1], which deals with the transverse vibrations in the system resulted in shear deformation of the viscoelastic material, which in turn dissipates the energy. This technique is very effective for damping terrain and firing-induced vibrations and hence increases precision and accuracy.

The integration of viscoelastic damping materials into various structures has been widely theoretical studied. Euler-Bernoulli beam theory has been used to model viscoelastic materials using the Rayleigh Ritz approximation for damping. Timoshenko beam theory incorporates both shear deformation and rotational deformation in the formulation. The modal strain energy method [2] makes use of the relationship between damping factors and modal loss factors in order to assign damping factors to real elastic modes assign approximation to light damping. The Golla-Hughes-McTavish (GHM) method [3, 4] uses a finite element approach where viscoelastic damping is introduced as a series of minioscillator terms and auxiliary dissipation coordinates. DiTaranto and Blasingame [5] and Mead and Markus [6] derived a sixth-order PDE to model the transverse vibrations of a three-layer beam system based on the equations developed for flexural vibrations of layered plates. In this approach damping of the viscoelastic layer is incorporated through the use of a complex shear modulus.

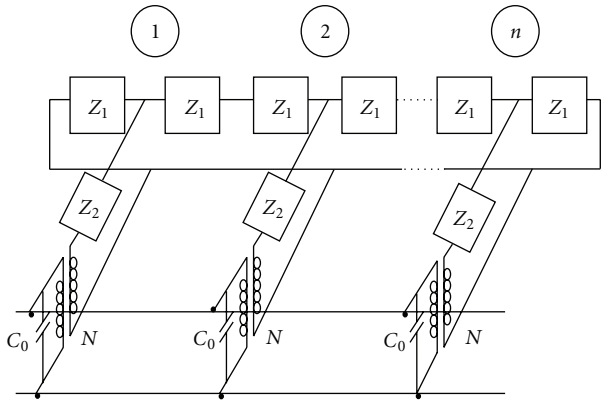

Figure 1: Equivalent circuit representation of a stack with the mechanical ports of each equivalent circuit representing a layer connected in series and n electrical ports in parallel.

Ro et al. [7] and Sung [8] developed this technique theoretically and experimentally by applying active constrained damping layer (ACLD); they modeled the tube/ACLD system by using Golla-Hughes-McTavish method in order to predict the tube response in the time domain. They calculated the transient response using finite element method; the predicted response is compared with that of a tube controlled with passive constrained layer damping treatment. The predictions of the finite element model are validated experimentally. The results obtained indicted that ACLD treatment has achieved significant attenuation of the structure vibrations.

On the other hand, the methods for damping radial and circumferential vibrations of the shell tube walls are completely different. Using periodic stiffeners distributed on the shell tube surface is tried theoretically by Ruzzene and baz [9, 10], Aldareihem and Baz [11, 12], and others [13–15], and studied experimentally in part 1, Eldalil and Baz [16].

In this work, the concept of applying a feedforward control by using piezoelectric stack is experimentally tried. To the best of our knowledge, this technique is not examined before for damping the radial and circumferential deformations of the shell walls theoretically or experimentally. The selection of the piezoelectric stacks is based on its dynamic characteristics which are meeting the shell walls radial and circumferential deformation dynamic modes. A feedforward control system is suggested and designed in order to achieve the optimum attenuation ratio and satisfy suitable dynamic stability.

1.1. Piezoelectric Stack Characteristics. Piezoelectric stacks are used in variety applications that require relatively high force and larger displacement than single element piezoelectric transducers can produce. These include micropositioning systems, solid-state pumps/switches, noise isolation mounts, ultrasonic drills, and stacked ultrasonic transducers. The solution for the zero bond length stacks was derived by Martin [17, 18]. His model was derived from Mason's equivalent circuit of n layers connected mechanically in series and electrically in parallel as shown in Figure 1.

Table 1: The effective material properties for the data of the stack resonator.

Property	Real	Imaginary
s_{33}^E (m^2/N)	2.00×10^{-11}	-3.0×10^{-13}
ε_{33}^T (F/m)	3.00×10^{-11}	-6.17×10^{-10}
d_{33} (C/N)	3.925×10^{-10}	-7.66×10^{-12}
k_{33}	0.5	-0.001

Martin's general solution for the admittance of a piezoelectric stack of area A, n layers, and total length nL is [19]

$$Y(\omega) = i\omega n C_0 + \frac{2N^2}{Z_{ST}} \tanh\left(\frac{n\gamma}{2}\right), \tag{1}$$

where

$$\begin{aligned} C_0 &= \frac{\varepsilon_{33}^T A}{L}(1 - k^2{}_{33}), \\ N &= \frac{A d_{33}}{L s_{33}^E}, \\ Z_{ST} &= \left[Z_1 Z_2 \left(2 + \frac{Z_1}{Z_2}\right)\right]^{0.5}, \\ \gamma &= 2 \operatorname{arcsin} h\left[\left(\frac{Z_1}{2Z_2}\right)^{0.5}\right], \\ Z_1 &= i\rho v^D A \tan\left(\frac{\omega L}{2v^D}\right), \\ Z_2 &= \frac{\rho v^D A}{i \sin(\omega L / v^D)} + \frac{iN^2}{\omega C_0}, \end{aligned} \tag{2}$$

and $v^D = 1/\sqrt{\rho s_{33}{}^D}$ is the acoustic velocity at constant electric displacement. The constants ε_{33}^T, s_{33}^D, d_{33} are the free permittivity, the elastic compliance at constant electric displacement, and the piezoelectric charge coefficient, respectively. Using (1) to (2), Martin demonstrated that in the limit of large n ($n > 8$), the acoustic wave speed in the material was determined by the constant field elastic constant $s_{33}^E(1/\sqrt{\rho s_{33}^E})$. In the limit of $n > 8$ an analytical equation for the admittance was presented which allowed for direct determination of material constants from the admittance data [3]. In this limit the admittance was shown to be

$$Y = \frac{iAn\omega_{33}^T}{} \left[1 - (k_{33})^2 + \frac{(k_{33})}{\omega/4f_s} \tan\left(\frac{\omega}{4f_s}\right)\right], \tag{3}$$

where the series resonance frequency is

$$f_s = \frac{1}{2\pi L}\sqrt{\frac{1}{\rho s_{33}^E}}. \tag{4}$$

The effective material properties are shown in Table 1, for the data of the stack resonator shown in Figure 2. The stack length $nL = 0.02$ m, Area $A = (0.01)^2$ m^2, and density $\rho = 7800$ kg/m^3.

For more details, refer to [19].

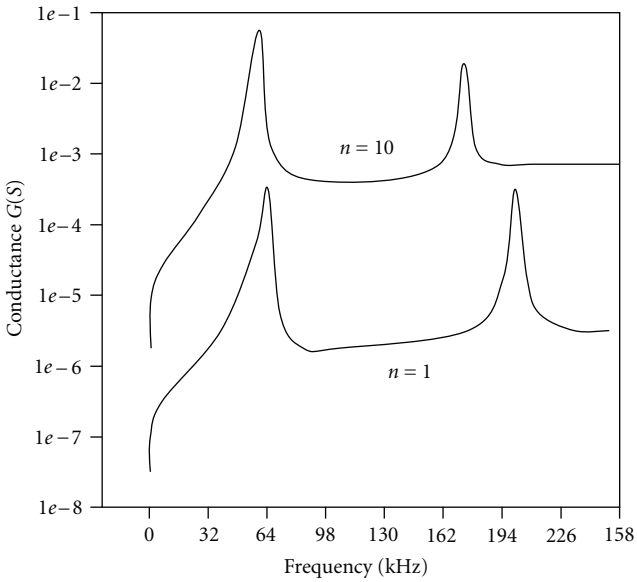

Figure 2: Typical conductance as a function of frequency for $n = 1$ to 10 layers.

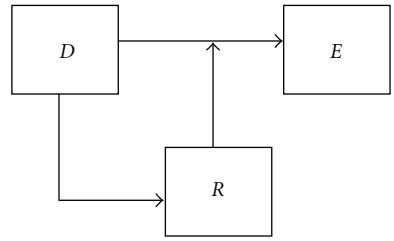

Figure 3: Basic mechanisms of regulation, from left to right: buffering, feedforward, and feedback block diagrams.

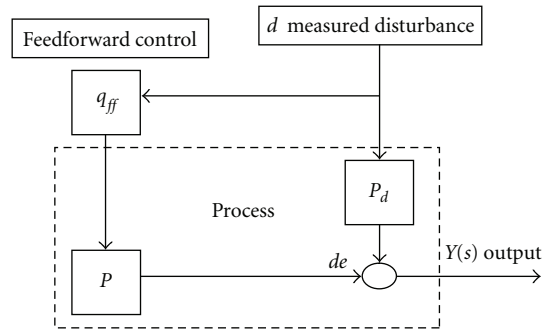

Figure 4: Traditional feedforward control structure.

2. Feedforward Control

2.1. Concept of Feedforward Control. Feed-forward control, which is used herein, will suppress the disturbance deformations before it has had the chance to affect the system's essential variables. This requires the capacity to anticipate the effect of perturbations on the system's goal. Otherwise the system would not know which external fluctuations to consider as perturbations, or how to effectively compensate their influence before it affects the system. This requires that the control system is able to gather early information about these fluctuations. Figure 3 shows block diagram of typical feedforward control system; the effect of disturbances D on the essential variables E is reduced by an active regulator R.

Feedforward control can entirely eliminate the effect of the measured disturbance on the process output. Even when there are modeling errors, feed-forward control can often reduce the effect of the measured disturbance on the output better than that achievable by feedback control alone. However, the decision as to whether or not to use feedforward control depends on whether the degree of improvement in the response to the measured disturbance justifies the added costs of implementation and maintenance. The economic benefits of feedforward control can come from lower operating costs and/or increased salability of the product due to its more consistent quality.

2.2. Mathematical Formulation. Figure 4 shows a traditional feedforward control scheme. The transfer function between the process output Y and the measured disturbance d as shown in Figure 4 is

$$Y(s) = \left(P_d - Pq_{ff}\right)d. \tag{5}$$

To eliminate the effect of the measured disturbance, we need only choose q_{ff} so that:

$$\begin{aligned} P_d - Pq_{ff} &= 0, \\ q_{ff} &= P^{\sim -1}P_{\mathrm{d}}^{\sim}, \end{aligned} \tag{6}$$

where a $\sim$ over a process transfer function indicates that it is a model of the process. Even in the above case, where the feedforward controller can perfectly compensate the measured disturbance, Seborg et al. [20].

3. Experimental Setup

The experiments were carried out with in-door Pneumatic 6/12-feet helium Gun Facility in the Vibration and Noise Control Laboratory at University of Maryland; it has a stainless steel tube length of 6 feet. The detailed description is found in part 1, Eldalil and Baz [16].

3.1. Piezoelectric Stack Configuration. The piezoelectric stack and shell tube combination is shown in Figure 5. As indicated in part 1 [16], the stiffeners are composed of three parts, two half rings (2, 3), in Figure 5, and one outer ring, surrounding the shell tube (1); consequently, in active control, the outer ring is removed and the stacks (4, 7) are rested on the upper and lower half rings. A stainless steel clamp strip (6) is used to hold the components fixed in position, and the screw (5) is used to create initial tension in the clamp strip and consequently generates compression force distributed around the shell tube substituting the removed outer ring of the stiffener.

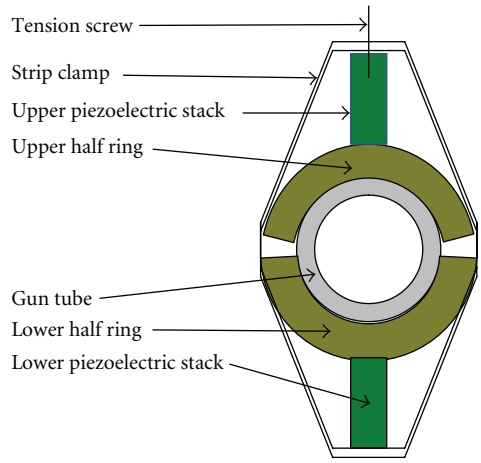

Figure 5: Double Piezoelectric stack configuration.

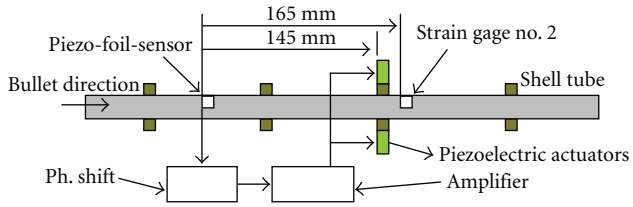

Figure 6: Piezoelectric stacks/feedforward control scheme.

3.2. Feedforward Control Elements Representation. The control circuit scheme is shown in Figure 6, of type feedforward; it is composed of piezoelectric foil pressure sensor located at distance $\times 1$ (165 mm) upstream of the strain gage of location number 2, and at distance $\times 2$ (145 mm) upstream the piezoelectric stack actuator. The output signals are phase shifted and amplified, then feed the piezoelectric stacks, which are located at distance $\times 3$ (20 mm) upstream the strain gage of location number 2. The sensor has a time advance of $\Delta t1$ (0.391 milliseconds) and the system (phase shifter, amplifier, and piezoelectric stacks) has a time lag of $\Delta t2$ (0.372 milliseconds), so for ideal operating case the two times should be equal, or $\Delta t2 < \Delta t1$ by few percent. By this way the actuators will have sensible impact on the tube vibrations; the phase can be adjusted by using phase shifter. The piezoelectric stack control setup view picture is shown in Figure 7.

3.3. Experimental Measurements and Results. The measurements are carried out at two operating helium pressures, 1600 and 2000 psi, and the controller (piezo-stack) is installed very close to location number 2 on the gun tube, as indicated in part 1 [16]. The expected deforming vibration due to these pressures ranges between 7.2 and 25 kHz, Part 1 [16], that is, far enough from the first mode frequency of the piezoelectric stack (64 kHz), as shown in Figure 2.

3.3.1. Measurements at Pressure Level of 1600 psi. The time resolved measurement of plain tube is shown in Figure 8(a), and that of the arrangement when the control is turned off, which is equivalent to the stiffened tube; is shown in Figure 8(b), and the active controlled time domain signals is shown in Figure 8(c). A time domain comparison of active and stiffened tube, is shown in Figure 9, and the comparison analysis of the frequency domains is shown in Figure 10.

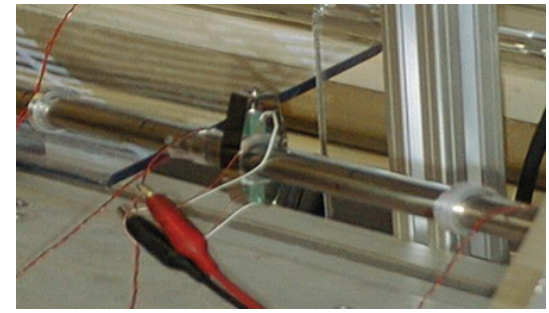

Figure 7: Piezoelectric stack control view picture.

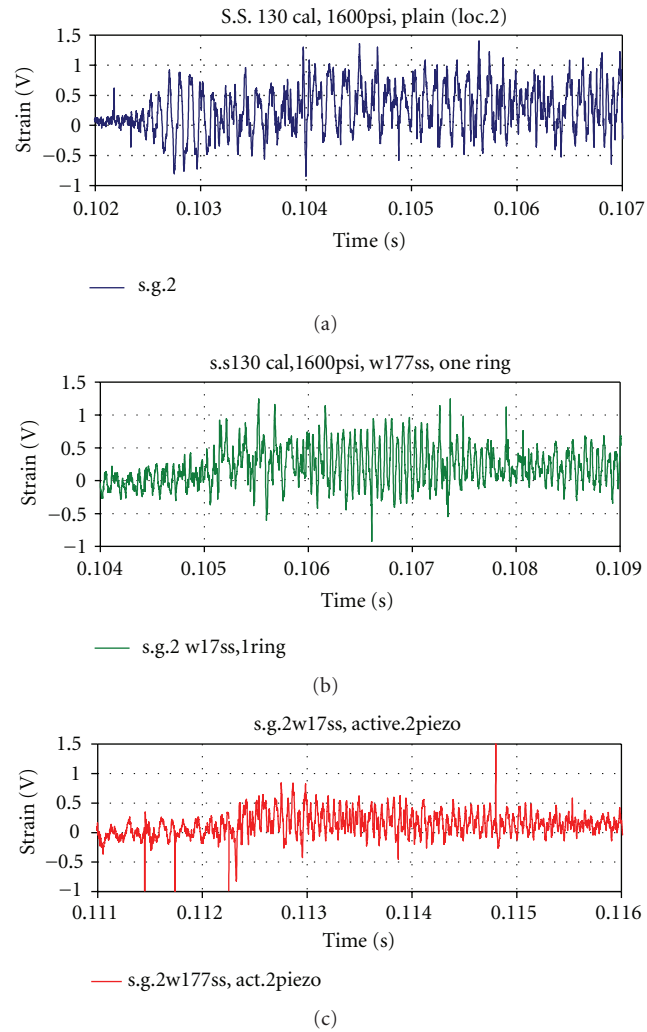

Figure 8: (a) Output signal at location number 2 of plain tube at 1600 psi. (b) Output signal at location number 2 of tube with 17 single stiffeners. (c) Output signal of location number 2 with 17 single stiffeners and with active control at 1600 psi.

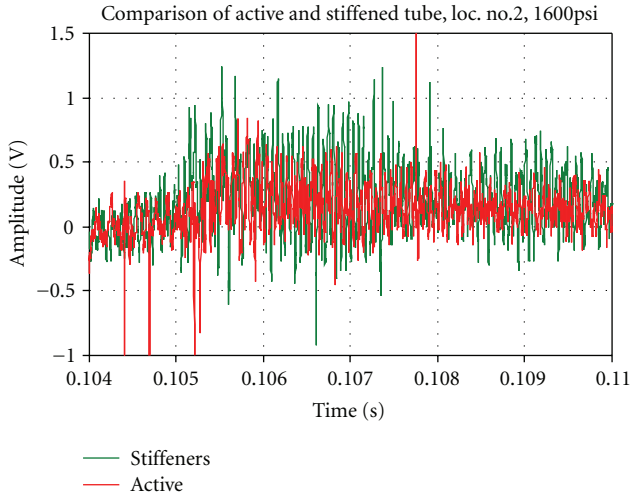

FIGURE 9: Time domain comparison between active and stiffened tube at location no. 2 at operating pressure 1600 psi.

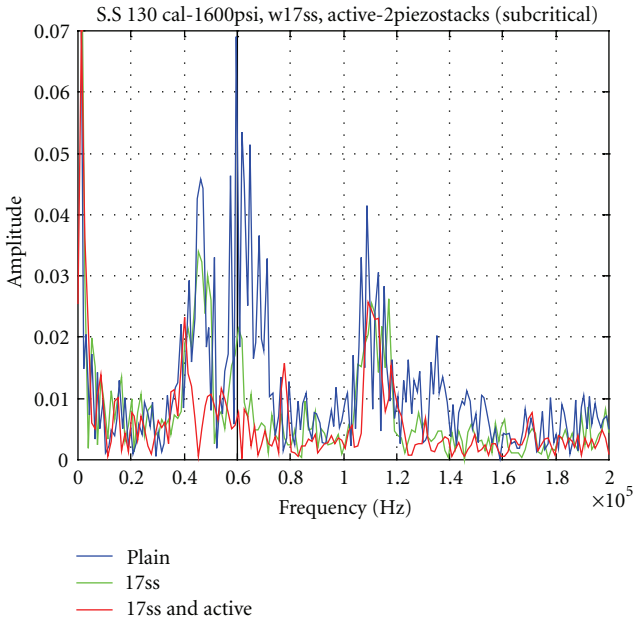

FIGURE 10: Frequency domain comparison between plain, stiffened tube, and with active piezo-stack control.

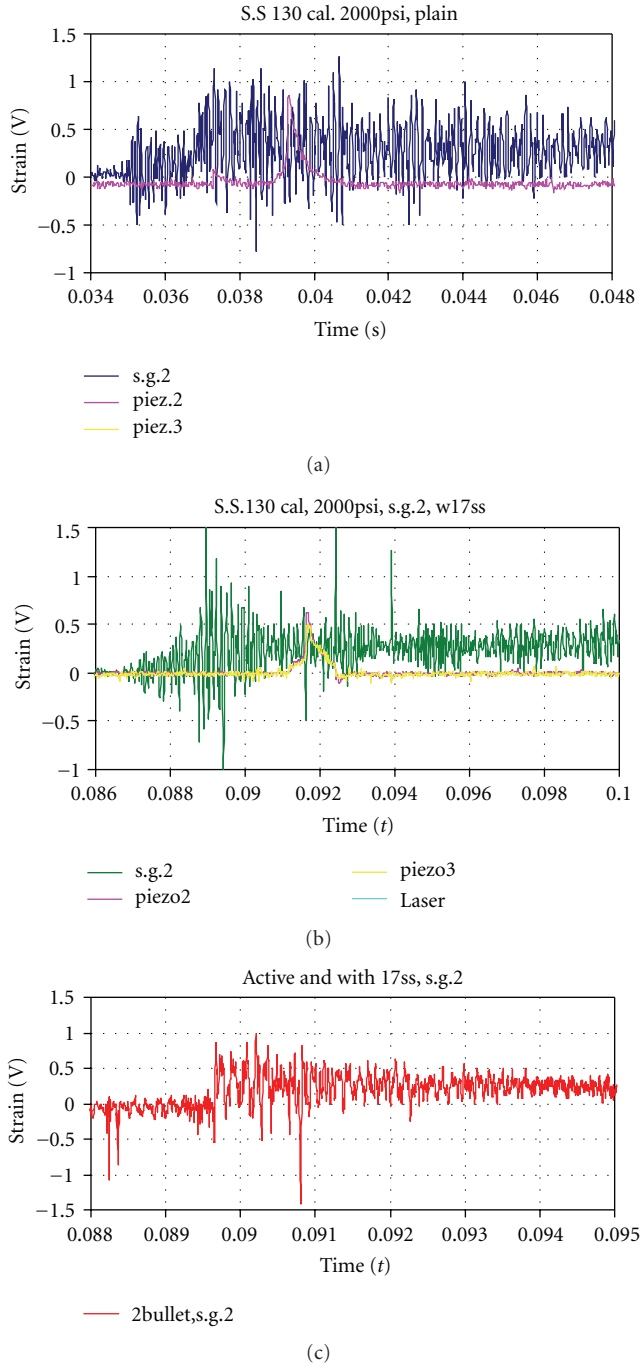

FIGURE 11: (a) Output signal at location number 2 of plain tube at 2000 psi. (b) Output signal at location number 2 of tube with 17 single stiffeners at 2000 psi. (c) Output signal of location number 2 with 17 single stiffeners and with active control at 2000 psi.

The attenuation ratio due to using active piezoelectric stack is attained to 33%, at vibration mode of 7.2 kHz and 48% at vibration mode of 9.5 kHz for pressure level of 1600 psi. The effect of active control is decreased at higher vibration modes.

3.3.2. Measurements at Pressure Level of 2000 psi. The time domain measurement of the plain tube at pressure level of 2000 psi is shown in Figure 11(a) and that of the stiffened tube with piezo-stack arrangement without control is shown in Figure 11(b), and the controlled time resolved signal is shown in Figure 11(c). The frequency domain comparison is shown in Figure 12. A comparison of the piezoelectric foil sensor and amplifier output signals (piezo-stqack loading signal or the control effort) is shown in Figure 13, at amplifier gain factor of 2.

The radial strain vibration is attenuated by using the active piezoelectric control by a ratio of 46% at vibration mode of 7.2 kHz and 65% at 9.5 kHz. The attenuation ratio is increased at higher pressure level of 2000 psi than at pressure

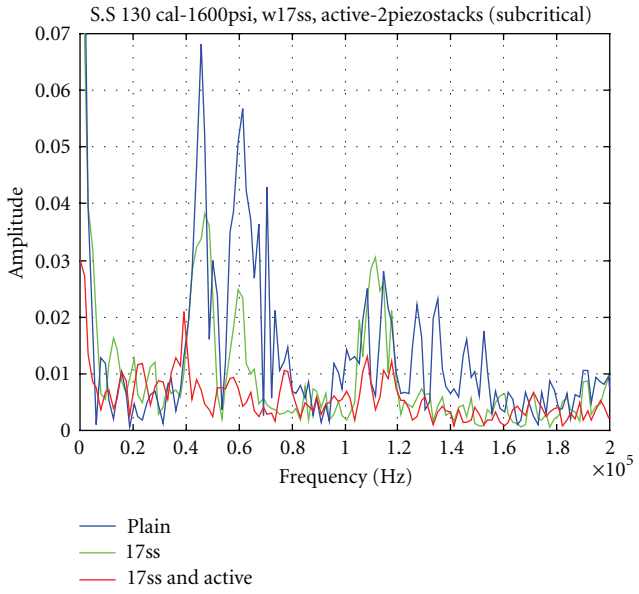

Figure 12: Frequency domain comparison between plain, stiffened tube, and with active control at 2000 psi.

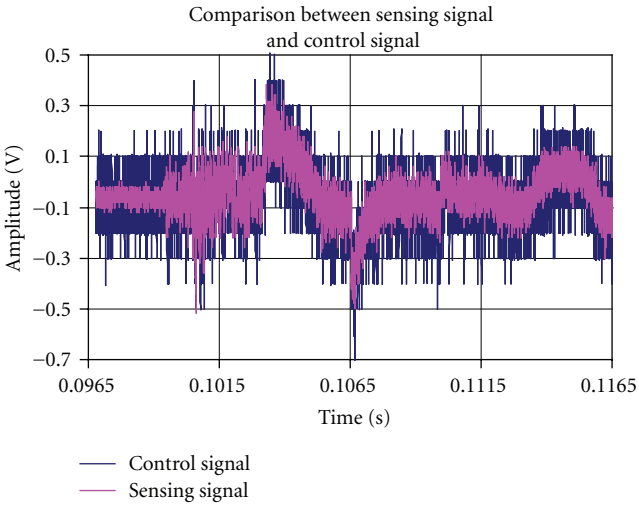

Figure 13: Comparison between piezoelectric sensor and amplified signals at amplifier gain factor of 2.

level of 1600 psi, by a value of 40% for the first mode and by 35% for the second mode of vibrations. The frequency is shifted to lower values by about 13%. This due to increasing the control effort nonlinearly with strain deformations which are occurred at the two pressure levels of the first and second experiments; consequently, the control signal is magnified sharply.

4. Conclusion

A cylindrical shell is actively controlled by using piezoelectric stacks for attenuating the radial circumferential vibrations due to moving pressure propelling mass.

A feedforward control scheme is designed and constructed by using piezoelectric foil sensor to predict in advance the incoming dynamics vibration and piez-stacks actuators.

The control system is checked at two pressures levels; first pressure level is 1600 psi and the second pressure level is 2000 psi. The attenuation ratio is predicted at two modes of low-frequency vibrations.

At first mode of vibration, 7.2 kHz, the attenuation ratio is found to be about 33% and 46% at pressure levels of 1600 psi and 2000 psi, respectively.

And at second mode of vibration, 9.5 kHz, the attenuation ratio is found to be about 48% and 65% at pressure levels of 1600 psi and 2000 psi, respectively. At higher modes of vibrations the attenuation effect decreases to lower ratios. The frequency is shifted to lower values by about 13%.

The frequency domain comparison for the two pressure levels indicates that the stability is satisfied and no spill over occurred.

References

[1] M. Z. Kiehl and C. P. T. W. Jerzak, "Modeling of passive constrained layer damping as applied to a gun tube," *Shock and Vibration*, vol. 8, no. 3-4, pp. 123–129, 2001.

[2] C. D. Johnson and D. A. Kienholz, "Finite element prediction of damping in structures with constrained viscoelastic layers," *AAIA Journal*, vol. 20, no. 9, pp. 1284–1290, 1982.

[3] D. J. McTavish and P. C. Hughes, "Modeling of linear viscoelastic space structures," *Journal of Vibration and Acoustics*, vol. 105, pp. 103–110, 1993.

[4] D. H. Golla and P. C. Hughes, "Dynamics of viscoelastic structures—a time-domain finite element formulation," *Journal of Applied Mechanics*, vol. 52, pp. 897–906, 1985.

[5] R. A. DiTaranto and W. Blasingame, "Composite damping of vibrating sandwich beams," *Journal of Engineering for Industry*, 1967.

[6] D. J. Mead and S. Markus, "The forced vibration of a threelayer, damped sandwich beam with arbitrary boundary conditions," *Journal of Sound and Vibrations*, vol. 10, no. 2, pp. 163–175, 1969.

[7] J. Ro, K. S. El-Din, and A. Baz, "Vibration control of tubes with internally moving loads using active constrained layer damping," in *Proceedings of ASME Annual Meeting*, vol. 223, pp. 1–11, Dallas, Tex, USA, November 1997.

[8] Y.-G. Sung, "Modeling and control with piezoactuators for a simply supported beam under a moving mass," *Journal of Sound and vibration*, vol. 250, no. 4, pp. 617–626, 2002.

[9] M. Ruzzene and A. Baz, "Dynamic stability of periodic shells with moving loads," *Journal of Sound and Vibration*, vol. 296, no. 4-5, pp. 830–844, 2006.

[10] M. Ruzzene and A. Baz, "Response of periodically stiffened shells to a moving projectile propelled by an internal pressure wave," *Mechanics of Advanced Materials and Structures*, vol. 13, no. 3, pp. 267–284, 2006.

[11] O. J. Aldraihem and A. Baz, "Moving-loads-induced instability in stepped tubes," *Journal of Vibration and Control*, vol. 10, no. 1, pp. 3–23, 2004.

[12] O. J. Aldareirhem and A. Baz, "Dynamic stability of periodic stepped beams under moving loads," *Journal of Sound and Vibration*, vol. 250, no. 2, pp. 835–848, 2002.

[13] R. N. Miles and P. G. Reinhall, "An analytical model for the vibration of laminated beams including the effects of both shear and thickness deformation in the adhesive layer," *Journal of Vibration, Acoustics, Stress, and Reliability in Design*, vol. 108, pp. 56–64, 1986.

[14] E. L. Kathe, "MATLAB modeling of non-uniform beams using the finite element method for dynamic design and analysis," Tech. Rep. ARCCB-TR-960 10, US Amy Armaments Research, Development and Engineering Center; Close Combat Armaments Center, Benèt Laboratories, Watervliet, NY, USA.

[15] M. J. Lam, W. R. Saunders, and D. J. Inman, "Modeling active constrained layer damping using Golla-Haughes-McTavish approach," in *Smart Structures and Materials 1995: Passive Damping*, vol. 2445 of *Proceedings of SPIE*, pp. 86–97, San Diego, Calif, USA, March 1995.

[16] K. M. S. Eldalil and A. M. S. Baz, "Dynamic stability of cylindrical shells under moving loads by applying advanced controlling techniques Part 1-Using Periodic Stiffeners," in *Advanced Materials for Application in Acoustics and Vibration*, Cairo, Egypt, January 2009.

[17] G. E. Martin, "Vibrations of coaxially segmented longitudinally polarized ferroelectric tubes," *The Journal of the Acoustical Society of America*, vol. 36, no. 8, pp. 1496–1506, 1964.

[18] G. E. Martin, "On the theory of segmented electromechanical systems," *The Journal of the Acoustical Society of America*, vol. 36, no. 7, pp. 1366–1370.

[19] S. Sherrit, S. P. Leary, Y. Bar-Cohen, B. P. Dolgin, and R. Tasker, "Analysis of the impedance resonance of piezoelectric stacks," in *Proceedings of the IEEE Ultrasonics Symposium*, vol. 2, pp. 1037–1040, San Juan, Puerto Rico, October 2002.

[20] D. E. Seborg, T. F. Edgar, and D. A. Mellichamp, *Process Dynamics and Control*, John Wiley & Sons, New York, NY, USA, 1989.

Hindawi Publishing Corporation
Advances in Acoustics and Vibration
Volume 2009, Article ID 956263, 7 pages
doi:10.1155/2009/956263

Research Article

Mitigation of Railway Traffic Induced Vibrations: The Influence of Barriers in Elastic Half-Space

Michele Buonsanti,[1] Francis Cirianni,[2] Giovanni Leonardi,[2] Adolfo Santini,[1] and Francesco Scopelliti[2]

[1] *Department of Mechanics and Materials (MECMAT), Mediterranean University of Reggio Calabria, Via Graziella, Feo di Vito, 89100 Reggio Calabria, Italy*
[2] *Department of Information Science, Mathematics, Electronics, and Transportations (DIMET), Mediterranean University of Reggio Calabria, Via Graziella, Feo di Vito, 89100 Reggio Calabria, Italy*

Correspondence should be addressed to Giovanni Leonardi, giovanni.leonardi@unirc.it

Received 23 January 2009; Revised 6 May 2009; Accepted 9 May 2009

Recommended by Yehia Bahei-El-Din

In this paper, the problem of vibrations induced by trains and their propagation through the soil is studied. Particular attention is focused on the vibration induced by trains in motion and on the effects of such vibrations on the foundations of buildings in proximity of the tracks. The interaction between propagating waves induced by trains in motion and buildings foundations is a problem which does not admit a straightforward analytical solution; thus a solution is given by the use of a model based on the finite elements method. Firstly, we analyze the theoretical aspects of the problem by considering constant or harmonic loads moving along a straight railway track; then, we define a transfer function soil-railway and the response function of the entire system. The study aims to address the wave propagation in an elastic semi-space and the presence in the ground of a discontinuity element, such as a barrier of a given depth is considered. The efficiency variation of barriers is analyzed in function of the different materials used, and different numerical simulations are analyzed in order to study how the wave propagation and the track-soil interaction are influenced by the membrane, seen as damping barrier.

1. Introduction

The foundations of structures are subject to vibrations due to moving masses, as vehicles in transit, vibrations which can cause damage locally to the foundations, as they can also travel up to the structures in elevation (Figure 1).

In this paper we consider the effects of vibrations due to the transit of locomotives on a railway, analyzing how the presence of material discontinuity, in an elastic semispace has an influence on the transmission of waves generated by a train passing by. The presence of barriers, made in polymeric material, rubber, or in concrete, seems to cause reflection and refraction of the vibrations generated in the ground. There are some references in scientific literature. Francois et al. [1], approached interaction between ground and infrastructures, in presence of vibrations generated by road traffic, while Sheng et al. [2], modelled the propagation of vibrations due to constant or harmonic loads, produced by the movement of trains.

Numerical aspects are developed in detail in Lombaert et al. [3] and Fiala et al. [4], while in Hubert et al. [5], a detailed analysis using the Boundary Element Method, in the dominion of frequency and of time, is developed on a model of elastic semispace. In the work of Andersen and Nielsen [6], a model for the reduction of vibrations of the ground through the use of barriers dipped in the ground and laid between rail track and structure is proposed. In the paper, after some general concepts of theory of the vibrations, the aim is set on the problem in homogenous elastic and isotropic semispace, where a two-dimensional constitutional discontinuity is localized, representing the artificial barrier in the hypothesis set for different materials (rubber, polyurethane, and concrete).

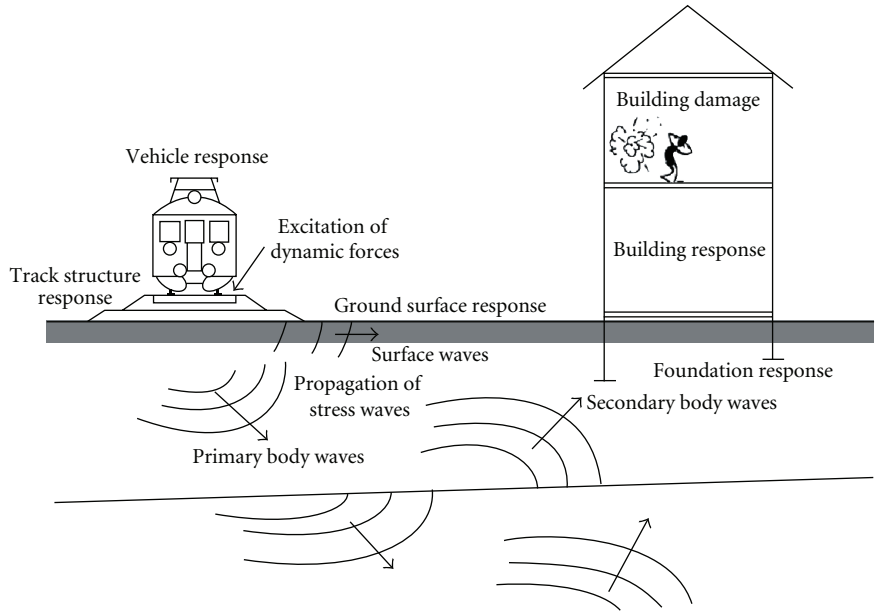

Figure 1: Transmission of induced vibrations.

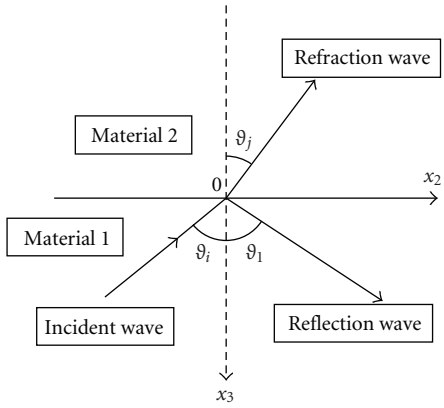

Figure 2: Incident wave and reflection.

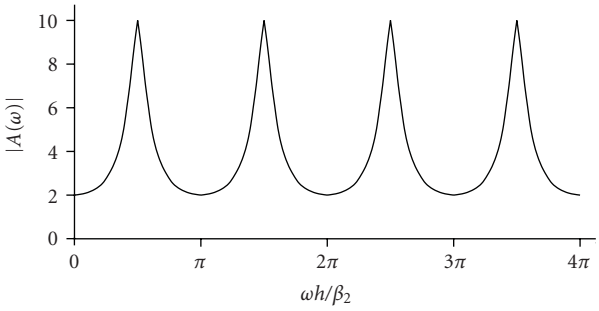

Figure 3: Amplification waves for $Z_1/Z_2 = 4$.

Once the case is defined in its theoretical formulation, a numerical simulation with the support of computer application is carried out. What we want to analyze is the variation of the mechanism of propagation of the vibration waves which happens in the semispace, regarding the conditions of quiet, and anyway without the influence of a traveling load. In particular, we observe as the nature of the material used for the realization of the barrier vary, how the conditions of propagation of the waves vary, and their influence, in an equilibrium state, on the contour conditions of an eventual foundation laid under the barrier.

2. Vibrations Theory

In regard to the fundamental aspects in the theory of the vibrations, in all this paper we follow the lines expressed in Hartog [7] and Clough and Penzien [8]. Our problem can have a first general organization in the context of the response for harmonic type loads. It is possible to characterize the following fundamental equations in the case of systems without damping:

$$m\ddot{u}(t) + ku(t) = p_0 \sin \omega t, \tag{1}$$

and with damping,

$$m\ddot{u}(t) + cu(t) + ku(t) = p_0 \sin \omega t. \tag{2}$$

The solution of (1) is admitted, from the combination of a complementary solution with a particular solution, in the shape

$$u(t) = A \sin \omega t + B \cos \omega t + \left(\frac{p_0 \beta}{\kappa}\right)(1 - \beta 2) \sin \omega t. \tag{3}$$

In the case of (2) the general solution is of the type

$$u(t) = e^{-\xi \omega t}(A \sin \omega_D t + B \cos \omega_D t) + \frac{p_0}{k} \times \frac{1}{(1-\beta^2)^2 + (2\xi\beta)^2}\left[(1-\beta^2) \sin \omega t - 2\xi\beta \cos \omega t\right]. \tag{4}$$

Figure 4: Modelling of the railway embankment.

The first term of (4) represents the transitory result, while the second term represents the stationary result, which has the pulsation of the solicitation but is out of sync with the last wave. The factor of dynamics amplification D is defined as the relationship betw.een the amplitude of the stationary response and the static movement produced from the external load. In a generalized manner D is function of the damping ratio and of the frequency relationship and usually it tends to infinite when damping is absent.

3. Theoretical Aspects in the Model Characterization

In an elastic semispace we consider that the source of disturbance (train) generates a set of waves which are distributed in the plane system and therefore we can classify the waves plane and classify our problem as a motion of waves within a semi-infinite body, which is assumed, for simplicity, elastic, homogenous, and isotropic. This type of phenomenon is shown in its generality and specificity in the case of the seismic waves as treated in Boschi and Dragoni [9]. We then consider a longitudinal elastic plane wave that propagates in x-direction, if we assume the movement $\mathbf{u}$ associated to it as a periodic function of the time, $\mathbf{u}$ can be placed in the form

$$\mathbf{u}(x,t) = \mathbf{x}\, a\cos(kx - \omega t + \varphi), \tag{5}$$

where a is the amplitude, k the wave number, φ a constant.

Using the relation between the exponential and trigonometrical functions, and the complex notation, each component of the movement, for a monochromatic wave, can be defined as

$$u(x,t) = Ae^{i(kx-\omega t)}, \tag{6}$$

that represents an oscillation of amplitude A and wavelength $\lambda = 2\pi/\kappa$, which propagates in the direction of the wave

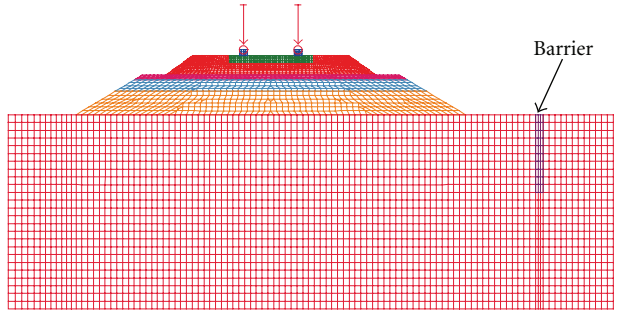

Figure 5: Finite element mesh of the two-dimensional model.

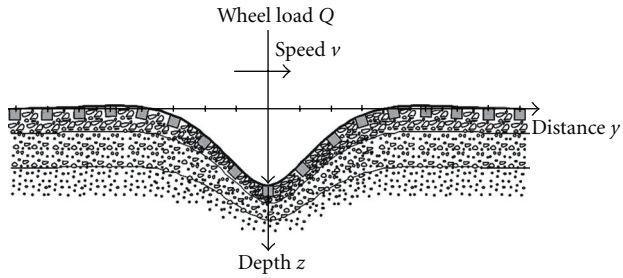

Figure 6: Deflection of the track structure from one wheel.

vector k at constant speed (phase speed):

$$v_f = \frac{\omega}{\kappa}, \tag{7}$$

any system of waves can be considered as a superimposition of monochromatic plane waves that move with the group velocity:

$$v_g = \frac{d\omega}{d\kappa}. \tag{8}$$

Equation (8) represents the speed with which the energy is transported and, if v_f is different from v_g, the constant phase surfaces move from an extremity to another in the package of waves while this last one is the same one in motion.

Given such assumption, we consider the elastic semispace as composed of different homogenous elements. Let's assume to form a put in elastic discontinuity, in the cross-sectional sense to the semispace, so to be placed in cross-sectional sense to the wave movement. This eliminates the direct flow of the waves from the source to the site of the structure placing itself as element of filter to the vibrations generated from the movement of the train. Regarding the interaction with the wave, or the set of waves, the discontinuity assumes the role of reflection element and refraction for two-dimensional waves. If we consider two elastic semispaces joined with an element of material discontinuity, we may say that ρ, α, β are, respectively, the density and the speed of the j elastic waves in the first semispace while ρ^*, α^*, β^* are the same amounts in the second semispace (Figure 2).

Refraction and reflection of the elastic waves will happen on the discontinuity surface, longitudinal ones, and of cross-sectional ones which can transform one in the other when

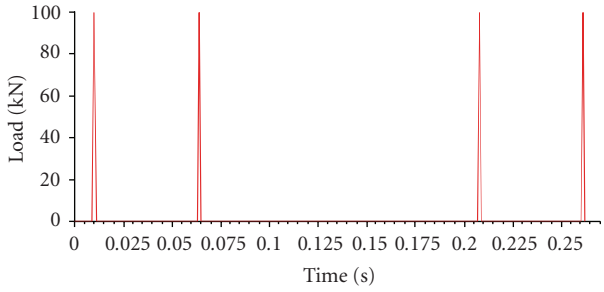

Figure 7: Load distribution of a moving wheel travelling at speed of 200 km/h.

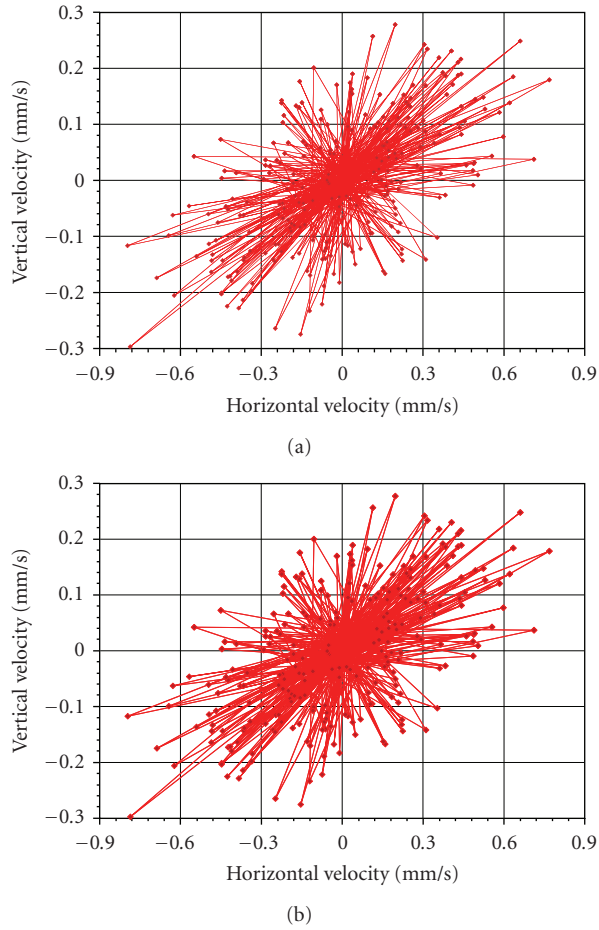

Figure 8: Nodes velocity (m/s) responses for a train speed of 200 km/h.

inciting on the surface that separates the two semispaces. In accordance with Graff [10], the coefficient of reflection or refraction c_{ij} assumes the form:

$$c_{ij} = \frac{2\rho_i\beta_i \cos\theta_i}{\rho_i\beta_i \cos\theta_i + \rho_j^*\beta_j^* \cos\theta_j}. \tag{9}$$

The contour conditions, on plan $x_3 = 0$ are the continuity of stress and the movement.

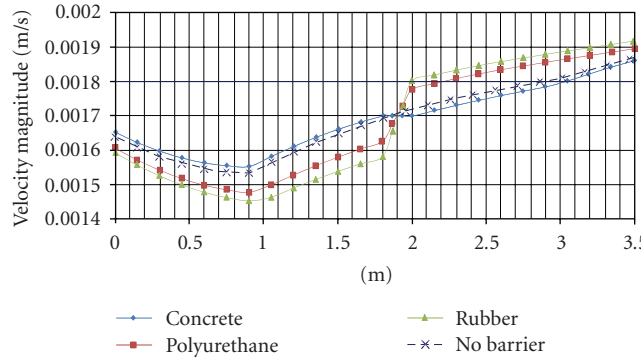

Figure 9: Trend of the velocity with the increase of the distance from embankment at the depth of 1 m.

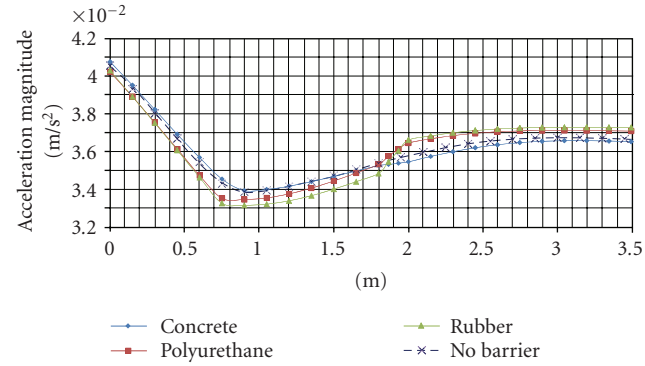

Figure 10: Trend of the acceleration with the increase of the distance from embankment at the depth of 1 m.

We assume that given a monochromatic wave incident with frequency ω, number of wave k_1 and travelling unitary amplitude in the semispace in direction-x_3, it produces one cross-sectional movement, in direction x_2 expressed in the form:

$$\mathbf{u}(x_3, t) = \exp[\omega t + k_1(x_3 - h)], \quad x_3 \geq h, \tag{10}$$

after the phenomenon of refraction and reflection the field of movements takes the form:

$$\begin{aligned}\mathbf{u}(x_3, t) = {} & \exp[\omega t + k_1(x_3 - h)] \\ & + R^* \exp[\omega t - k_2(x_3 - h)], \quad x_3 \geq h,\end{aligned} \tag{11}$$

where R^* is a coefficient that holds account of all the waves that travel in positive direction x_3. The contour conditions require that traction on free surface x_3 is equal to zero, $x_3 = 0$, and that the movement and the traction are continuous on the surface of discontinuity $x_3 = h$. In agreement with Graff [10], given $Z_1, Z_{\text{the }2}$ as stiffness of the two semispace and $A(\omega)$ the coefficient of the exponential, the module of the latter supplies the amplification of the waves:

$$|A(\omega)| = \frac{2}{\operatorname{sqr}\left[\cos^2\left(\omega h/\beta_j\right) + (Z_2/Z_1)^2 \sin^2\left(\omega h/\beta_j\right)\right]}. \tag{12}$$

Table 1: Properties of structural materials.

Mechanical characteristics	Rail (UIC60)	Sleeper (concrete)	Traditional ballast	HMA subballast	Protective layer	Embankment
Density ρ (kg/m^3)	7850	2400	1250	2200	2000	1000
Modulus E (MPa)	210000	30000	130	6000	160	80
Poisson's Ratio ν	0.30	0.15	0.30	0.40	0.45	0.50

Table 2: Properties of barriers.

Mechanical characteristics	Density ρ (kg/m^3)	Modulus E (MPa)	Poisson's ratio ν	Dumping ratio η
Concrete	2500	25000	0.15	0.04
Polyurethane (elastomer)	1170	25	0.50	0.08
Rubber chip	500	20	0.25	0.10

Equation (12) is a periodic function of the frequency ω with maximums in correspondence of the values:

$$\omega_n = (2n-1)\left(\frac{\pi}{2}\right)\left(\frac{\beta_j}{h}\right). \quad (13)$$

Figure 3 shows the diagram of amplification of the waves.

4. Modeling and Simulation: The Track-Subsoil Model

In this paragraph we show a numerical analysis, using a software for defined elements, on a two-dimensional modeling of the studied system.

4.1. Model Characteristics. In the proposed model the rail track is the conventional one, and the elements that compose it are (Figure 4)

(i) a protective compacted layer 30 cm thick of sand/gravel (called, in the Italian railways, *supercompact*);

(ii) a 12 cm subballast layer made of bituminous (hot-mix asphalt) concrete;

(iii) a traditional ballast layer 35 cm thick;

(iv) an embankment 60 cm high.

The dimensional characteristics of the elements above indicated are those requested by the Italian standard (RFI) for high speed lines.

Moreover, to analyze the propagation process of the vibrations in the soil, it has been considered a thickness of the support soil of the embankment equal to a total 5 m.

The materials properties used in the model were derived from tests and available experimentations in literature. Table 1 lists the physical-mechanical characteristics for the soil and track structure.

Finally a discontinuity (10 cm thick and 2 m deep) in the semispace at a given distance from the rail track (2 m from the embankment) is considered, considering the passage of a high speed locomotive (ETR 500) with 4 wheels for car.

The effects of discontinuity is estimated considering three different materials whose properties are shown in Table 2.

4.2. Finite Element Analyses of Train-Induced Ground Vibrations. The finite element simulations of train-induced ground vibrations was developed, using the ADINA software, considering a two-dimensional finite element model perpendicular to the track (two-dimensional perpendicular model).

The two-dimensional model is composed of 7517 elements and 8533 nodes (Figure 5). The elements consisted of four-node solid element for ballast, HMA subballast, protective layer and embankment and nine-node solid element for rail and sleeper. Furthermore, the rail pad was modeled with parallel discrete springs and dampers (spring constant $K = 11.2 \cdot 10^8$ N/m and damper constant $c = 12 \cdot 10^4$ Ns/m).

For these elements, under the accepted hypothesis of viscose-elastic behavior, the input parameters for the materials characterization, are the modulus of elasticity (E), Poisson's ratio (ν), density (ρ), α and β Rayleigh's coefficients for the definition of the damping matrix.

The acting forces are a sequence of axial loads, moving like the train (the loads are similar to those of an ETR 500 locomotive) (Figure 6).

The forces are applied using a time function that represents the time history of the force in the considered node. During the simulations the loads were applied four times, reproducing the passing of four axes. The loads can be thought of as triangular pulses distributed over the wheel-rail surface of contact as shown in Figure 7.

All the finite element analyses in this study were performed in the time domain. The time step of the analyses was fixed and set to 0.001 second.

Figure 8 shows the variation of velocity (y-direction and z-direction) of the middle node under truck and of a node at the distance of 1.5 m from the embankment. The orbits of

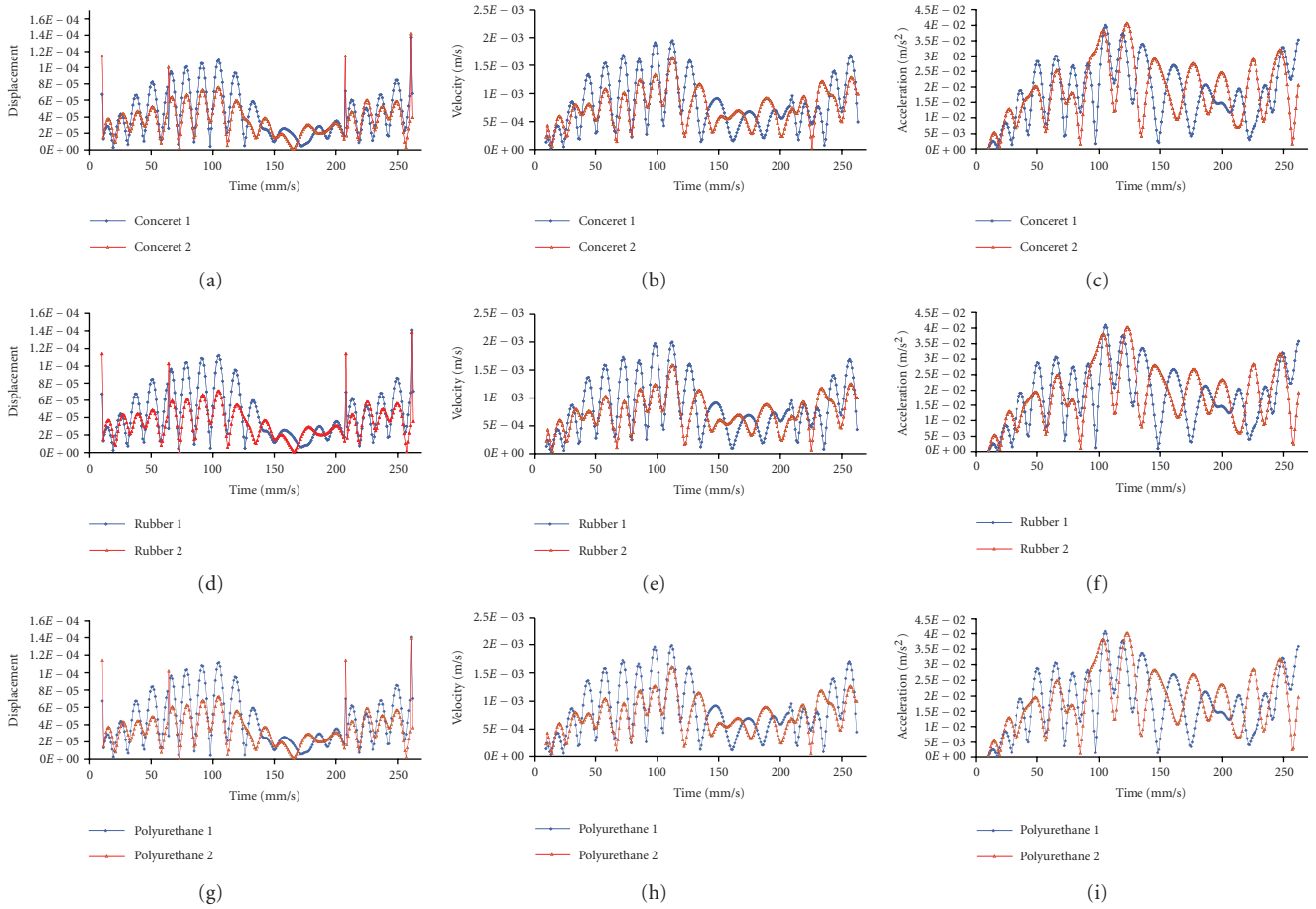

Figure 11: Trend of displacement, velocity, and acceleration in two nodes located before and after the barrier.

vertical to horizontal particle motions were mostly counter clockwise; this could indicate the presence of Rayleigh waves [11].

5. Results

The graphs of the outcomes of the various analyses are shown in Figures 9 and 10.

To estimate the effectiveness of the barrier we have estimated the dynamic characteristics (speed and acceleration) before and after the discontinuity, in correspondence of an eventual foundation plan of a building placed at a distance of 1.5 meters from the barrier.

As a general result of the analyses, as illustrated in Figures 9 and 11, for the considered loads, it is concluded that, when the load is travelling with the speed of 200 Km/h, concrete barriers provide a more efficient vibration shielding than the rubber and polyurethane barriers.

Figure 11 shows, for the three kinds of barrier, the course of the displacement, velocity, and acceleration in time.

The results given in Figures 9 and 11 supply useful information for the making of barriers, especially when it is required to respect regulation's limit for vibration, as expressed in terms of displacements and velocities (i.e., Italian regulation UNI 9916/2220).

6. Conclusions

The results of the proposed elaborations at the finite elements have been finalized to the assessment of the incidence of the barrier on the vibration state induced from the passage of a high speed locomotive. The response of three different materials for the barrier was confronted and the following conclusions can be made:

(i) concrete seems to provide a better reduction of the vibration. In spite of the greater density of the material it involves an increase of the reflection phenomena and a consequent increase of the phenomenon at the top side of the barrier (Figures 9 and 10);

(ii) polyurethane and rubber chip materials seem to respond in a similar way to the solicitations; however their damping contribution, in the analyzed geometric configuration, do not contribute meaningfully.

The results obtained were given with the use of different materials for the barrier, in identical geometrical conditions, in size and position of the proposed damping barriers. A follow up to the presented study, requiring further analyses, is in course, to estimate the influence of the position and of the thickness of the barriers on their dampening ability.

References

[1] S. Francois, L. Pyl, H. R. Masoumi, and G. Degrande, "The influence of dynamic soil-structure interaction on traffic induced vibrations in buildings," *Soil Dynamics and Earthquake Engineering*, vol. 27, no. 7, pp. 655–674, 2007.

[2] X. Sheng, C. J. C. Jones, and M. Petyt, "Ground vibration generated by a load moving along a railway track," *Journal of Sound and Vibration*, vol. 228, no. 1, pp. 129–156, 1999.

[3] G. Lombaert, G. Degrande, and D. Clouteau, "Numerical modelling of free field traffic-induced vibrations," *Soil Dynamics and Earthquake Engineering*, vol. 19, no. 7, pp. 473–488, 2000.

[4] P. Fiala, G. Degrande, and F. Augusztinovicz, "Numerical modelling of ground-borne noise and vibration in buildings due to surface rail traffic," *Journal of Sound and Vibration*, vol. 301, no. 3–5, pp. 718–738, 2007.

[5] W. Hubert, K. Friedrich, G. Pflanz, and G. Schmid, "Frequency- and time-domain BEM analysis of rigid track on a half-space with vibration barriers," *Meccanica*, vol. 36, no. 4, pp. 421–436, 2001.

[6] L. Andersen and S. R. K. Nielsen, "Reduction of ground vibration by means of barriers or soil improvement along a railway track," *Soil Dynamics and Earthquake Engineering*, vol. 25, no. 7–10, pp. 701–716, 2005.

[7] J. P. D. Hartog, *Mechanical Vibrations*, Dover, Oxford, UK; Oxford University Press, Oxford, UK, 1975.

[8] R. W. Clough and J. Penzien, *Dynamics of Structures*, McGraw-Hill, Singapore, 1985.

[9] E. Boschi and M. Dragoni, *Sismologia*, UTET, Torino, Italy, 2000.

[10] K. F. Graff, *Wave Motion in Elastic Solids*, Dover, Oxford, UK, 1991.

[11] L. Hall, "Simulations and analyses of train-induced ground vibrations in finite element models," *Soil Dynamics and Earthquake Engineering*, vol. 23, no. 5, pp. 403–413, 2003.

Hindawi Publishing Corporation
Advances in Acoustics and Vibration
Volume 2009, Article ID 942787, 12 pages
doi:10.1155/2009/942787

Research Article

Assessing the Open Trenches in Screening Railway Ground-Borne Vibrations by Means of Artificial Neural Network

Gaetano Di Mino,[1] Marinella Giunta,[2] and Ciro Maurizio Di Liberto[1]

[1] *Department DIIV, University of Palermo, Parco D'Orleans, 90100 Palermo, Italy*
[2] *Department DIMET, University Mediterranea of Reggio Calabria, Via Graziella Feo di Vito, 89100 Reggio Calabria, Italy*

Correspondence should be addressed to Marinella Giunta, marinella.giunta@unirc.it

Received 29 January 2009; Revised 28 May 2009; Accepted 13 October 2009

Recommended by Mohammad Tawfik

Reducing ground borne vibrations in urban areas is a very challenging task in railway transportation. Many mitigation measures can be considered and applied; among these open trenches are very effective. This paper deals with the study of the effect, in terms of reduction of vertical and horizontal displacements and velocities, of the open trenches. 2D FEM simulations have been performed and several open trench configurations have been analysed varying the main geometric features such as width and depth, distance from the rail, thickness of the soil layer over the rigid bedrock, type of the ground, ratio between the depth of the trench, and the thickness of the soil layer. For quantifying the influence of the above specified parameters in reducing ground-borne vibrations an analysis using artificial neural networks (ANNs) has been carried out. Results show that among the geometric parameters the role of the depth of the trench is very significant; however the influence of the depth must be also evaluated in relation to the thickness of the soil layer.

1. Introduction

The problem of the ground-borne vibrations induced by railway traffic has received an increasing interest in the recent years becoming a relevant scientific and technical research area.

Due to the frequent construction of high-speed railways and mass rapid transit systems worldwide, most highly developed cities or metropolitan areas have encountered the problem that the rail tracks inevitably come cross or close to vibration-sensitive sites, as discussed by Hung and Yang [1, 2].

The economical and environmental aspects of the issue require a careful assessment of the problem before the construction of new rail tracks or the upgrading of the existing ones for heavier and faster traffic.

The main source of excitation of the track is represented by the vertical force determined by the wheel-rail interaction during the passage of the train. Vibrations can be amplified by the passage of trains due to the surface irregularities of wheels and rails, by the rise and fall of axles over sleepers, and by the propagation of deformation patterns in the track and ground. Such vibrations are transmitted through the track structure, including rails, sleepers, ballast, and sublayers and propagate as waves through the soil medium [3].

The study of the ground-borne vibrations requires the consideration of four main components: the "source," that generate the vibration, that is, the excitation caused by the motion of the trains over rails with irregular surfaces, the "propagation path" through the soil medium, the "receiver," that is, the nearby buildings, and finally the "interceptor," that is, wave barriers, such as piles, in-filled and open trenches, and isolation pads.

At each component is related one specific phase of the process of the transmission of the vibrations and in particular the generation, the transmission, the reception, and the interception.

In regard to this last phase, three groups of mitigation measures can be considered:

(i) mitigations in the source, that include all types of interventions in the railway structures (active isolation);

(ii) mitigations in the path, such as barriers to the waves propagation from the source to the receiver (in-filled and open trenches, lime cements columns); these barriers provide an active isolation when they are close to the source, and a passive one when they are far away;

(iii) mitigations to the receiver, that include all the measures aimed at reducing the effects on the buildings (passive isolation) or on the other vibration-sensitive sites.

Among the mitigation measures in the path, the open trenches have exhibited a good performance on the screening of the vibrations but, to achieve this effect, it is very important to assign it the proper dimensions.

2. Previous Studies

The first experimental surveys on the effectiveness of open and in-filled trenches were carried out by Barkam (1962) [4]. He showed that their effectiveness increases with increasing the depth and the distance for raising frequencies.

In regard to the continuous barriers also Woods [3] showed the influence of the depth and the distance from the vibratory source. He also demonstrated that the passive isolation is better than the active for screening the *P* - body and *S*-body waves while the active isolation is more suitable for the screening of the Rayleigh waves; moreover he highlighted that the most relevant geometric parameter in the screening process is the ratio between depth barrier and Rayleigh wavelength.

Several experimental surveys stated that the best screening performance takes place when the depth of the trench is equal to the wavelength while the width of the trench is small [3–10].

Numerous researches on the effectiveness of the barriers have been carried out using FEM and BEM modelling [11–16].

In particular, Beskos et al. [11] employed boundary element method (BEM) to study open and in-filled trenches as well as pile wave barriers. Ahmad and Al-Hussaini [13] proposed a simplified design methodology for vibration screening of machine foundations by trenches using 2D BEM.

Adam and Estorff (2005) [6] inspected the effectiveness of open and in-filled trenches in reducing the six-storey building vibrations due to passing trains using a two-dimensional FEM analysis.

Yang and Hung (1997) [1, 2] combined the finite and infinite elements to investigate the effect of trenches and elastic foundations in reducing train-induced vibration.

Few works focus on the effectiveness of barriers in full scale.

The most important application is based on Gas Cushion Method that consists in a vertical panels filled of gas and flexible cushion with very low impedance installed in a trench having a great depth [17]. In Gnarp, Sweden 1984, the first application of these barriers was carried out in order to screen a sensitive building from railway ground borne vibrations. The effectiveness of this application reached an attenuation value of about 70%.

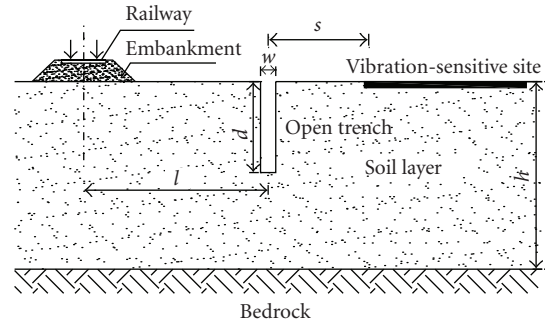

Figure 1: Schematic of the position of the open trench.

Table 1: Geometric parameters of the trenches.

Width w (m)	Distance from the rail l (m)	Distance from the site s (m)
0.5	8	19
1.0	12	15
1.5	16	11
2.5	20	7
—	24	3

Table 2: Depth of the trench and ratio depth/thickness of layer.

Parameters	Assumed values
d (m)	2, 5, 8, 11,14
d/h	1/5, 1/2, 2/3

3. Problem Formulation and Basic Assumptions

In this work the screening performance of open trenches, excavated in a soil layer over a bedrock, has been studied. By applying a 2D FEM model, an extensive analysis has been carried out to the aim of determining the contribution of the main geometric parameters of the trenches in the interception of the vibrations. The geometric characteristics assumed to be variable parameters are width (w), depth (d), distance from the rail (l), distance from the vibration-sensitive site (s), thickness of the soil layer over the rigid base (h), and ratio between the depth of the trench and the thickness of the soil layer (d/h) (see Figure 1).

The study has been carried out considering different scenarios obtained by varying the above specified geometric parameters of the trenches and the mechanical and geometric characteristics of the soil medium. The values attributed to the geometric features are summarised in Table 1, while the geometric conditions of the soil medium have been set up according to the Table 2.

Two types of unsaturated soil, labelled, according to the classification of Eurocode 8, respectively, ground type C (medium dense sand) and ground type D (firm clay), have been considered. These soils have been characterised by the

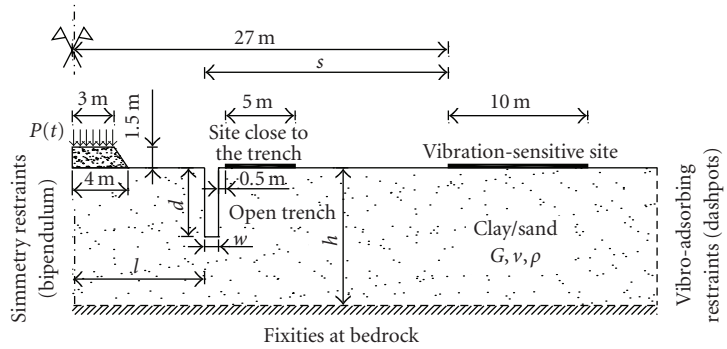

Figure 2: Modelling scheme.

shear modulus (G), the Poisson's ratio (ν), the mass density (ρ), the damping ratio (ξ), and the shear and the Rayleigh's wave velocities (V_s, V_r). The values assigned to each of these parameters are shown in Table 3.

The value of the damping ratio for clay and sand has been selected according to the results of an Italian comprehensive review [18] that analyses a great number of experimental results (44 international researches carried out in the last 30 years) and concludes that although a considerable scatter of the experimental points exists, for deformations lower than 0.001%, the damping ratio has a tendency to increase according to the plasticity index.

By combining all the parameters, 540 scenarios have been obtained and investigated. The propagation and interception of ground-borne vibrations for each scenario have been modelled by means of the finite elements method. The scheme adopted is shown in Figure 2. The 2D model has been assumed to be symmetric in respect to the railway line.

It has been also established that the railway line is sited over an embankment 1.5 m high and with escarpment's slope of 2/3; the geotechnical parameters of the embankment are $G = 125$ MPa, $\rho = 2000\,\text{N/m}^4\,\text{s}^2$, and $\nu = 0.33$.

For each scenario the following responses have been obtained: vertical (dir. z) and horizontal (dir. y) displacements and vertical (dir. z) and horizontal (dir. y) velocities. In particular, these parameters have been calculated in two areas:

(a) in a "vibration-sensitive site," large 10 m and far away 27 m from the symmetry axis of the railway;

(b) in a zone, in the following called "site close to the trench," 5 m wide and sited far away 0.5 m from the trench.

The dimensions assigned to the two sites are well suited to be comparable with the dimensions of receptors such us buildings.

The study of the response in this last site allowed to verify the effectiveness of the open trench as passive isolation.

4. Finite Element Modelling

The propagation of vibrations is a typical three-dimensional issue, specially in railway field where the train acts as a series of incoherent point source rather than a fully coherent line source. So three-dimensional models are certainly more suitable to predict the absolute vibration but require computation times not always consistent with extensive analyses.

Andersen and Jones [19] performed analyses 2D-3D FEM and BEM and stated that 2D models provide results qualitatively comparable with those obtained using 3D models in a wide range of frequencies.

In the light of this, the 2D model has been considered appropriate to output results consistent with the aim of the present study.

4.1. Material Constitutive Model and Type of FEM Elements Applied. Linear viscoelastic constitutive model for the embankment and the soil medium materials has been adopted to carry out the investigation, according to some previous studies [20, 21]. Both the embankment and the soil medium have been meshed with triangular elements having 6 nodes. The mechanical parameters assigned to each element are the Young modulus E, Poisson's ratio ν, and the mass density ρ, while the damping behaviour has been introduced by means of the Rayleigh coefficients α and β. The damping matrix [C] has been defined on the basis of the quoted Rayleigh coefficients α and β.

The presence in the analysed scheme of a rigid base has been taking into account by introducing in the model fixities at bedrock.

4.2. Modelling of the Rail Source. The railway source has been modelled applying in the surface of the embankment below the ballast a stress having a value equal to the dynamic stress produced in the contact surface ballast-embankment.

In particular, according to [6], two concentrated linear loads acting over the rails have been considered. The time history of each load consists of four consecutive impulses; each impulse have a time duration of 0.02 seconds and an amplitude equal to 1000 KN. Since only the embankment has been modelled, the dynamic pressure produced by the linear loads in the contact surface ballast/embankment, having dimensions of about $2,5\,\text{m} \times 1\,\text{m}$, has been fixed in $400\,\text{kN/m}^2$ (Figure 3) while its time history is the one plotted in Figure 4.

Table 3: Mechanical characteristics of the soil medium.

Type of soil	G (MN/m^2)	ρ (N/m^4 sec^2)	ν	ξ	V_s (m/sec)	V_r (m/sec)
Clay	20.7	1583.8	0.3	0.06	114.3	108.1
Sand	138	1682.8	0.3	0.04	286.3	270.9

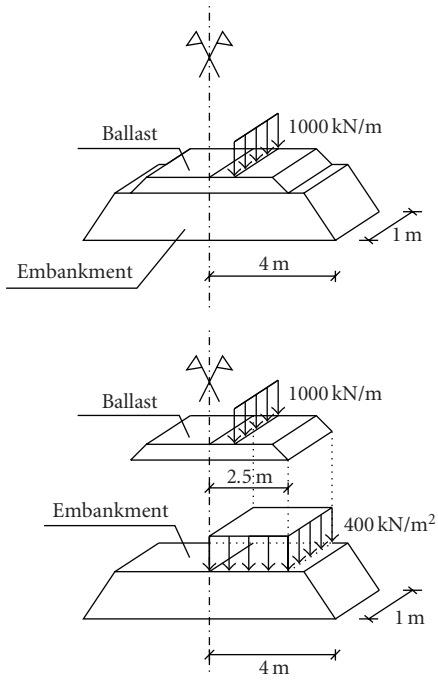

Figure 3: Loading conditions.

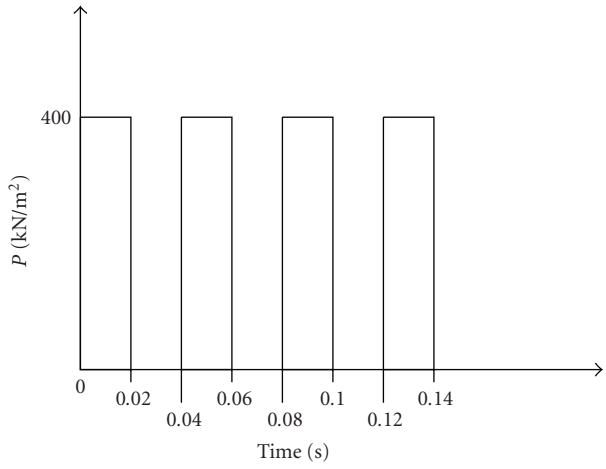

Figure 4: Time history of the rail force.

The applied load function gives a significant contribution for the frequencies included in the range from 20 to 35 Hz, with a central frequency of about 27 Hz. This range, in the present study-case, is representative of the frequencies produced by the passage of a freight train at the velocity of 60 km/h, and having a boogie axle distance of 9 m. The load can appear overabundant but it takes into account the dynamic amplification factor by the shortest wavelength [6, 22].

4.3. Finite Element Mesh. The definition of the model mesh is in general a compromise between the necessity to restrict the number of the elements and that to limit their dimensions. However, the element's dimension must be accurately chosen in order to adequately represent the deformed shape associated to the wave lengths λ at the different harmonic frequencies f imputed.

If $f_{\max}$ is the greatest frequency of the significant components of the Fourier spectrum and V_j is the propagation speed of the waves (P -waves, S-waves, or R-waves) in the material, the dimension of the mesh element for the material should satisfy the following relation:

$$d \leq \frac{\lambda_{\min}}{k} = \frac{V_j}{k \cdot f_{\max}}, \tag{1}$$

where k is a coefficient ranging from 4 to 10 according to the type of finite element and to its shape function [23].

In the light of this, the maximum dimension of the element has been defined in the following way:

(i) on the basis of the material properties, there has been calculated the minimum wave propagation velocity for the considered domain; that is, for the superficial elements there has been considered the Rayleigh's velocity V_r, for the elements close to deep source the shear velocity V_s;

(ii) there has been defined the maximum value of the appropriate frequency $f_{\max}$; that is, in this study, according to the railway source model, $f_{\max}$ has been set up equal to 35 Hz;

(iii) there has been calculated, using the expression (1), the minimal dimension of the element.

By applying this procedure to the two types of soil medium, there has been obtained

Clay $\Rightarrow$ $V_r = 108.16$ m/sec; $f_{\max} = 35$ Hz; $k = 6 \Rightarrow d_A \leq 0.51$ m;

Sand $\Rightarrow$ $V_r = 270.94$ m/sec; $f_{\max} = 35$ Hz; $k = 6 \Rightarrow d_S \leq 1.29$ m.

By considering these dimensions, the mesh has been made as follows:

(i) in the part of the model where the response is significant to the aim of the study, corresponding to a strip, large about 40 m and 40 m deep, closest to the rail track, a maximum dimension of 0.5 m has been assigned to the elements; this mesh has been designed to be denser in this focal area in order to achieve a good precision;

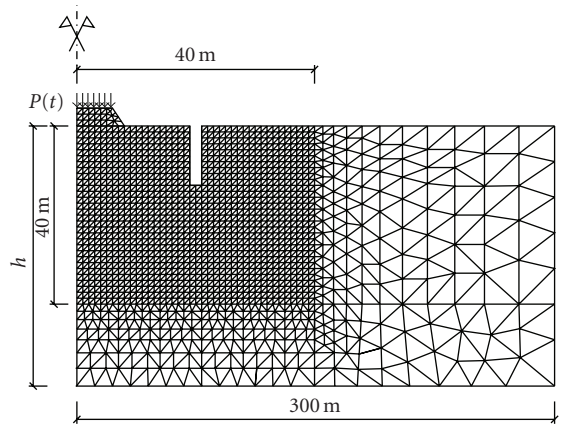

Figure 5: Scheme of FEM mesh.

(ii) in the part of the model included between the quoted part and the lower edge a maximum dimension of 0.5 m has been assigned when the clayey soil has been analysed, while in the case of sandy soil the dimensions of the element gradually increase until 1.5 m near the lower edge;

(iii) externally to the above mentioned areas, the dimensions of the elements increase gradually reaching the value of 3 m in proximity of the vertical boundary far 300 m from the symmetry axis.

The linear variation of the mesh dimensions, from the side $y = 40$ m to the boundary, has been chosen in accordance with other similar works [24, 25].

The scheme of the finite element mesh is shown in Figure 5.

It can be observed that outside the zone of interest ($40\,\text{m} \times 40\,\text{m}$), the growth of the dimensions of the element in connection with the time step does not produce effects in the part of the model where is sited the trench; in fact, the vibratory waves, also when undergo reflections in correspondence of the vertical boundary right hand, cannot reach this zone before the end of the analysis.

4.4. Courant's Condition. The time step integration has been assigned taking into account the Courant condition, that defines the maximum time step as [26]

$$\frac{V_j \cdot \Delta t}{h} = C, \quad C \leq 1 \tag{2}$$

in which V_j is the velocity of the considered wave, h is the maximum spatial displacement admitted for the perturbation that in FEM models is generally assumed equal to the dimension of the mesh, and C is the Courant number.

It should be noted that in the problems involving different type of waves, like the propagation of the P and S waves in the elastic space, the time step is imposed by the greatest propagation velocity, while the element's dimensions depend on the lowest velocity. So, a great difference between the greatest and the lowest propagation velocity requires a small finite element and a short-time step.

Having in mind this, in this task there has been assumed that

Clay $\Rightarrow$ $V_p = 191.55$ m/sec, $d_{A,\min} = 0.5$ m $\Rightarrow$ $\Delta t \leq 0.0026$ sec; there has been chosen $\Delta t = 0.002$ sec.

Sand $\Rightarrow$ $V_p = 479.83$ m/sec, $d_{S,\min} = 0.5$ m $\Rightarrow$ $\Delta t \leq 0.00104$ sec; there has been chosen $\Delta t = 0.001$ sec.

In both cases of clay and sand the FEM simulations have been performed in a time of $T = 0.75$ sec; this time is sufficient to permit the complete passage of the dynamic perturbation in the examined zone.

4.5. Boundary Condition. Boundary conditions have been imposed in the model in consideration of the geometric and mechanical conditions of symmetry and taking into account the need to limit the errors, namely, the difference existing between the theoretical value of the stress in a point of the boundary and the value obtained in presence of the restraints.

FE calculations need a self-consistent simulation area to operate on. Especially in the case of wave propagation, special boundary conditions have to be incorporated into the calculation scheme [27]. Many authors have proposed special absorbing boundary conditions (ABCs) for the FE calculation of elastic waves. In these works the boundary conditions suggested from Lysmer and Kuhlemeyer have been applied [28]:

$$\begin{aligned} \sigma &= -\rho c_d V_n, \\ \tau &= -\rho c_s V_t, \end{aligned} \tag{3}$$

where σ and τ are the normal and the shear stress, ρ the material density, and c_d and c_s the longitudinal and the shear wave velocities of the transmitting media. These equations reveal that the magnitude of these stresses at the boundaries is proportional to the particle velocities in the normal (V_n) and in the tangential (V_t) directions. Lysmer's dampers placed on the artificial boundary are effective in reducing unwanted wave reflections if the boundary of the finite element mesh is sufficiently far outward.

In the light of this, there has been applied

(i) in the symmetry edge, symmetry restraints like bipendulum in y direction;

(ii) in the lower edge, fixities at the bedrock;

(iii) in the right-side edge, Lysmer's dampers in the directions y and z.

The right-side edges have been applied at a distance of 300 m from the source; the errors obtained in the boundary have been

(i) $\varepsilon(\sigma_n) = 0.10\%$ and $\varepsilon(\tau) = 0.45\%$, in the case of the clayey soil medium;

(ii) $\varepsilon(\sigma_n) = 0.26\%$ and $\varepsilon(\tau) = 1.12\%$, in the case of the sandy soil medium.

4.6. The Determination of the Rayleigh Damping Coefficients α and β. In an FEM model the damping behaviour can be

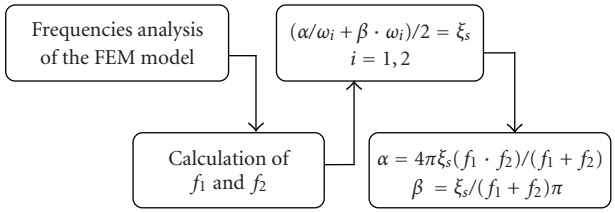

Figure 6: Rayleigh's parameters determination.

modelled using Rayleigh's method. The damping matrix can be obtained from the following relation:

$$[C] = \alpha[M] + \beta[K], \tag{4}$$

where $[M]$ and $[K]$ are, respectively, the mass matrix and the stiffness matrix.

The α and β damping coefficients [23, 29] have been determined following the procedure described below and shown in Figure 4.

(i) For each 2D model, a frequency analysis has been carried out and the first resonance frequency f_1 has been calculated.

(ii) There has been calculated the frequency f_2 by means of the relation $f_2 = nf_1$, where n is the first odd number greater than the ratio f_i/f_1, being f_i the dominant frequency. In this case f_i has been fixed equal to 27 Hz, like the medium frequency of the load function.

(iii) Rayleigh's parameters value has been calculated by establishing that, for frequencies equal to f_1 and f_2, the damping coefficient of the element must be equal to the value ξ_s, which is proper to the examined soil. In this way there has been introduced a subdamping for the frequencies ranging from f_1 to f_2 and a superdamping for the other frequencies not included in this range.

For the clayey soil Rayleigh's parameters have been calculated assuming that a damping ratio ξ_s is equal to 0.06, while for the sandy one there has been assumed that ξ_s is equal to 0.04.

In Figures 7 and 8, we can see examples of damping diagrams for clayey and sandy soil medium.

4.7. Validation Model. In order to validate the model, results by Beskos et al. [11] have been considered and used. Results concern an open trench having a depth of 2.8 m ($1\lambda_r$) and a width of 0.28 m ($0.1\lambda_r$); it is made in an elastic half-space at a distance of 10.04 m ($5\lambda_r$) from the axis of a rigid foundation having a width of 0.7 m and subjected to a harmonic load with frequency of 50 Hz.

In particular the comparison between the results given by the proposed 2D FEM model and the Beskos one has been performed considering the trend of the attenuation ratio A_r versus the normalized distance y/λ_r, where λ_r is the length of Rayleigh's waves generated from the source and y the horizontal distance of the generic point from the axis of the source.

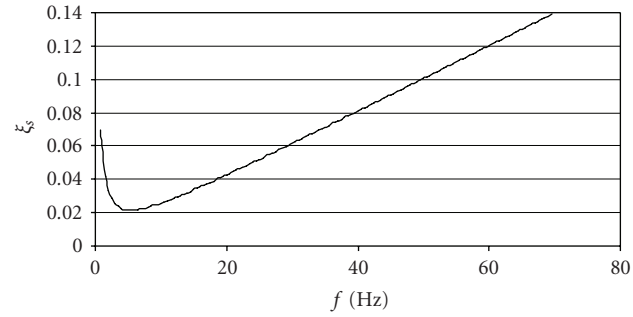

$\alpha = 0.733542936$
$\beta = 0.000632546$

Figure 7: Damping ratio ξ_s versus frequency for clay bank of 25 m depth.

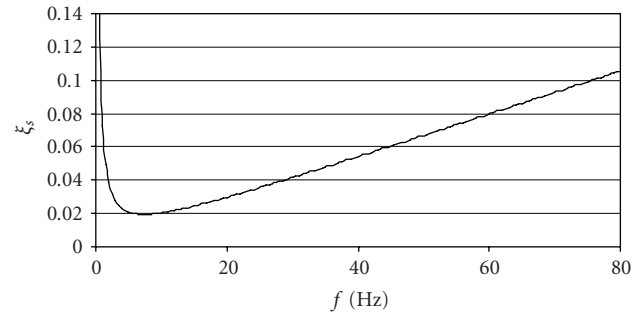

$\alpha = 0.90001977$
$\beta = 0.000416658$

Figure 8: Damping ratio ξ_s versus frequency for sand bank of 40 m depth.

In each point of both vibration-sensitive site and site close to the trench the attenuation ratio A_r has been defined as the ratio between the maximum value of the kinematic parameters (y and z displacements and y and z velocities) in presence of trench and the same value without trench:

$$A_r = (\text{max value of the kinematic parameters in a point with trench})/(\text{max value of the kinematic parameters in a point without trench}). \tag{5}$$

The attenuation ratio has been calculated not only for the vertical displacement (dir. z), as it is usual in literature, but also for the horizontal displacement (dir y) and for the horizontal and vertical velocities.

Since the sites are not points but large zones and considering the evolution of the attenuation ratio increasing distance (Figure 7), the effectiveness of the trench in these sites has been evaluated in terms of average attenuation ratio:

$$A_m = \frac{1}{C}\int_o^c A_r(y)\,dy, \tag{6}$$

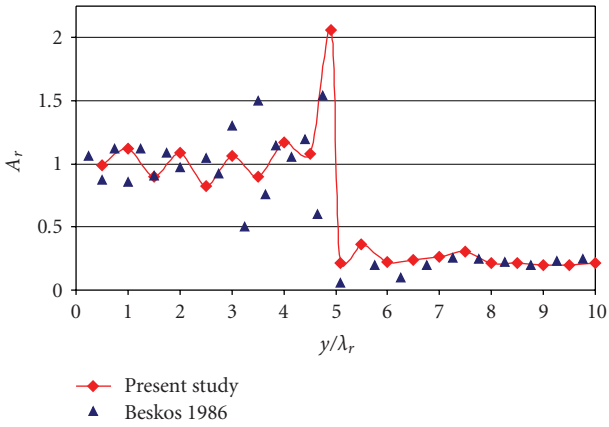

Figure 9: Model results versus Beskos results.

where C is the length of the investigated zone (equal to 10 m for vibration sensitive site and 5 m for site close to the trench).

As it can see in Figure 9, a good agreement between the numerical results from Beskos simulation and the ones obtained with the proposed model has been achieved. The model has given good results also in others experimental applications [29] and thus it has been applied in the present study.

4.8. Results. From the numerical FEM simulations of the 540 scenarios the values of the displacements and velocities have been obtained; the minimum and the maximum values reached in the significant points are summarised in Table 4.

In Figure 10 two samples of time history of displacement and velocity in a point are plotted.

When the horizontal propagation of in-plane waves is considered, the Rayleigh waves and the P-waves are the main causes of the ground motion.

At quite distance ($5\lambda_r$) from a vibratory source the ground motion is due to the Rayleigh waves energy.

If an open trench is excavated near the source, the incidence of the waves on this obstacle (discontinuity field) gives rise to reflected and transmitted body waves. Behind the open trench, as the distance increases, the transmitted P-waves get partially into Rayleigh waves (phenomenon known as mode conversion). Therefore, the Rayleigh waves are the main cause of the ground motion [13].

According to this phenomenon the results show a great attenuation of displacement and velocity passing from the site close to the trench to the vibration sensitive site (see Table 4).

To evaluate the effectiveness of the trench there has been adopted the very strict following criterion: a trench is effective in screening the ground borne vibration if the value of the attenuation ratio is lower than 0.4 for every considered displacement and velocity.

The analysis of the FEM results for the two types of ground has been performed having in mind this criterion.

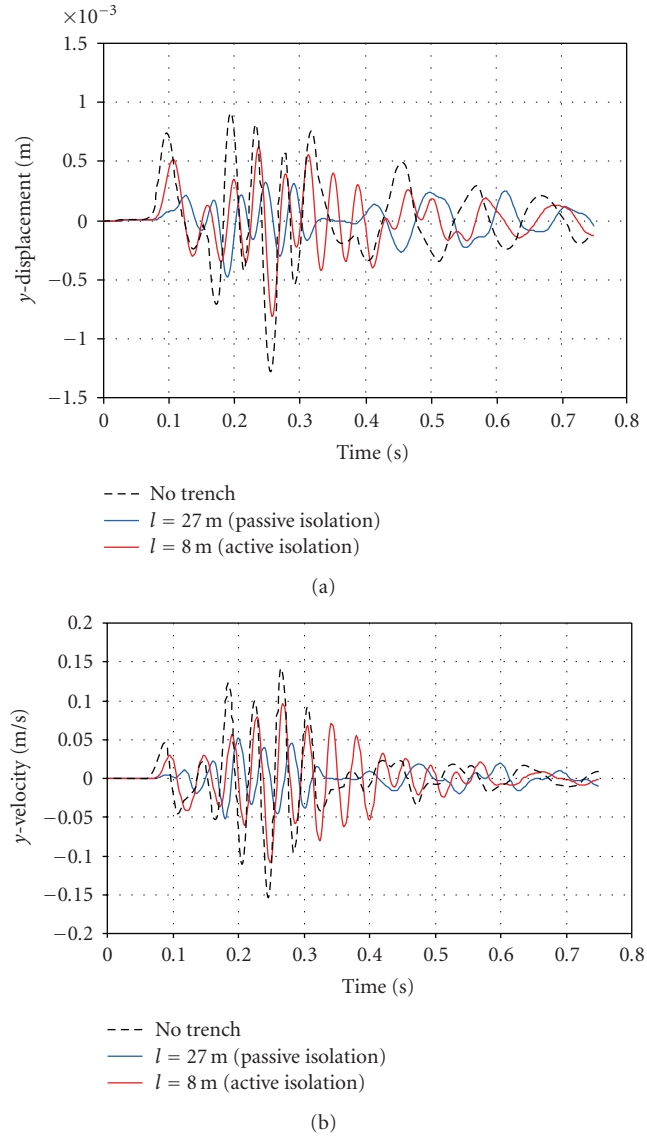

Figure 10: Samples of results in a point in case of sandy soil.

The results give some indications for the design of the open trenches in both cases of site close to the trench and vibration-sensitive site (see Tables 5 and 6).

The effect of frequency is fully taken into account by normalizing the open trench dimensions with respect to the Rayleigh wavelength.

The obtained results are very strict in regard to the dimensions and the position of the trench because these features depend on the ratio d/h and so on the finite value of the layer thickness.

For instance, in clayey soil results show that the trench is effective if it is 5 m deep and far away at least 12 m from the source, for thickness layer equal to 10 m or 2 m deep and far away at least 24 m from source, and for layer thickness equal to 3 m.

Some results of the parametric studies carried out are plotted in Figure 11. It can be seen that the efficiency of

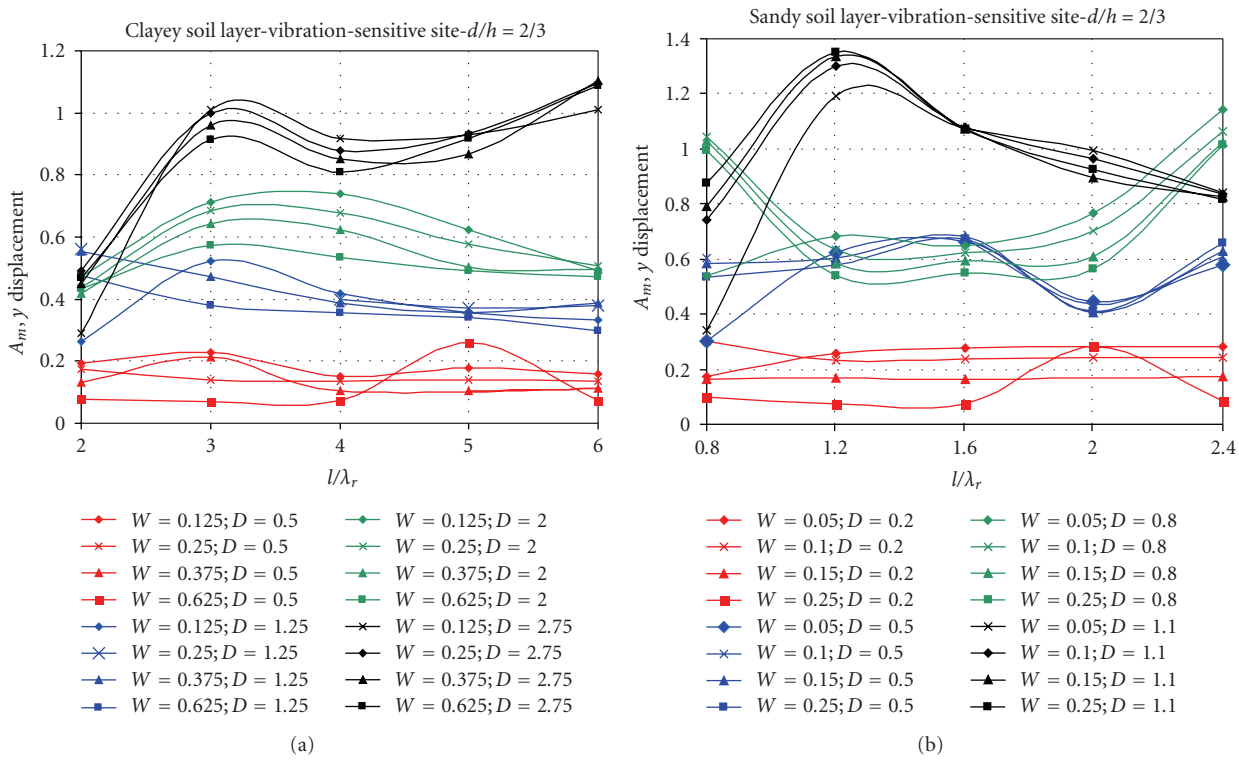

Figure 11: Some results of parametric study ($W = w/\lambda_r$, $D = d/\lambda_r$).

Table 4: Maximum and minimum values of displacements and velocities.

Site close to the trench				
Soil type	Velocity dir. y min max (m/sec)	Velocity dir. z min max (m/sec)	Displacement dir. y min max (m)	Displacement dir. z min max (m)
Sand	0.13	0.09	0.00098	0.00056
	0.35	0.25	0.00252	0.00619
Clay	0.16	0.13	0.00564	0.00369
	0.29	0.48	0.01084	0.02509
Site vibration-sensitive				
Soil type	Velocity dir. y min max (m/sec)	Velocity dir. z min max (m/sec)	Displacement dir. y min max (m)	Displacement dir. z min max (m)
Sand	0.052	0.035	0.00078	0.00009
	0.21	0.20	0.00198	0.00341
Clay	0.035	0.028	0.00177	0.00040
	0.27	0.30	0.01084	0.01714

Table 5: Design parameters for trench—site close to the trench.

d/h	Clayey soil layer [$\lambda_r = 4,00$ m]			Sandy soil layer [$\lambda_r = 10,00$ m]		
	d	l	w	d	l	w
1/5	—	—	—	$0.2\lambda_r$	$2\lambda_r$	$\leq 0.1\lambda_r$
1/2	$1.25\lambda_r$	$>3\lambda_r$	all	$0.5\lambda_r$	$\geq 1.2\lambda_r$	all
2/3	$<2.75\lambda_r$	$6\lambda_r$	all	$0.2\lambda_r$	all	all

Table 6: Design parameters for trench—vibration-sensitive site.

d/h	Clayey soil layer [$\lambda_r = 4,00$ m]			Sandy soil layer [$\lambda_r = 10,00$ m]		
	d	l	w	d	l	w
1/5	—	—	—	$0.2\lambda_r$	$0.8\lambda_r$	$0.05\lambda_r$
1/2	$1.25\lambda_r$	$>3\lambda_r$	all	$0.5\lambda_r$	$0.8\lambda_r$	$0.05\lambda_r$
2/3	$0.5\lambda_r$	all	all	$0.2\lambda_r$	$\geq 0.8\lambda_r$	all

Table 7: Percentage of contribution to the attenuation of the displacements—site close to the trench.

Attenuation ratio for horizontal displacements		Attenuation ratio for vertical displacements	
Parameters	Percentage of contribution	Parameters	Percentage of contribution
d	28.00%	d	31.00%
d/h	26.00%	d/h	28.00%
V_s	17.00%	l	14.50%
ξ	15.50%	V_s	13.00%
l	10.50%	ξ	9.00%
w	3.00%	w	4.50%

Table 8: Percentage of contribution to the attenuation of the velocities—site close to the trench.

Attenuation ratio for horizontal velocities		Attenuation ratio for vertical velocities	
Parameters	Percentage of contribution	Parameters	Percentage of contribution
d	31.00%	d	27.00%
d/h	23.00%	d/h	26.00%
ξ	17.00%	l	15.00%
l	14.00%	V_s	13.50%
V_s	11.00%	ξ	11.50%
w	4.00%	w	7.00%

Table 9: Percentage of contribution to the attenuation of the displacements—vibration-sensitive site.

Attenuation ratio for horizontal displacements		Attenuation ratio for vertical displacements	
Parameters	Percentage of contribution	Parameters	Percentage of contribution
d	36.00%	d	42.00%
d/h	30.00%	d/h	26.00%
V_s	13.00%	V_s	12.00%
ξ	11.00%	ξ	11.00%
l	7.00%	l	7.00%
w	3.00%	w	2.00%

Table 10: Percentage of contribution to the attenuation of the velocities—vibration-sensitive site.

Attenuation ratio for horizontal velocities		Attenuation ratio for vertical velocities	
Parameters	Percentage of contribution	Parameters	Percentage of contribution
d	34.00%	d	35.00%
d/h	27.00%	d/h	22.50%
V_s	17.00%	V_s	16.00%
ξ	14.00%	ξ	15.50%
l	5.00%	l	8.00%
w	3.00%	w	3.00%

the trench is in general independent from the width of the trench; therefore it can be established according to technical-economic criteria, while the depth affects significantly the attenuation process.

5. ANNs Analysis

5.1. Introduction. Artificial neural networks (ANNs) are a tool that simulates the biological processes and, as demonstrated by the wide applications in engineering field, they are able to solve functional mapping problems. ANNs are an assemblage of mathematical simple computational elements called neurons.

In particular the back propagation neural network (BPNN) is a collection of neurons distributed over an input layer, that contain the input variables of the problem, one or more hidden layers with a certain number of nodes, and an output layer with a number of nodes equal to the output variables. The nodes between layers are connected by the links having a weight that describes quantitatively the strength of the connection.

A significant effort is required in the selection of the ANN architecture, particularly, as it is obvious, in the definition of the hidden layers and the corresponding nodes.

The learning process utilized for this type of ANN is the "back-propagation learning" which consists in an error minimization technique [30]. Inputs from the mapping examples are propagated through each layer and give the outputs that are compared with the correct answers; the difference represents the error. This error is propagated backward through the network and the connection weights are individually adjusted so as to reduce and minimize the error.

To ensure an efficient convergence and the desired performance of the trained network, several parameters are incorporated in the training phase. These parameters include the learning rate, the momentum term, and the number of training iterations. The learning rate is a factor that proportions the amount of the adjustment applied at each time the weight is updated. The use of a momentum term could carry the weight change process through one or more local minima and get it into global minima. The early stopping method and the number of training epochs determine the training stop criteria [31].

5.2. Neural Network Application. For the present application the neural networks have been trained and tested with the data given from the FEM modelling of the 540 scenarios.

In details, the input data chosen for the neural analysis have been 6 and precisely: width of the trench (w), depth of the trench (d), ratio of depth of the trench to thickness of the soil layer (d/h), shear wave velocity (V_s), and damping ratio (ξ), while the output data have been the average attenuation ratio of the horizontal and vertical displacements, and the average attenuation ratio of the horizontal and the vertical velocity. In fact, the neural network application aimed at evaluating the contribution of each input factor in the attenuation of the displacements and velocities.

To this purpose a great number of trial ANNs with one, two, and three hidden layer have been trained to evaluate the performance of different network architectures in the comprehension and generalisation of the problem.

The training procedure has been tested using a test set of examples having a percentage of 10% of the training set; the prediction performance of the developed model has been exhibited in the test set.

The error term, represented by the mean square error (RMS error), computed for the validation input-output pairs, has been monitored during the training process of the networks. The error normally decreases during the initial phase of training. However, when the network begins to overfit the data (a situation arising when ANN works well only with the training data), the error on the validation set will typically begin to increase. When the validation error increased for a specified number of iterations, training was stopped and the weights at the minimum of the validation error were saved. This point is the point of maximum generalization [30].

Considering this, networks with errors comprising in the following ranges have been selected: RMS error training set: 0.02–0.1; RMS error test set: 0.02–0.12; Correlation training set: 0.5–1. It has been stated that the neural networks having the training parameters included in the quoted ranges provide acceptable results.

The analysis of the training and the testing phases of these neural networks allowed to evaluate the percentage of contribution of each input factor in the output determination. In other terms the study allowed to assess qualitatively and quantitatively the influence of the features of the trench and the soil medium in the attenuation process of ground-borne vibrations.

5.3. Results. The results obtained for both vibration-sensitive site and site close to the trench are explained in the following.

5.3.1. Site Close to the Trench. Regarding the attenuation ratio of the horizontal and vertical displacements, the neural network analysis has given the percentages of contribution summarised in Tables 7 and 8.

By analysing the results it can be deduced that for both vertical and horizontal displacements the percentage of contribution to the attenuation ratio of the depth of the trench d and of the ratio d/h is close to the 60%. The influence of the terrain, expressed by V_s and ξ, ranges from 32% for horizontal displacements to about 22% for vertical displacements. The influence of the distance of the trench from rail l is evaluated around the 10%–14% while the width of trench w has a marginal weight of about 3–5%.

Regarding the attenuation of the velocities the hierarchy of influence of the parameters seems to be the same of the displacements: the influence of the depth of the trench d and of the ratio d/h is preponderant (about 50%), while the influence of the terrain is evaluated around the 25%–28% while, in contrast to the results found for the displacements, there appears significant the distance of the trench from rail l that contributes for around the 15% to the attenuation

process. The width of the trench w, even if with the different weights for horizontal (4%) and vertical (7%) velocities, gives a poor contribution to the attenuation phenomenon.

5.3.2. Vibration-Sensitive Site. The percentages of contribution to the attenuation ratio of the horizontal and vertical displacements are summarised in Tables 9 and 10.

In this site the influence of the depth of the trench d on the attenuation ratio of the vertical and horizontal displacements is very significant (36%–42%) and together with the ratio d/h seems to govern preponderantly the attenuation process. The other factors (V_s, ξ, l) have an influence comparable (each ranged from 7 to 13%) and lesser than d and d/h. Once again the width w of the trench is not much significant.

Regarding the attenuation ratio of the horizontal and vertical velocities the trend is the same of the displacements but the contribution of the terrain's parameters (V_s and ξ) is higher (about 30%). The distance of the vibration sensitive site from the source l and even more the width w of the trench have a low contribution.

6. Conclusions

In order to intercept the elastic waves and in particular Rayleigh's ones generated by the moving source from reaching buildings between the railways and the sensitive site, vibration screening may be established by means of the open trenches. Several factors determine the effectiveness of the open trenches in the screening of the ground borne vibrations in soil medium.

In the present work, as outcomes of an FEM modelling of the problem and of an analysis carried out by means of the neural network, the weights of the main geometric features of both the trench and the soil medium have been established.

The main conclusions of this application are the following:

(i) first of all, the screening performance of the trench is mainly affected by the depth of the trench, in both cases of site close to the trench and vibration-sensitive site. From ANN analysis the percentage of contribution of this geometric parameter in reducing displacements and velocities of vibration reached the 25%–35%;

(ii) layer thickness increasing, the attenuation ratio increases according to the depth of the trench; to this reason, it appears very noteworthy in the topic not only the depth d of the trench but also the ratio d/h (depth of the trench/ thickness of the bank); the two parameters d and d/h govern the attenuation process with a percentage of contribution more than 50%;

(iii) to the aim of evaluating the effectiveness of the trench we have to analyse all the kinematic parameters and not only the displacement in one direction, generally the direction z; in fact, some geometric configurations able to reduce one kinematic parameters can be inefficient with regard to the attenuation of the other kinematic parameters.

References

[1] H.-H. Hung and Y.-B. Yang, "A review of researches on ground-borne vibrations with emphasis on those induced by trains," *Proceedings of the National Science Council, Republic of China, Part A*, vol. 25, no. 1, pp. 1–16, 2001.

[2] Y.-B. Yang and H.-H. Hung, "A parametric study of wave barriers for reduction of train-induced vibrations," *International Journal for Numerical Methods in Engineering*, vol. 40, no. 20, pp. 3729–3747, 1997.

[3] R. D. Woods, "Screening of surface waves in soils," *Journal of the Soil Mechanics and Foundations Division*, vol. 94, no. 4, pp. 951–979, 1968.

[4] D. D. Barkam, *Dynamics of Bases and Foundations*, McGraw-Hill, New York, NY, USA, 1962.

[5] R. K. Shrivastava and N. S. V. Kameswara Rao, "Response of soil media due to impulse loads and isolation using trenches," *Soil Dynamics and Earthquake Engineering*, vol. 22, no. 8, pp. 695–702, 2002.

[6] M. Adam and O. von Estorff, "Reduction of train-induced building vibrations by using open and filled trenches," *Computers and Structures*, vol. 83, no. 1, pp. 11–24, 2005.

[7] A. Karlström and A. Boström, "Efficiency of trenches along railways for trains moving at sub- or supersonic speeds," *Soil Dynamics and Earthquake Engineering*, vol. 27, no. 7, pp. 625–641, 2007.

[8] L. Andersen and S. R. K. Nielsen, "Reduction of ground vibration by means of barriers or soil improvement along a railway track," *Soil Dynamics and Earthquake Engineering*, vol. 25, no. 7–10, pp. 701–716, 2005.

[9] H. J. Dolling, "Die Abschirmung von Erschütterungen durch Bodenschlitze," *Bautechnik*, vol. 6, pp. 193–204, 1970.

[10] W. A. Haupt, "Model tests on screening of surface waves," in *Proceedings of the 10th International Conference on Soil Mechanics and Foundation Engineering*, vol. 3, pp. 215–222, Stockholm, Sweden, June 1981.

[11] D. E. Beskos, B. Dasgupta, and I. G. Vardoulakis, "Vibration isolation using open or filled trenches—part 1: 2-D homogeneous soil," *Computational Mechanics*, vol. 1, no. 1, pp. 43–63, 1986.

[12] B. Dasgupta, D. E. Beskos, and I. G. Vardoulakis, "Vibration isolation using open or filled trenches—part 2: 3-D homogenous soil," *Computational Mechanics*, vol. 6, pp. 129–142, 1990.

[13] S. Ahmad and T. M. Al-Hussaini, "Simplified design for vibration screening by open and in-filled trenches," *Journal of Geotechnical Engineering*, vol. 117, no. 1, pp. 67–88, 1991.

[14] T. M. Al-Hussaini and S. Ahmad, "Design of wave barriers for reduction of horizontal ground vibration," *Journal of Geotechnical Engineering*, vol. 117, no. 4, pp. 616–636, 1991.

[15] R. Klein, H. Antes, and D. Le Houédec, "Efficient 3D modelling of vibration isolation by open trenches," *Computers and Structures*, vol. 64, no. 1–4, pp. 809–817, 1997.

[16] H. Takemiya, K.-S. Shim, and K. Goda, "Embankment train track on soil stratum and wave impeding block (WIB) measured for vibrations reduction," in *Soil Dynamics and Earthquake Engineering VII*, C. A. Brebbia and A. S. Cakmak, Eds., vol. 14, pp. 105—112, Wessex Institute of Technology, Wessex, UK; Princeton University, Princeton, NJ, USA, 1995.

[17] K. R. Massarsch, "Mitigation of traffic-induced ground vibration," in *Proceedings of the 11th International Conference on Soil Dynamics and Earthquake Engineering*, Berkeley, Calif, USA, January 2004.

[18] G. Lanzo and F. Silvestri, *Risposta Sismica Locale. Teorie ed Esperienze*, Hevelius, 1999.

[19] L. Andersen and C. J. C. Jones, "Coupled boundary and finite element analysis of vibration from railway tunnels—a comparison of two- and three-dimensional models," *Journal of Sound and Vibration*, vol. 293, no. 3–5, pp. 611–625, 2006.

[20] C. M. Di Liberto and G. Di Mino, "I fenomeni vibrazionali generati dal transito dei vettori ferroviari: analisi FEM del comportamento meccanico del sistema sovrastruttura-terreno. Casi studio per configurazione in trincea," *Ingegneria Ferroviaria*, pp. 53–62, 2006.

[21] G. Di Mino, "Le vibrazioni in campo ferroviario: analisi F.E.M. dell'interazione convoglio-sovrastruttura-terreno," in *Proceedings of the 13th Convegno Nazionale SIIV*, Padova, Italy, October 2003.

[22] C. J. C. Jones and J. R. Block, "Prediction of ground vibration from freight trains," *Journal of Sound and Vibration*, vol. 193, no. 1, pp. 205–213, 1996.

[23] V. Aiello and F. Silvestri, "Vibrazioni prodotte da infrastrutture di trasporto in ambiente urbano: una proposta metodologica applicata ad un caso studio," in *Proceedings of the 22nd Convegno Nazionale di Geotecnica*, Palermo, Italy, Sebtember 2004.

[24] L. Hall, "Simulations and analyses of train-induced ground vibrations in finite element models," *Soil Dynamics and Earthquake Engineering*, vol. 23, no. 5, pp. 403–413, 2003.

[25] M. H. El Naggar and A. G. Chehab, "Vibration barriers for shock-producing equipment," *Canadian Geotechnical Journal*, vol. 42, no. 1, pp. 297–306, 2005.

[26] R. Courant, K. Friedrichs, and H. Lewy, "On the partial difference equations of mathematical physics," *IBM Journal*, vol. 11, pp. 215–234, 1967.

[27] A. Castellani, "Boundary conditions to simulate an infinite space," *Meccanica*, vol. 9, no. 3, pp. 199–205, 1974.

[28] J. Lysmer and R. L. Kuhlemeyer, "Finite dynamic model for infinite media," *Journal of the Engineering Mechanics Division*, vol. 95, pp. 859–875, 1969.

[29] G. Di Mino, C. M. Di Liberto, and J. Nigrelli, "A FEM model of rail track-ground system to calculate the ground borne vibrations: a case of rail track with wooden sleepers and k-fastenings at Castelvetrano," in *Advanced Characterisation of Pavement and Soil Engineering Materials*, A. Loizos, T. Scarpas, and I. Al-Qadi, Eds., Taylor & Francis, London, UK, 2007.

[30] S. Haykin, *NN: A Comprehensive Foundation*, Macmillan, New York, NY, USA, 1994.

[31] J. C. Principe, N. R. Euliano, and C. W. Lefebvre, *Neural and Adaptive Systems: Fundamentals Through Simulations*, John Wiley & Sons, New York, NY, USA, 2000.

Hindawi Publishing Corporation
Advances in Acoustics and Vibration
Volume 2009, Article ID 317202, 17 pages
doi:10.1155/2009/317202

Research Article

Dynamic Stability of Cylindrical Shells under Moving Loads by Applying Advanced Controlling Techniques Part I—Using Periodic Stiffeners

Khaled M. Saadeldin Eldalil[1] and Amr M. S. Baz[2]

[1] *Department of Mechanical Engineering, Faculty of Engineering, Tanta University, Sperbay, Tanta, Egypt*
[2] *Department of Mechanical Engineering, University of Maryland, 2137 Eng. Bldg., College Park MD 20742, USA*

Correspondence should be addressed to Khaled M. Saadeldin Eldalil, eldalil01@msn.com

Received 2 April 2009; Accepted 12 July 2009

Recommended by Mohammad Tawfik

The load acting on a cylindrical shell, with added periodic stiffeners, under a transient pressure pulse propelling a pullet (gun case) has been experimentally studied. This study is based on two modes of velocities, the first is subcritical mode and the second is supercritical mode. The stiffeners are added to the gun tube of an experimental gun facility, of 14 mm bore diameter. The radial strains are measured by using high-frequency strain gage system in phase with a laser beam detection system. Time-resolved strain measurement of the wall response is obtained and both precursor and transverse hoop strains have been resolved. The time domain analysis has been done using "wavelet transform package" in order to determine the frequency domain modes of vibrations and detect the critical frequency mode. A complete comparison of the dynamic behavior of the shell tube before and after adding periodic stiffeners has been done, which indicated that a significant damping effect reaches values between 61.5 and 38% for subcritical and critical modes. The critical frequency of the stiffened shell is increased, so the supercritical mode is changed to subcritical mode. The amplification and dispersion factors are determined and constructed; there is a reduction in the corresponding speed frequencies by about 10%. Also the radial-bending vibrations and tube muzzle motions are detected at muzzle velocity ratio of 0.99%, the results indicated that there is a significant improvement in increasing the number of rounds per second by about 36% and increasing the pointing precision by about 47%.

1. Introduction

The analysis of moving loads on elastic structures has drawn the attention of many researchers over the last century. The extent of the efforts dedicated to studying this problem is justified by the wide variety of structures which are subjected to moving loads, such as bridges, gun barrels, rails, work pieces during machining operations, as well as fluid-conveying pipes. In all these structures, the emphasis is placed on studying two basic phenomena. The first phenomenon deals with the amplification of the dynamic deflections caused by the moving loads, as compared with the deflections resulting from the static application of the same loads. The second considered phenomenon is associated with the dynamic instabilities that can be generated when the velocity of the moving loads exceeds certain critical values.

Vibration of gun barrels is one of the most affected because it leads to dispersion of shot patterns. Decreasing dispersion will lead to a more lethal (more likely to hit), survivable (the sooner the enemy is hit the less likely they are to hit you), and sustainable (less rounds need to achieve the desired effect) weapon system. An intuitive way to reduce dispersion is to reduce the vibrations of the barrel. The end of the barrel is the antinode for all vibration modes, so increased exit velocity requirements have led to a demand for longer barrels. Longer barrels are more susceptible to these vibrations, Fryba [1].

Recently, the demand of increasing muzzle velocity arises strongly for defending considerations, so increasing shell length is becoming essential to satisfy the main target together with increasing stability and decreasing weapon mass. These challenging counteractions lead many

investigators to propose theoretical and experimental solutions. The dynamic behavior of cylindrical shells was studied experimentally by Finlayson [2], Simkins [3, 4], Beltman et al. [5], Thomas [6], and Baz et al. [7], the results indicated that increasing bullet velocity by expanding pressure step causing the axisymmetric radial vibration to be several times higher than that produced by the static application of the same load. So, the traveling velocity of the moving load affects the amplitude of the radial response and critical velocity, above which the shell response becomes unstable.

Many authors have been involved with the theoretical determination of the dynamic response of structures subjected to moving loads, Abu-Hilal and Mohsen [8], and Lin and Trethewey [9]. Several theoretical techniques have been considered in order to define the stability limits and conditions for different structures, Nelson and Conover [10], Steele [11, 12], and Bolotin [13].

Ruzzene and Baz [14, 15] studied theoretically the vibrations of cylindrical shells induced by a moving projectile propelled by an internal pressure wave and controlled by placing stiffening rings periodically along the length of the shell. They suggested that the shell response is, therefore, given by the combination of rotationally symmetric and bending motions, which are coupled by the interaction between the moving projectile, the internal pressure, and the shell vibrations. They developed a finite-element model to predict the transient response of stiffened cylindrical shells loaded by a moving projectile propelled by an internal pressure wave. The model is formulated to account for the interaction between moving mass, internal pressure, and shell vibration and to capture the resulting coupling between bending and rotationally symmetric response. Their results demonstrate the capability of periodically stiffened shells of reducing bending vibrations and, therefore, of stabilizing the overall shell response, before and after the projectile leaves the shell. Aldraihem and Baz [16, 17] investigated theoretically the dynamic stability and response of stepped tubes subjected to a stream of moving objects excitations. They found that the stability of certain tube modes can be improved by providing the tube with appropriately spaced steps.

It is obvious that the increased susceptibility of long gun tubes to operation-induced vibration affects precision and accuracy of firing as well as barrel/round interactions during firing. A lightweight, low-cost method is desired to damp firing induced vibrations thereby increasing performance of the gun system. A relatively inexpensive and lightweight method of damping vibrations in some structures is to apply a surface treatment of a stiffening material. The stiffeners are clamped to the base material of the gun tube, in our case. Radial and transverse vibrations in the system result in radial and shear deformation of the stiffening material, which in turn redistribute and dissipate the energy. The presented experimental work provides guidelines and clear vision for the design of gun barrels with increased firing velocity, improved accuracy, and enhanced structural stability.

To the best of our knowledge, investigating the gun tube with added stiffeners as a periodic damped structure has not been investigated experimentally.

This work deals with studying the gun tube with added stiffeners along its length under moving pressure pulse and mass. The length of the shell is about 130 times the caliber (about three times the present practical ratio) and it may increase to double this ratio to account for supercritical dynamics. A gun test facility is constructed, in the "Noise and control laboratory" at the University of Maryland, USA, to account for investigating and measuring the gun dynamics at subcritical and supercritical velocity modes. A complete comparison of the plain and stepped tube is presented. The dispersion and amplification curves are constructed. The configuration of the stepped shell which is chosen herein is quite similar to that of reference [14].

2. Experimental Setup

2.1. Pneumatic 6/12-Feet Gun Tube Facility

2.1.1. Setup Main Components. The experiment was carried out with in-door helium gun in the vibration and noise control laboratory at University of Maryland, it has a stainless steel tube length of 6 feet, and can be extended to the similar length in the case of running supercritical bullet velocities, as discussed in details by Baz et. al. [7]. Figure 1 shows schematic diagram of the gun system components and Figure 2 shows a view picture of the test setup facility.

As shown in Figure 1, the gun facility is composed of four main parts as follows.

Part 1: pullet decelerator (1),

Part 2: stainless steel tube assembly (2, 14),

Part 3: pneumatic gun machinery (3, 4, 6, 7, 8, 9, 10, 11, 12, 13),

Part 4: firing control box (5).

All the four mentioned parts are assembled on the main base structure (15).

2.1.2. Shooting Mechanism. The bullets are installed in the magazine (3) in Figure 1 and the system power supply is turned on (115 v ac). When Turning "ON" the firing switch in the control box, the air will permit to feed the main and booster cylinders (11) and (6) by low air pressure (220 psi). This will make their push rods to proceed forward to release one bullet from the magazine end and move it to the front of the gun core (12). When the bullet attains this location, a pulse of high-pressure helium will applied on the back of it, then it starts to move through the accelerator (13) which has sloped inlet bore and smaller diameter than the bullet at the rest of it, as shown in Figures 3(a) and 3(b). Due to this diameter difference, the bullet will be extruded and the helium pressure starts to grow up to almost near its maximum value. At this moment, the pressure forces will release the bullet by very high acceleration value. The

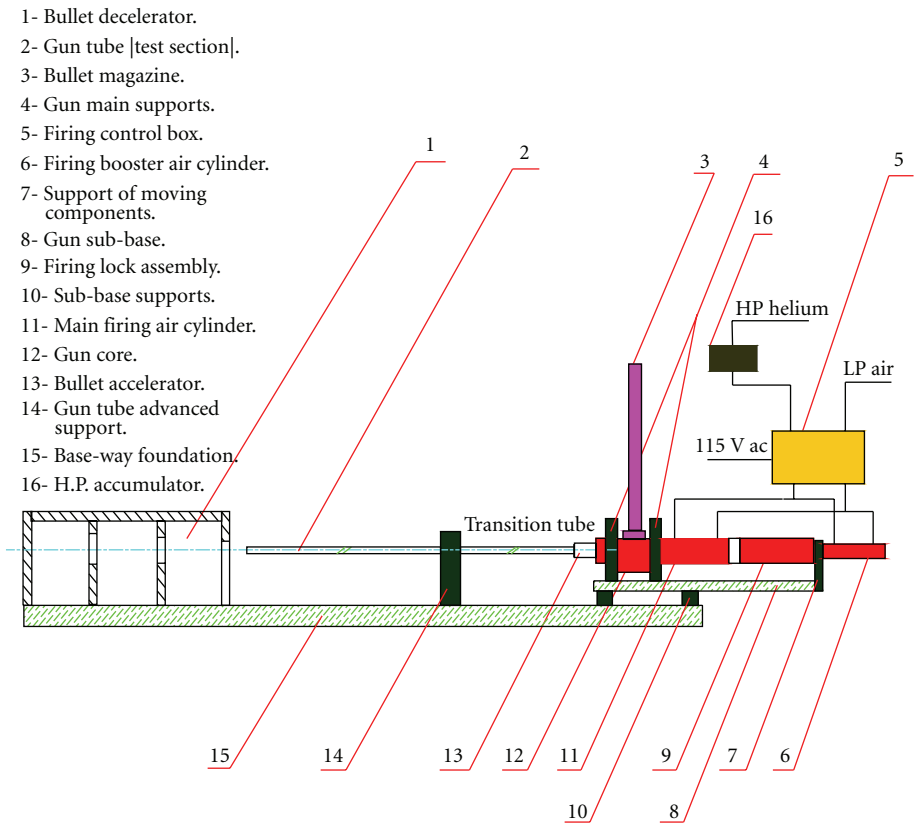

Figure 1: Experimental layout.

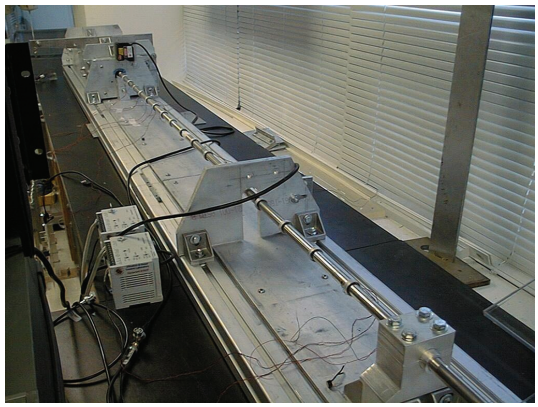

Figure 2: Setup view picture.

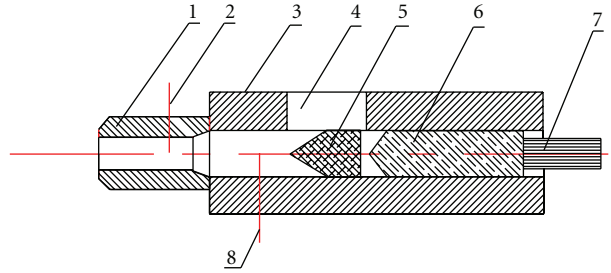

(a) The bullet comes inside gun core

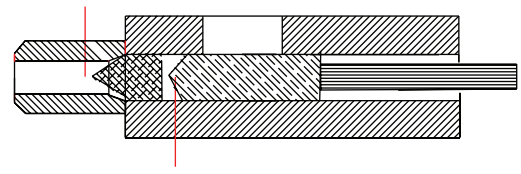

(b) The piston moves the bullet forward

Figure 3: Scheme of shooting mechanism.

high-pressure accumulator is used to keep the pressure pulse almost constant during the firing operation until the bullet leaves the muzzle.

After the bullet comes out from the gun tube, the feeding air of the cylinders will reverse and the piston rods will move back to their original positions. When the firing switch is on single shooting position, the piston will stay at its original location but if the firing switch is on automatic position, the shooting cycle will be repeated until the magazine will get empty. The kinetic energy of the bullet will be absorbed in the decelerator box (1). It partitioned to several rooms containing layers of foam sheets and its walls are made from hard aluminum of 0.5″ thickness.

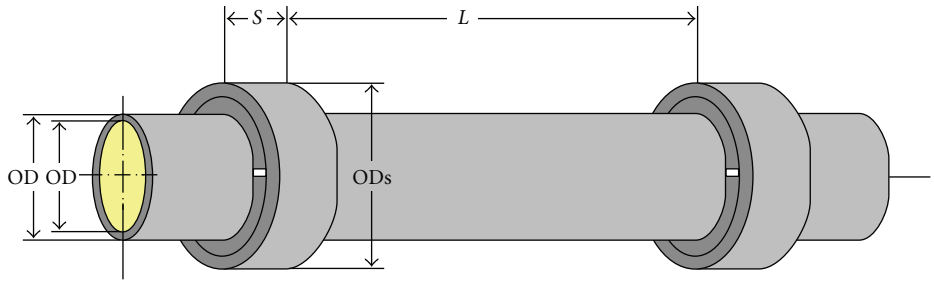

Figure 4: Tube-stiffeners configuration.

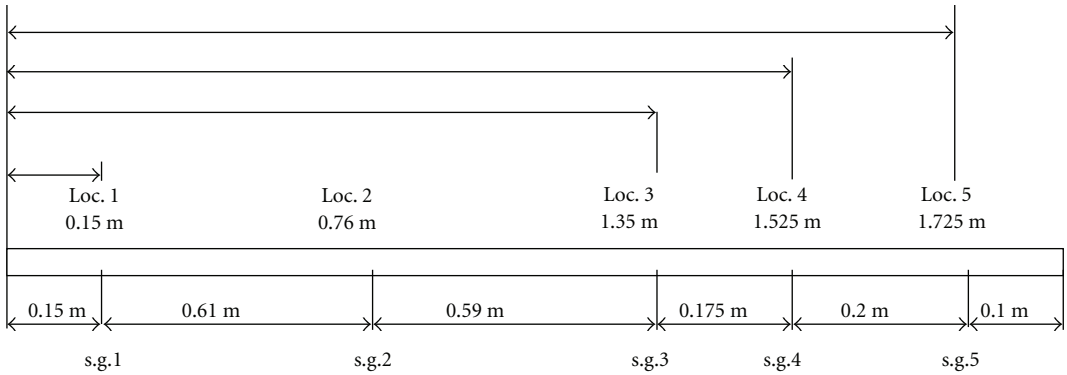

Figure 5: Measuring point locations on the plain and stepped gun tube for subcritical velocities.

2.1.3. Experimental Measurements. The gun tube is made from stainless steel; it has inner and outside diameters of 14.097 and 15.113 mms. The tube has a length of 1830 mms (130 times the caliber); it may be fixed directly on the bullet accelerator outlet or to the end of transition tube (another 130 caliber) at the advanced support (14) as shown in Figure 1. The transition tube is used to extend the expansion process and get supercritical bullet velocities and it has the same length and inner diameter as the gun tube but the outside diameter is bigger. The gun tube is supported as clamped-free to account for bending vibration response and as clamped-simple for radial vibration response measurements.

Five Micro Measurements strain gages of type "CEA-09-062UW-350" and signal conditioning amplifier were used to record the transition response of the gun tube. The strain gages were located at 150 (number 1), 760 (number 2), 1350 (number 3), 1525 (number 4), and 1725 (number 5) mms from the tube inlet, as shown in Figure 5. When extending the gun tube for supercritical measurements, we use only three strain gages locations, they are numbers 1, 4, and 5, as shown in Figure 19. The strain gages were mounted to measure the circumferential strains on the gun tube surface, so it adhered in a perpendicular direction to the tube axis.

The average steady-state deformation strain and the position of the bullet are measured by hand-made piezoelectric foil transducers of type PVDF film, adhered on the gun tube outside surface, and located at the same location plane of the strain gages but at orientation angle of 90°. The ac. signals are rectified by using full wave rectifier and displayed directly without any modulations. The average velocity of the bullet is obtained by measuring the strain gage signals and at the point just ahead of it (e.g., 1 and 2, then 2 and 3, etc.), the time difference between two consecutive points is measured and the distance is known, so, the average velocity is estimated. Also in order to confirm these results by additional measurements, a laser beam analog sensor is located at the outlet of the gun tube.

2.1.4. Experimental Procedure. The experiment was first done for gun tube free from stiffeners (plain tube) and a basic reference is completed and confirmed by many trails at the same conditions (pressure, bullet size, and weight). The experiments were done when the gun tube is evacuated at short and double tube length, in order to obtain low (subcritical) and high (supercritical) bullet velocities.

2.1.5. Controlling Stiffeners. The control stiffeners are used to redistribute and dissipate the energy of the structure. Its optimum number and size is chosen similar to that theoretically studied in [14]. The size of the stiffener is $S = 3.175$ mms long, outside and inside diameters (OD and ID) are 20.828 and 15.113 mms. The stiffener is composed from two part, outer ring and inner two half rings. The numbers of stiffeners were found to be 17 and the distance apart is $L = 100$ mms. The weight of the total stiffeners (the mass added to the gun tube) is found to be 23.32 g, about 5.6% of the tube weight. Figure 4 shows the shell stiffeners configuration.

2.1.6. Critical Parameters Prediction. The projectile critical velocity may be estimated by the followin expresion [18]:

$$V_{\text{cr}} = \sqrt{\frac{Eh}{\rho R}}\left[\frac{1}{3(1-\nu^2)}\right]^{0.25}, \quad (1)$$

where E: Young's modulus of elasticity of the tube; H: tube wall thickness; ρ: denesity of the tube material; R: tube average radius; ν Poisson's ratio of the tube material.

The critical radial frequency for infinite length for thin shells of thickness to radius ratio is less than 1/30 may be estimated with reasonable accuracy according to the findings of Baron and Bleich [19, 20] and Tang [21]:

$$\omega_{\text{cr}} = \frac{K}{a}\sqrt{\frac{Gh}{m}}, \quad (2)$$

where G: shear modulus $= E/2(1+\nu)$, N/m^2; m: mass of shell per unit of area $= \rho h$, kg/m^2; K: factor, $= \pi a/L$ in case of fundamental frequency $n = 0$, L: half wave length, m; a: tube mean diameter, m, then

$$\omega_{\text{cr}} = \frac{K}{a}\sqrt{\frac{E}{2.6\rho}}\ \text{rad/s}. \quad (3)$$

The estimated critical frequency will be 11462.5 Hz, also the value of the critical radial frequency is the same as estimated by [18].

3. Experimental Results and Analysis

3.1. Subcritical Case. The measurements were taken at five locations on the gun tube of length 1.825 m (130 calipers), as shown in Figure 5, for plain and with 17 single stiffeners.

3.1.1. Plain Tube Measurements. Samples of the time domain measurements of plain tube at location points that are specified before are shown in Figures 6(a), 6(b), and 6(c).

As stated in [7], the projectile velocity at location number 1 is very low (about 85 m/s) and the pressure puls is at its maximum value of 1600 psi. The resulting vibration is due to the detonation effect (sudden pressure rise) of the compressed helium at the intry of the accelerator chamber. The obtained vibration is considered as a radial circumference flextural mode (6.8 kHz), Blevins [18]. At location number 2, the velocity is increased to 515 m/s and the pressure value starts to become almost constant due to controlling the rate of injected Helium to be balanced with its expansion rate.

At location number 3, the velocity is increased to 810 m/s, and became about 80% from the theoretically calculated critical velocity (1045 m/s) so the radial vibration frequency increased and the radial deformations started to grow up. The amplification (ε) factor (normalized amplitude) became more than unity and its value can be calculated by

$$\varepsilon = \max \cdot \text{strain/Lame deformation}. \quad (4)$$

At location number 4, the projectile velocity reaches 917 m/s, that is, 88% and the head frequency is increased to 92 kHz and trailing wave became about 120 kHz. As the projectile proceeds toward the tube muzzel, the velocity increases to 980 m/s at location number 5 and the head wave frequency is found to be 80 kHz and the trailing wave reached to 145 kHz. These variations in the wave frequency, which decrease the

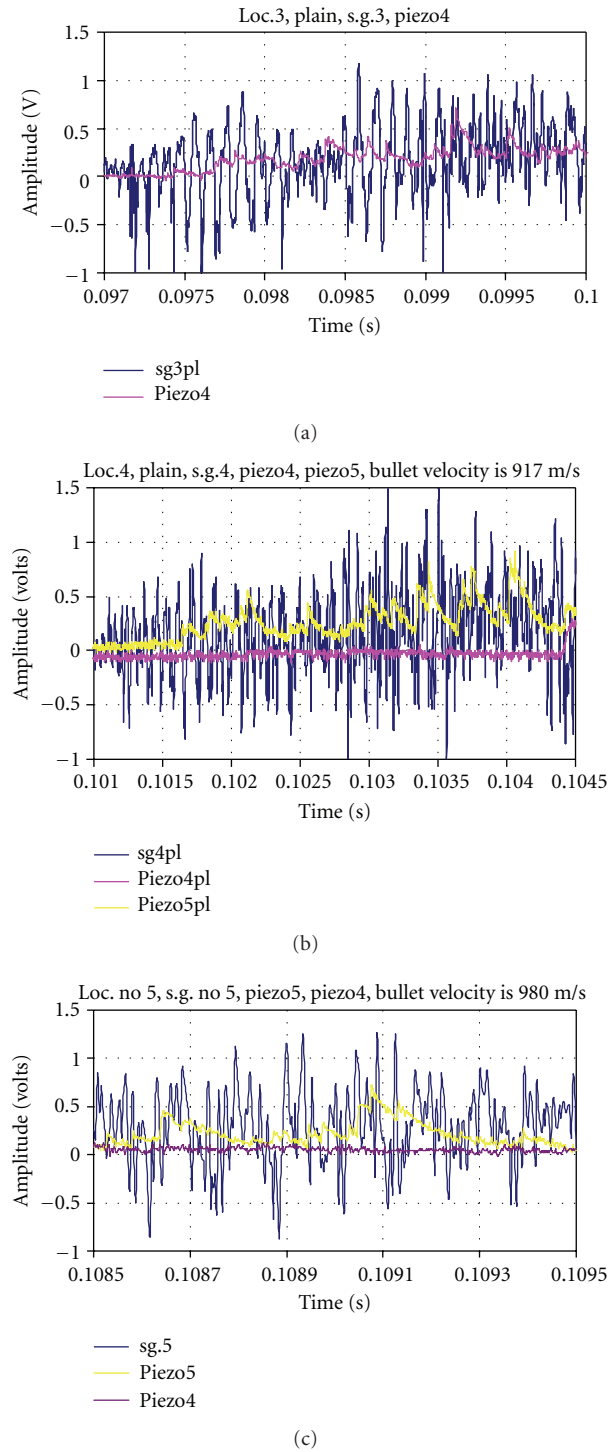

Figure 6: (a) Time domain output at location number 3. (b) Time domain output at location number 4. (c) Time domain output at location number 5.

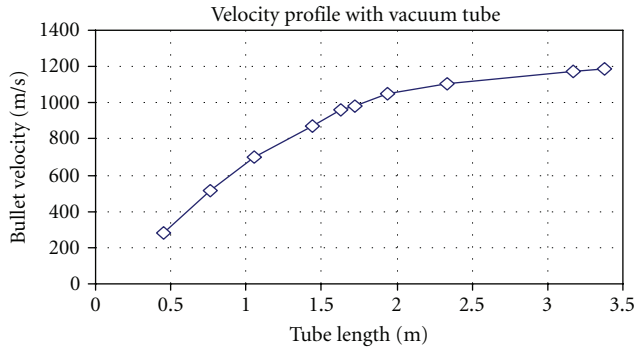

Figure 7: Bullet velocity profile with vacuum for tube length of 260 calibers at pressure pulse of 1600 psi.

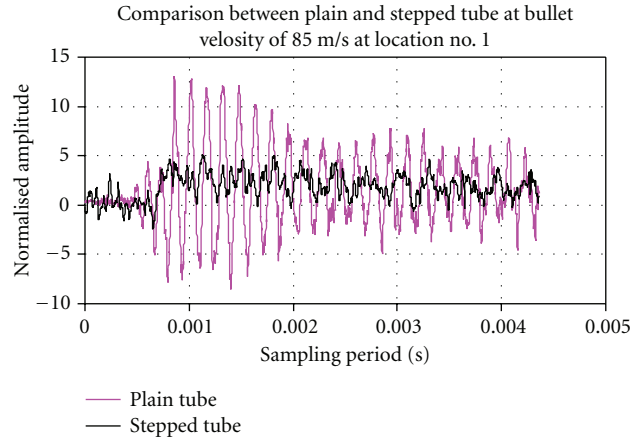

Figure 8: Comparison time domain measurements at location number 1.

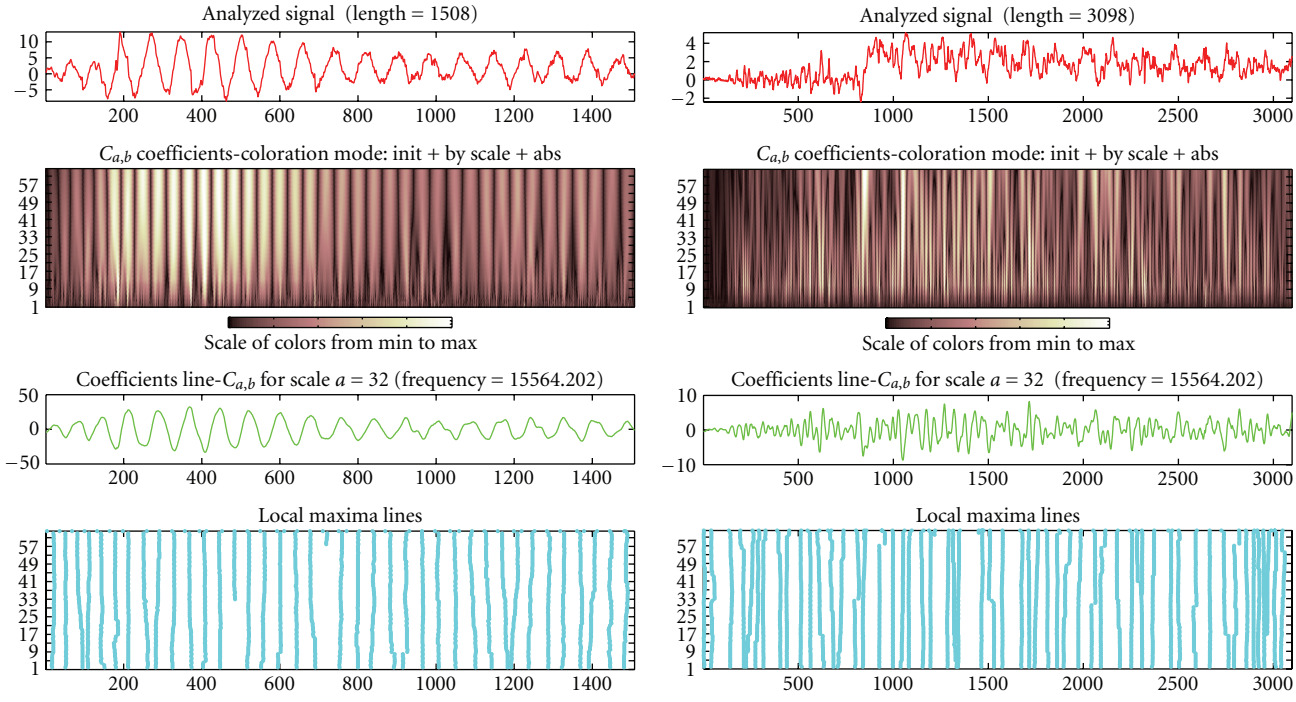

(a) Plain tube (b) Stepped tube

Figure 9: Time-frequency representation at location number 1.

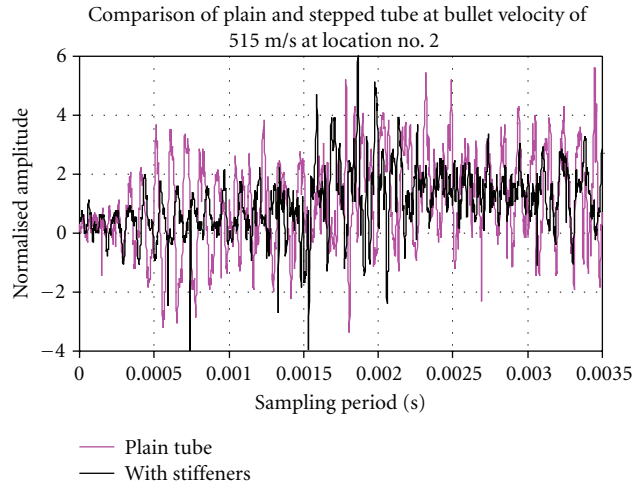

FIGURE 10: Comparison of time domain measurements at location number 2.

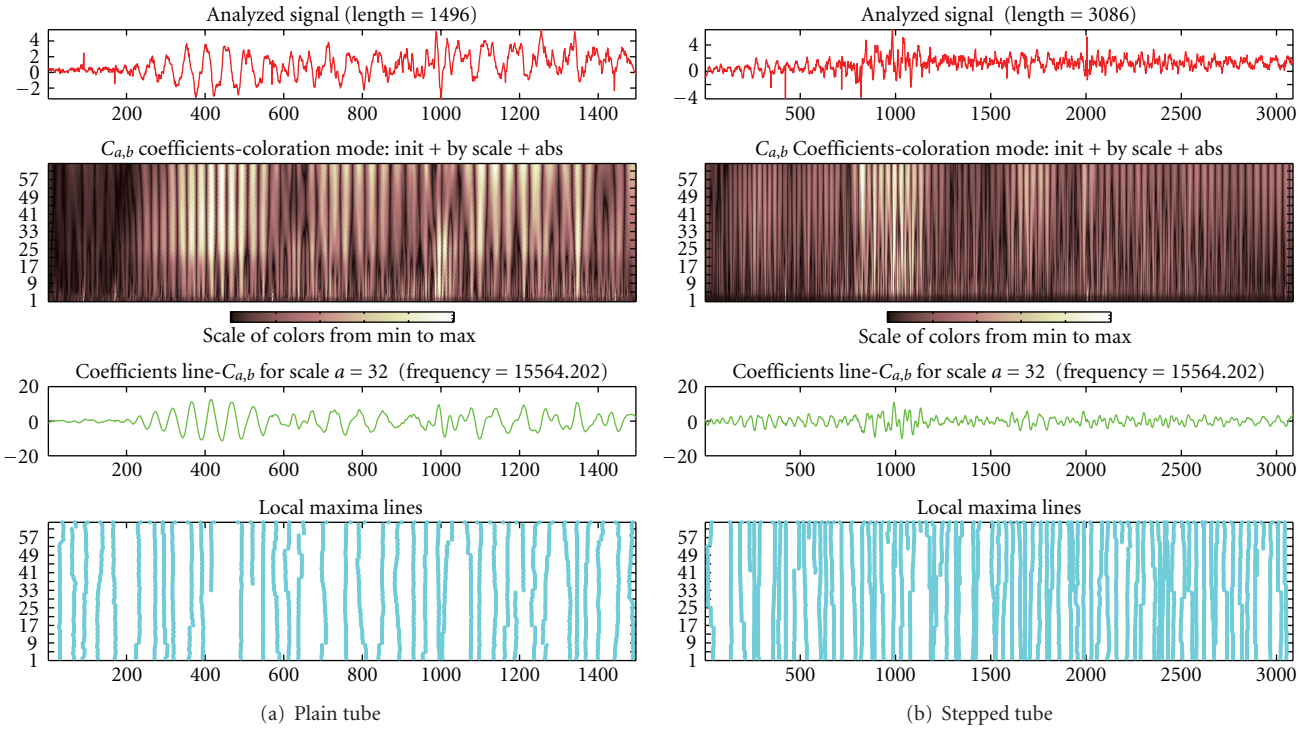

(a) Plain tube (b) Stepped tube

FIGURE 11: Time-frequency representation at location number 2.

head wave and increase the trailing wave, extrapolate that the critical velocity may be happening. The projectile leave the tube muzzle at a velocity of about 1015 m/s, that is, 97% of the critical velocity. So, some very large deformations occurred at the tube muzzel due to these transient transformation to the critical case. The velocity profile of the bullet inside a vacuum tube is shown in Figure 7. The avarage static deformation (Lame deformation) is found to be equal to the equevelant output strain voltage of 0.25 v.

3.1.2. Shell with Added Stiffeners Measurements. A comparison time domain measurements of the shell after adding stiffeners to its surface at the same location points, which are specified before, are shown in Figures 8, 10, 12, 14, and 16. The amplitude is normalized according to the L'me deformation and the time is shifted to starts from zero.

The effect of adding stiffeners is found to be significant. At location number 1 (Figure 8), where the low frequencies are the most, the amplification is reduced by 61.5%. The

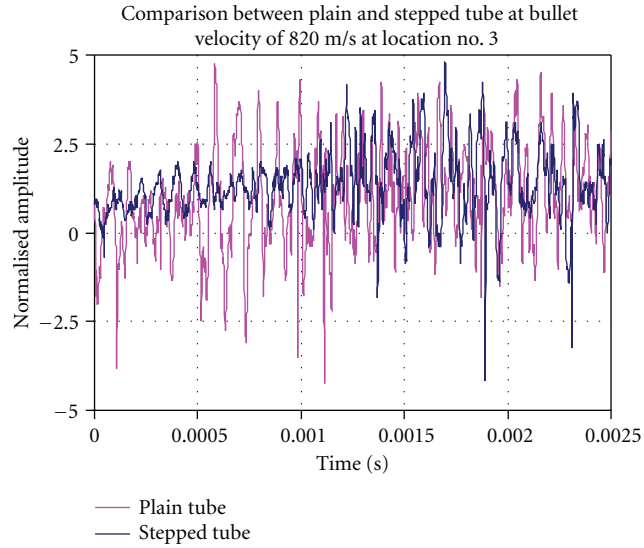

Figure 12: Comparison of time domain measurements at location number 3.

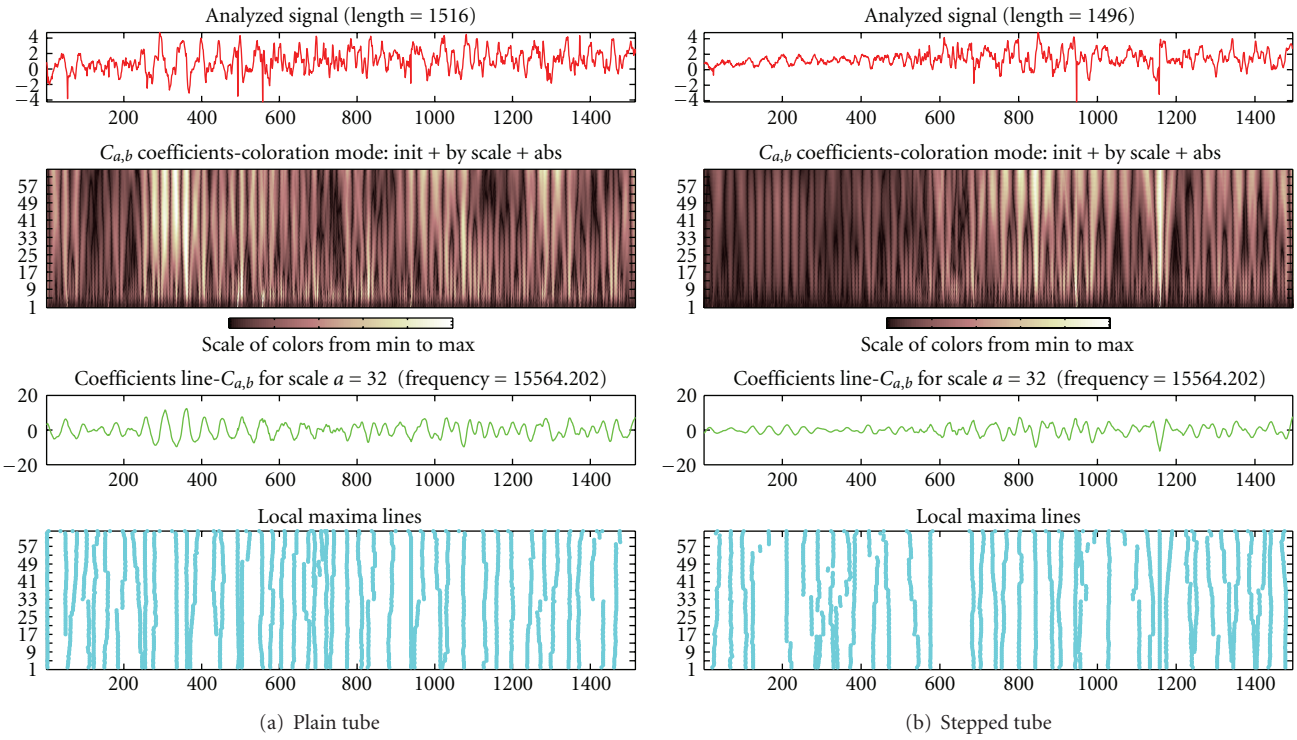

(a) Plain tube (b) Stepped tube

Figure 13: Time-frequency representation at location number 3.

shape of the strain signal is transferred to a classical subcritical signal shape. The same effect is continued at all the subsequent four locations; as shown in Figures 10, 12, 14, and 16. At locations numbers 2 and 3, the frequency starts to increase, so the total period of the signals is suppressed in shorter time. The stiffened tube amplification factor is decreased by 20% at locations numbers 3 and 4 and by 38% at location number 5.

The frequency analysis have been done using "wavelet transform (WT)" instead of "fast Fourier transform (FFT)" in order to detect the stronger high frequency modes which are built-in with the resulting vibrations. The ability of the wavelet transforms to detect very high frequencies is due to its very narrow scanning window (time span) which may be equal to the sampling period, so, it can deal well with the dynamic waves and the signal decomposition will be

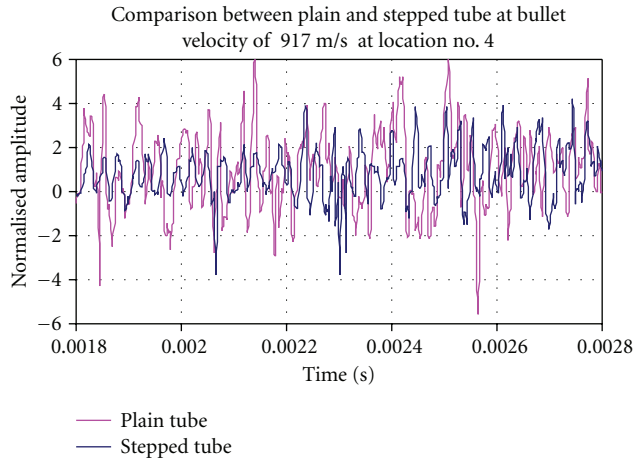

Figure 14: Comparison of time domain measurements at location number 4.

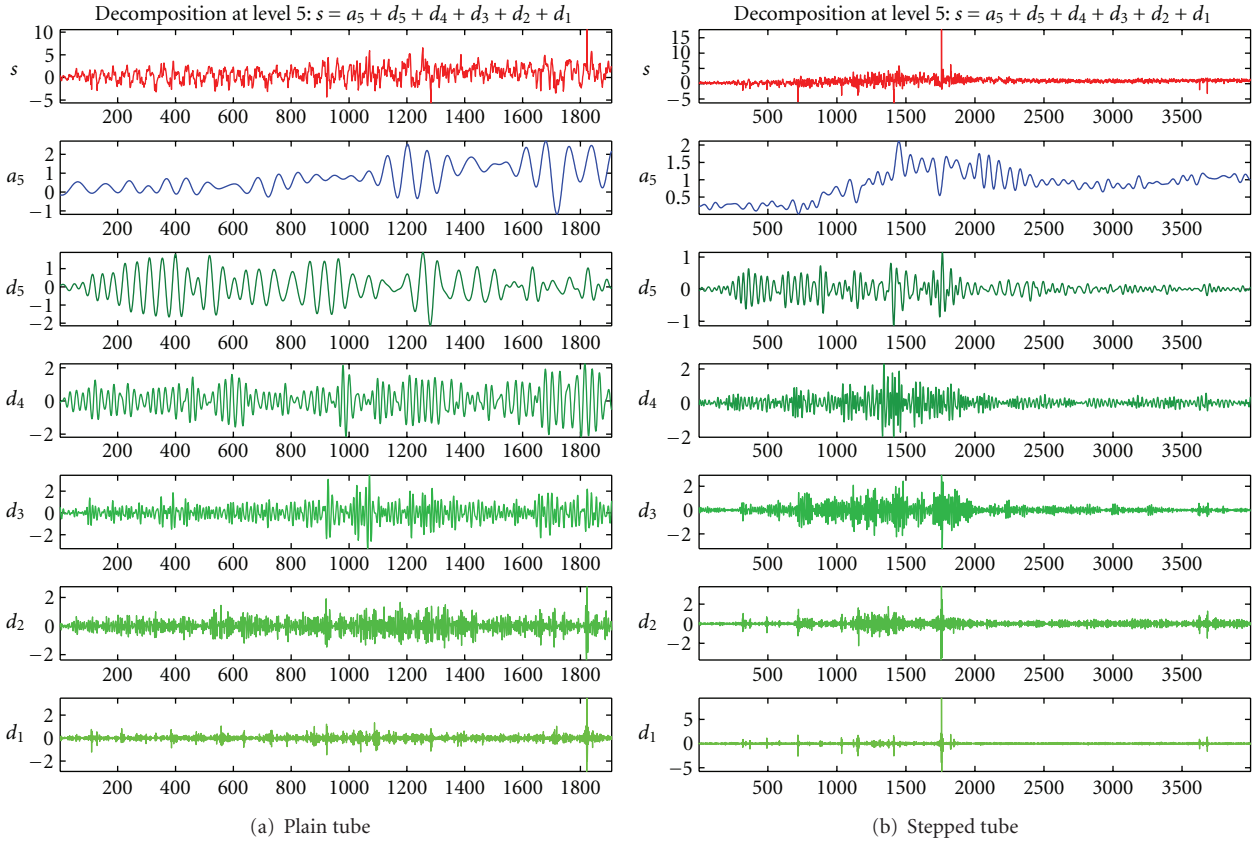

Figure 15: Time-frequency representation at location number 4.

obtained perfectly. Also the wavelet transform gives frequency modes corresponding to its time domain locations, so the interfering noise could be avoided which may be prevent any confused results.

Contrarily, the fast Fourier transform has a wide scanning window, so it detects only stationary signals which have limited frequency changes over long periods. Also, the frequency and time information of a signal at some certain point in the time-frequency plane cannot be known. In other words, we cannot know what spectral component exists at any given time instant, so the analysis will comprise trickery results.

A comparison of the time-frequency decomposition domains is illustrated in Figures 9, 11, and 13 at locations numbers 1, 2, and 3, respectively. The figures indicate that the frequency domain appears as a colorization area (pink color),

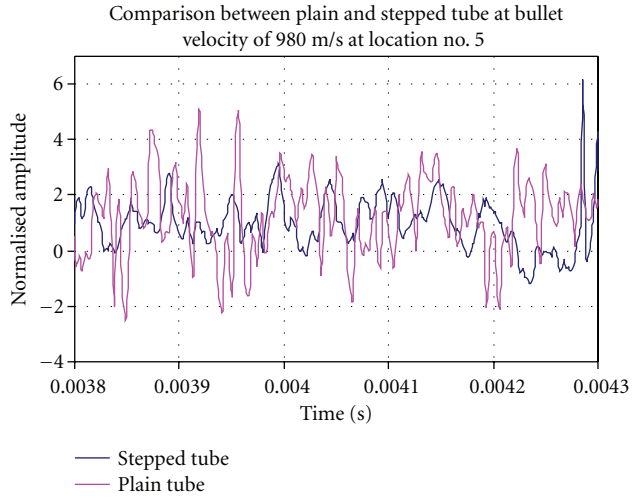

Figure 16: Comparison of time domain measurements at location number 5.

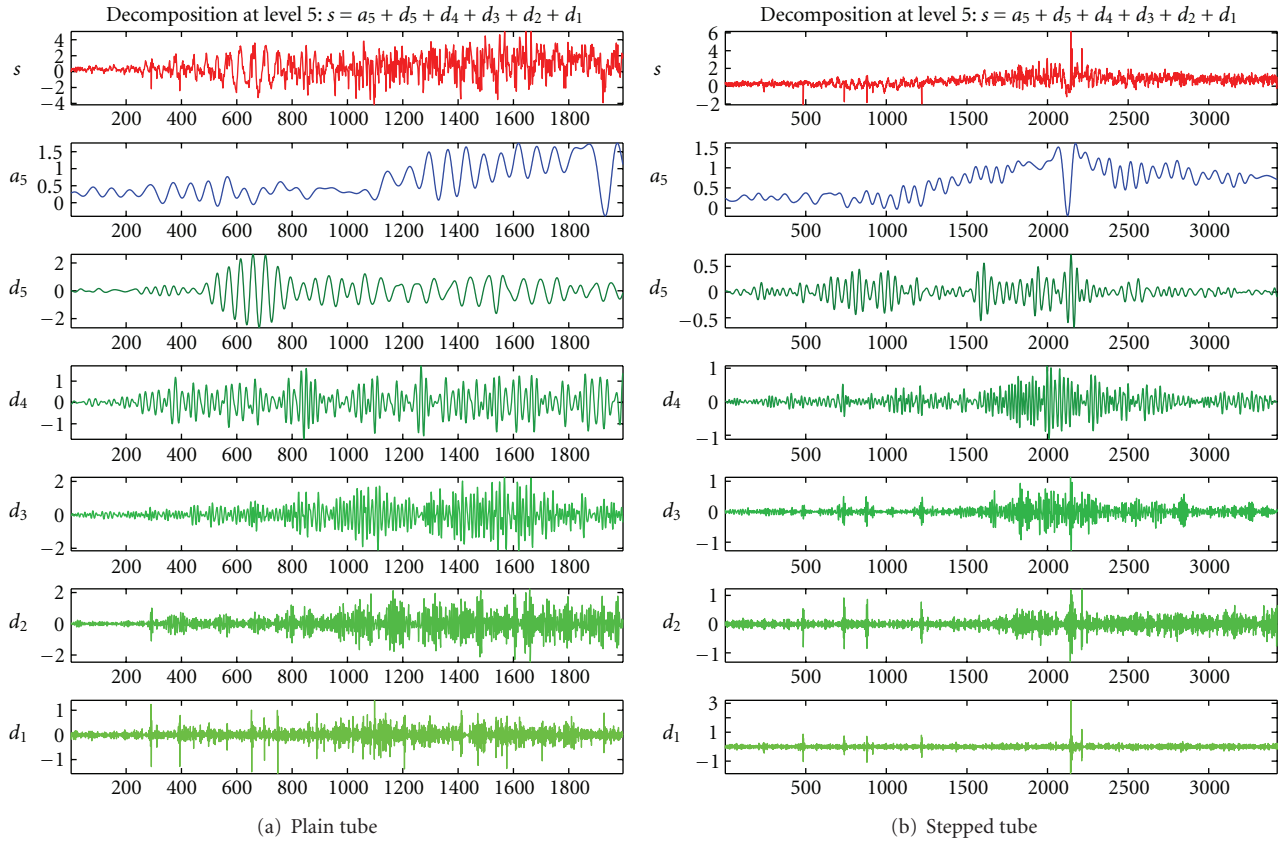

(a) Plain tube (b) Stepped tube

Figure 17: Time-frequency representation at location number 5.

it changes from dark to bright as the amplitude increases from minimum to maximum; also the frequency is defined by a so-called parameter "Scale" which is proportional to the inverse of the frequency multiplied by a certain factor depending on the used decomposition function of WT family. The figures indicate that the high frequency modes are suppressed due to using stiffeners; also they indicate that the frequency modes decomposition is carried out corresponding to its time domain location.

Figures 15 and 17 show the results of signal processing (decomposition) at locations (4 and 5) by using discrete wavelet transforms. The modes herein are called coefficients, a_1 represents the most very lower frequency mode. The higher frequency modes are represented by coefficients d_5 to

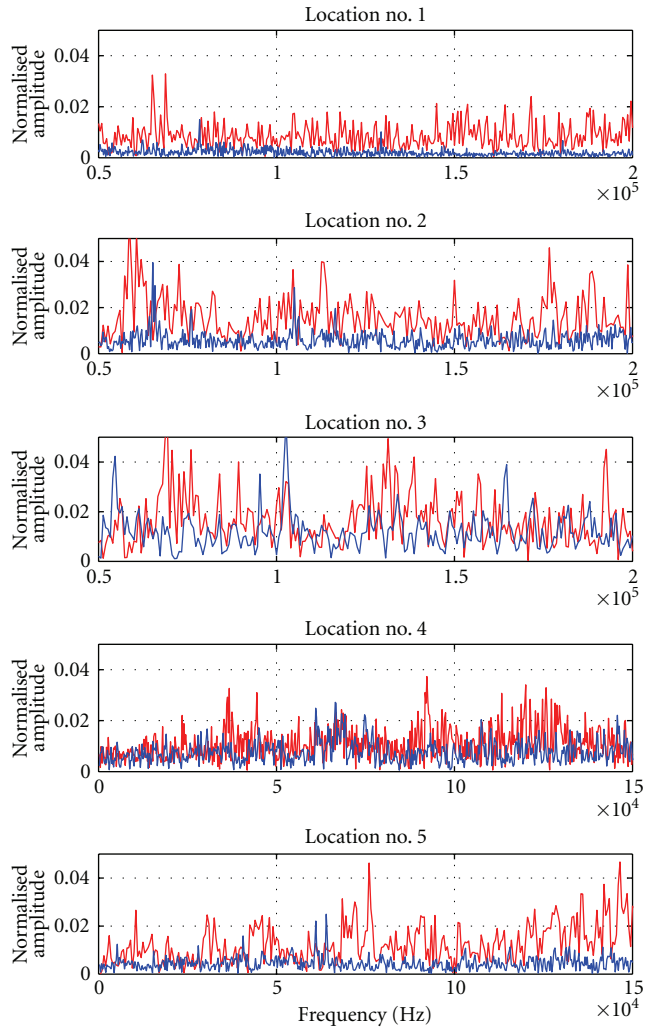

Figure 18: Frequency-domain analysis at locations 1, 2, 3, 4, and 5, red color for original and blue color for stepped tube.

d_1 (from low to high). It is obvious, from the figures, that there is higher amplitude frequencies for coefficients d_3, d_2, and d_1 in the case of plain tube, but these corresponding coefficients are suppressed to lower amplitude values in the case of stepped tube.

Figure 18 shows a comparison of the frequency domain analysis at the five mentioned tube locations before and after using stiffeners. The figure indicates that the absolute value of the signal amplitude is increased at locations numbers 4 and 5, where the critical and supercritical symptoms are started.

3.2. Supercritical Measurements. As mentioned earlier, the supercritical measurements are taken with the aid of extension tube, which is similar to the subcritical tube in length but it has double wall thickness. This double wall thickness tube has higher values of critical velocity and frequency, so, running the experiment will be safer and its damage will be avoided.

3.2.1. Plain Tube Measurements. The measurement locations are shown in Figure 19. Samples of the obtained supercritical measurements are shown in Figures 20(a) and 20(b) at locations numbers 6 and 8.

At location number 6, the velocity was found to be 1050 m/s, that is, about 100.5% above the critical velocity. The signal shape is resembles the classical super critical signal of [4]. At locations number 7, the signal amplitude is decreased but the velocity increased to 1176.5 m/s, then at location number 8, the velocity increased to 1190 m/s, about 113.9% of the critical velocity and the frequency amplitude continued in decreasing.

At location number 7, the detected frequency of the head wave is found to be 70 kHz, and the trailing wave is 155 kHz and at location number 8, the trailing wave frequency is found to be more than 200 kHz.

3.2.2. Shell with Added Stiffeners Measurements. A comparison of the time domain measurements of plain and stiffened tube are shown in Figures 21(a), 21(b), and 21(c). The amplification factor at location number 6 is decreased to a value of 25% of that obtained of the plain tube, and the signal shape is changed to be as a typical classical subcritical

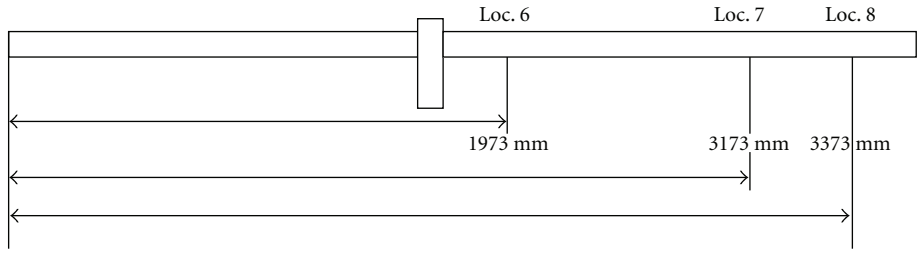

Figure 19: Supercritical measuring locations.

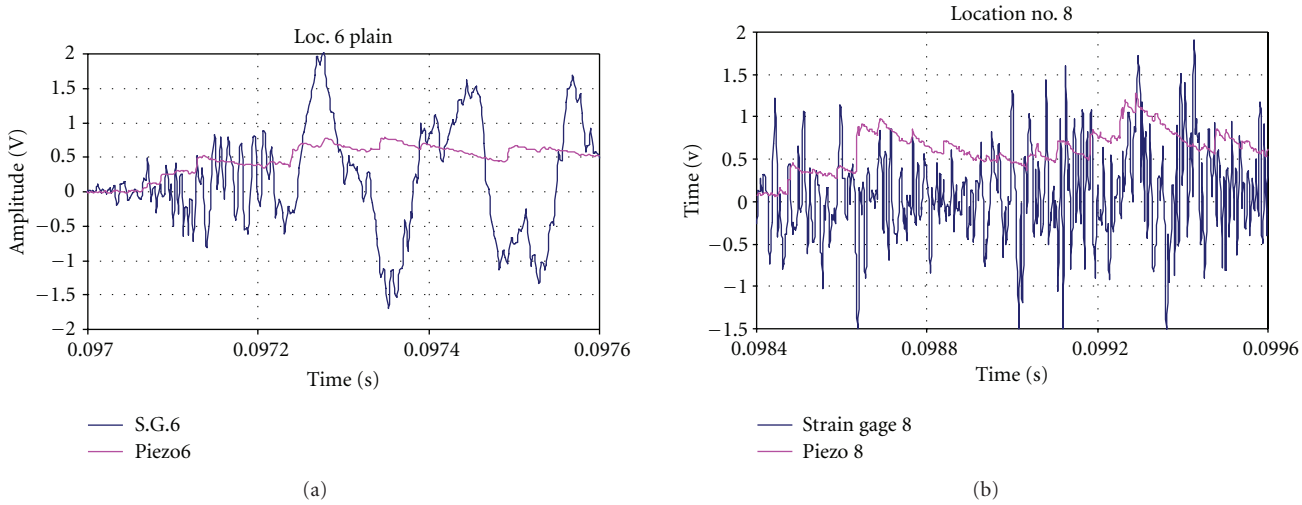

Figure 20: (a) The output signals at location 6, plain tube. (b) The output signals at location 8, plain tube.

shape, that is, the supercritical condition is transferred to subcritical case. At location number 7, the amplitude of the high frequency of the stiffened tube is increased by about 90% of that of the plain tube, this is due to increasing the bullet velocity and frequency. At location number 8, the amplification factor is increased to about 100% than that of the plain tube.

The signal decomposition diagrams at locations numbers 6, 7, and 8 are shown in Figures 22, 23, and 24. The figures show that the amplitude of vibrations at location number 6 of coefficients d_2 and d_1 are decreased due to using stiffeners, it is just aft-critical location. The component d_1 of the stiffened tube is reduced or almost vanished. The high-frequency mode amplitude d_2 of the stiffened tube at locations number 7 is started to increase together with the head wave frequency and continued increasing at location number 8 where it includes the vibration modes of d_2 and d_1.

The frequency domain analysis of the high-frequency modes for both plain and stiffened tube (d's coefficients), at the corresponding measurement locations, are shown in Figure 25. The figure indicates that the supercritical appearance at location number 6 is transformed into subcritical mode by using periodic stiffeners. Contrarily, the critical and supercritical symptoms are obviously started at locations numbers 7 and 8 of the stiffened tube.

The amplification factor diagram is shown in Figure 26, it is obvious that the stiffened tube frequencies are shifted to lower values than the plain tube by about 10%, and the critical velocity is increased to about 1190 m/s. The dispersion curve is constructed and shown in Figure 27, the figure indicates that the expected critical frequency is 114 kHz and the critical velocity is 1045 m/s for the case of plain tube, as obtained by [18–21]. The critical velocity and critical frequency is increased, in the case of using stiffeners to about 1190 m/s and 200 kHz, respectively. So, adding stiffeners to the plain tube leads to increasing the critical velocity and frequency.

3.3. Measurements of Radial-Bending Vibrations. The radial-bending vibrations of plain and stiffened tube are shown in Figures 28 and 29. The tube support is changed to clamped-free, while in the previous study, it was clamped-simple. It is obvious that the stability time which the tube walls taken to rebound is decreased in the case of stiffened tube from 140 ms to 90 ms, by a ratio of about 36%. So, this will lead to increasing the number of rounds from 7 to 11 rounds per second with good retargeting precision.

3.4. Measurements of Tube End Traverse Pointing Motion. The motion of the gun tube end is very important to satisfy

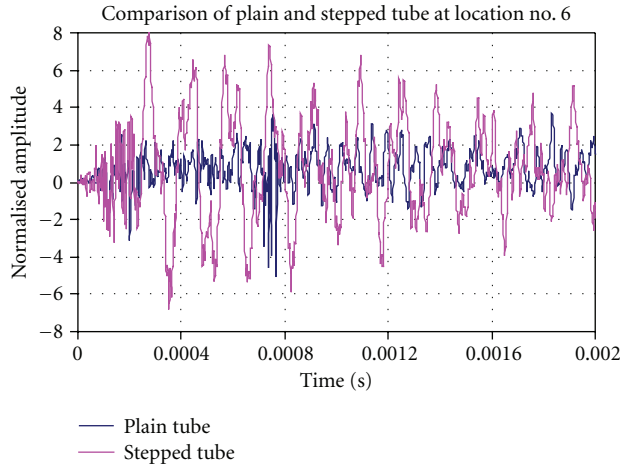

(a)

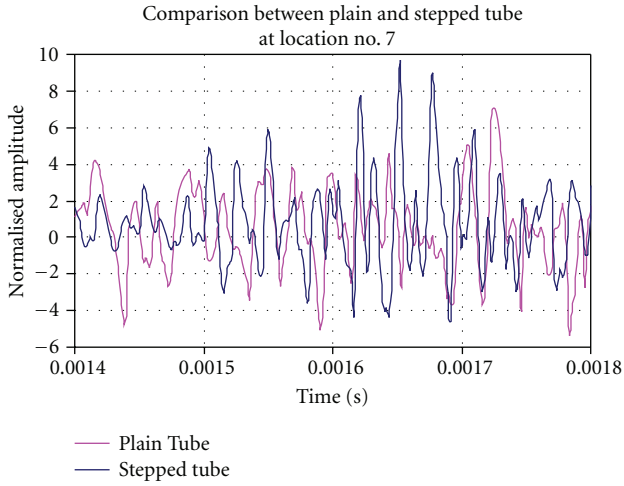

(b)

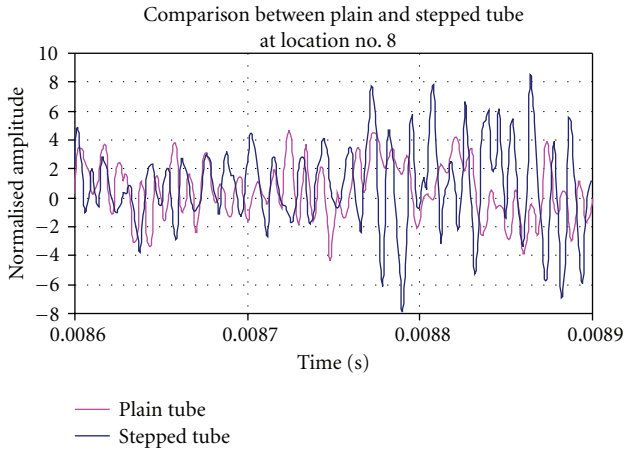

(c)

Figure 21: (a) Comparison of time domain measurements at location number 6. (b) Comparison time domain measurements at location number 7. (c) Comparison of time domain measurements at location number 8.

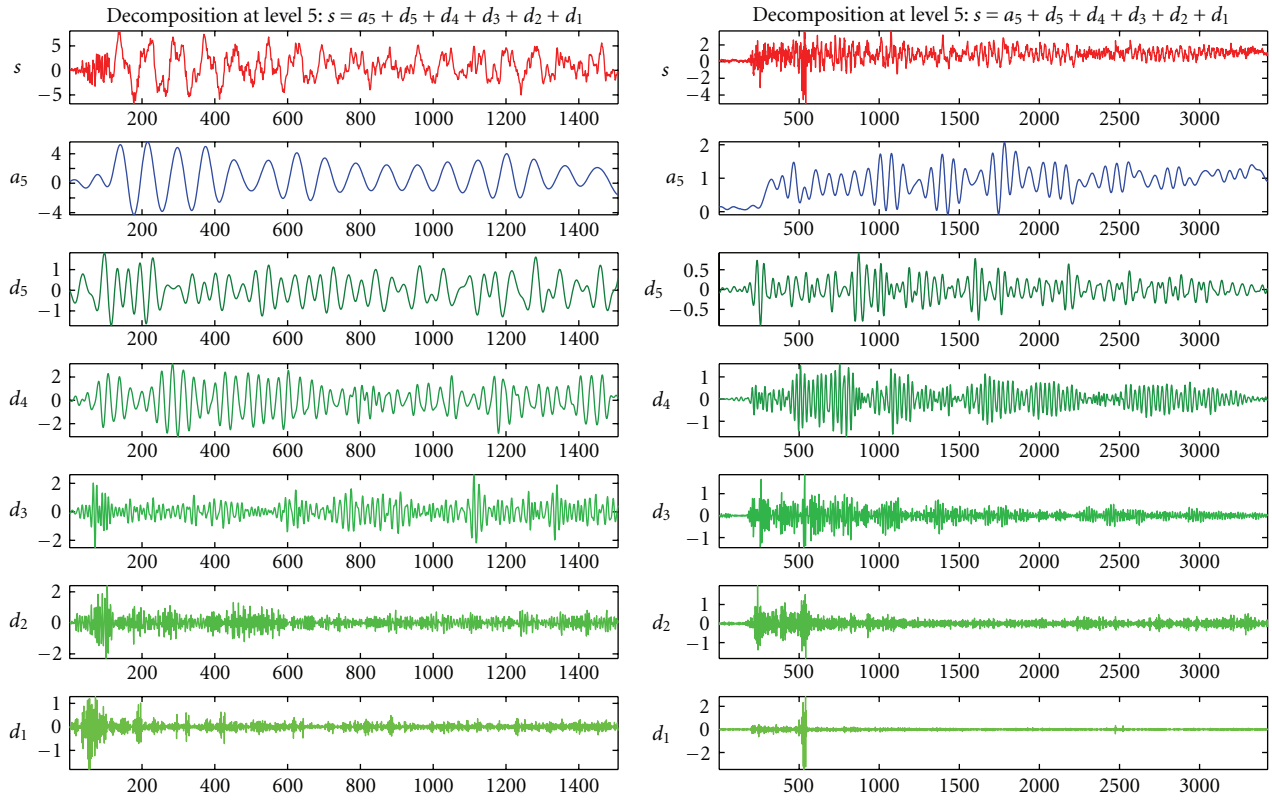

(a) Plain tube (b) Stepped tube

Figure 22: Strain signal decomposition at location number 6.

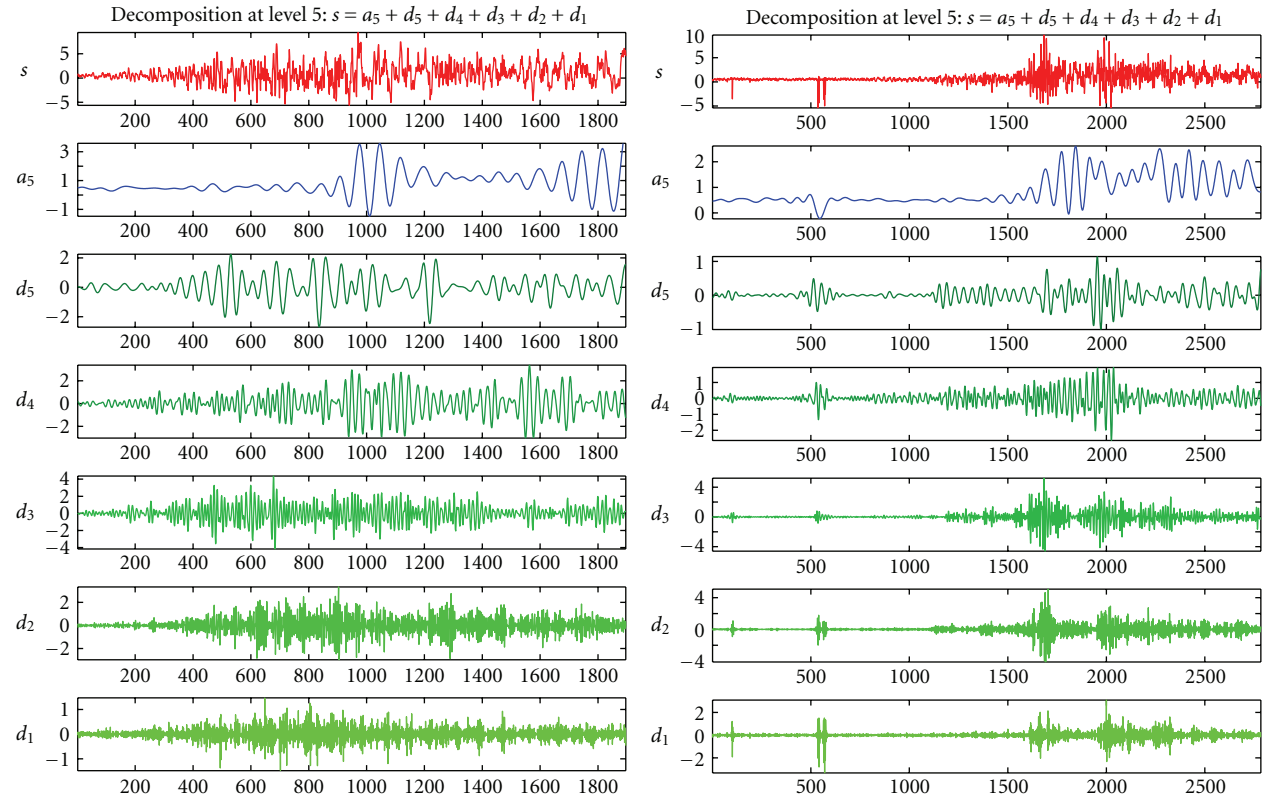

(a) Plain tube (b) Stepped tube

Figure 23: Strain signal decomposition at location number 7.

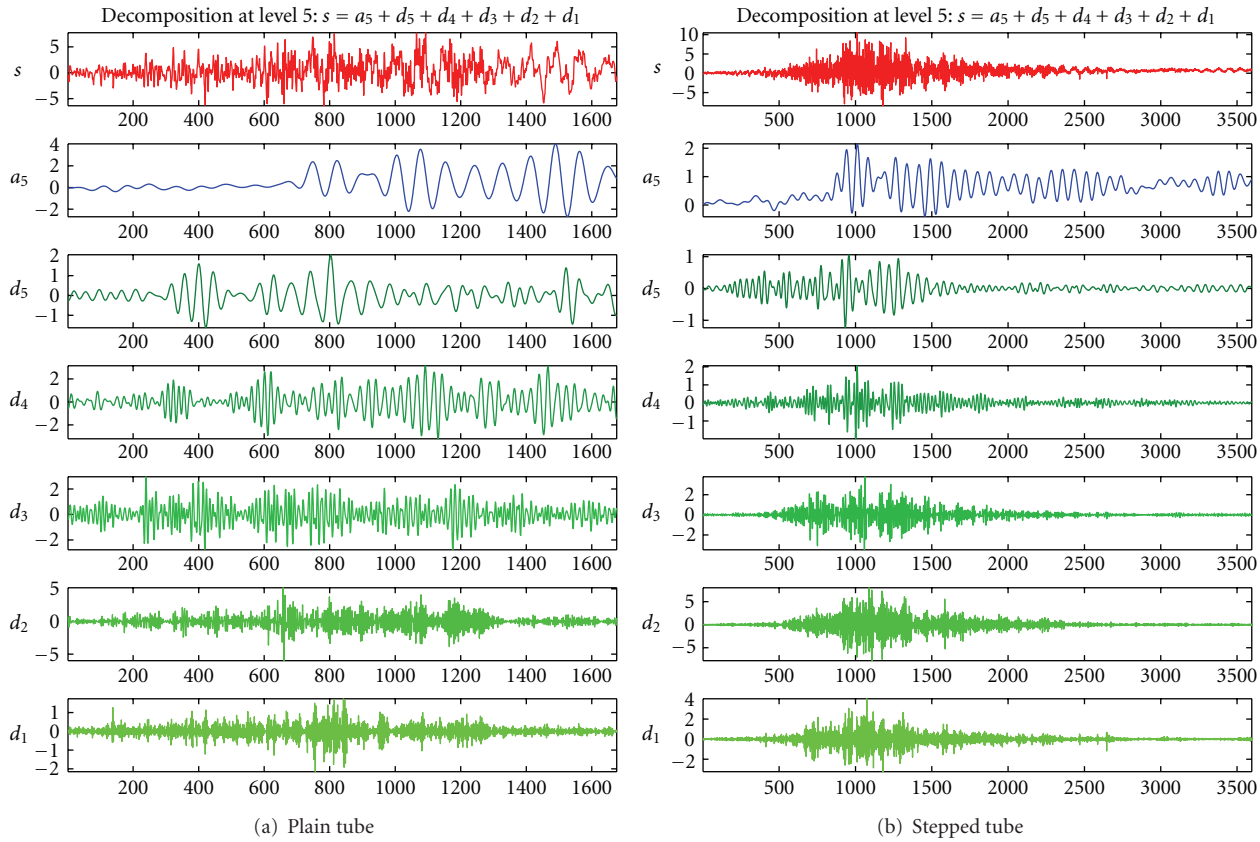

Figure 24: Strain signal decomposition at location number 8.

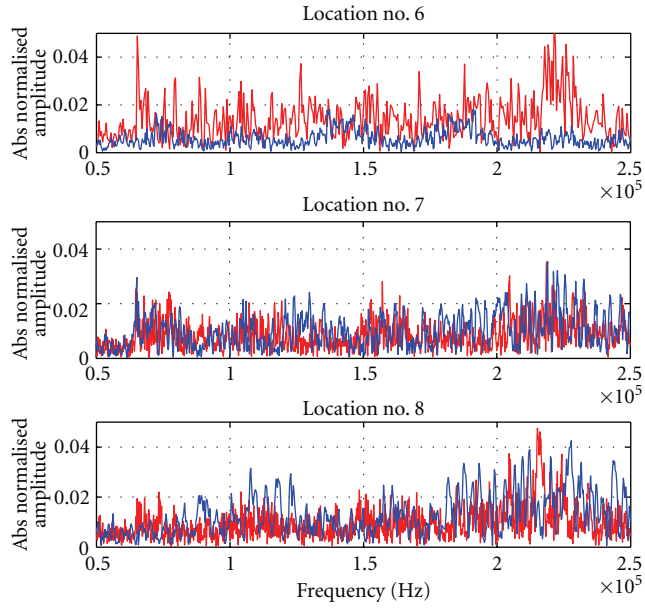

Figure 25: Frequency domain analysis at locations numbers 6, 7, and 8, red color for original and blue color for stepped tube.

high-accuracy pointing precision although it is considered as an antinode point. Figures 30(a) and 30(b) illustrate the bullet position in the shell versus the normalized displacement, for plain and stiffened tube. The figure shows that the shell response to the bullet is delayed until the bullet reaches about 50% of the shell tube length and the maximum deflection is reduced from 0.33 to 0.175 by a ratio of 47%.

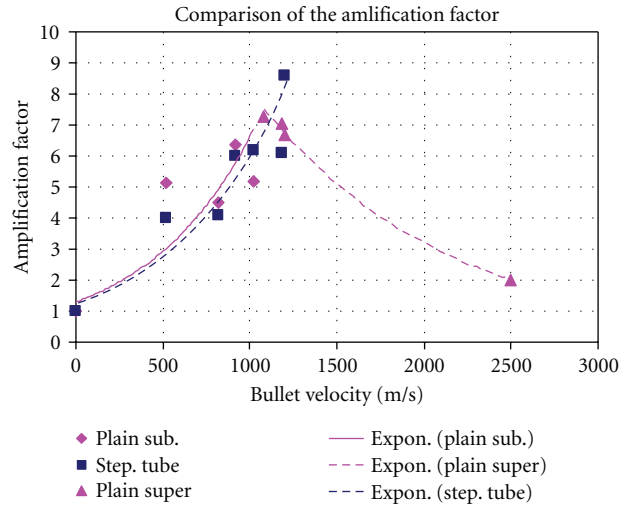

Figure 26: Amplification factor.

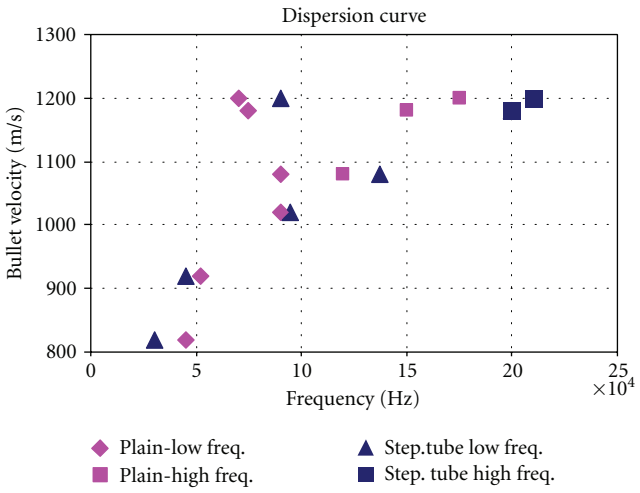

Figure 27: The dispersion curve.

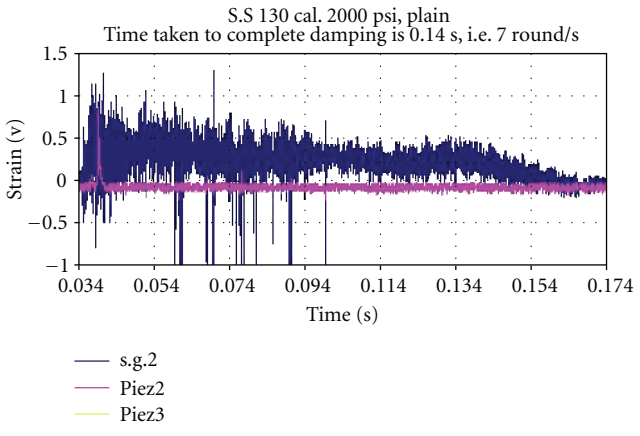

Figure 28: The radial-bending vibrations of plain tube.

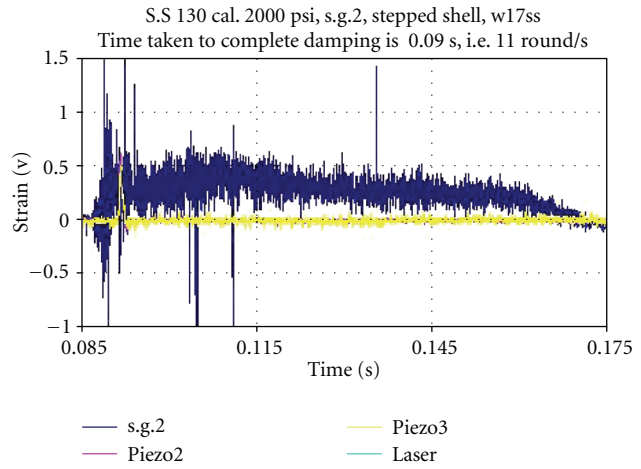

Figure 29: The radial-bending vibrations of the stiffened tube.

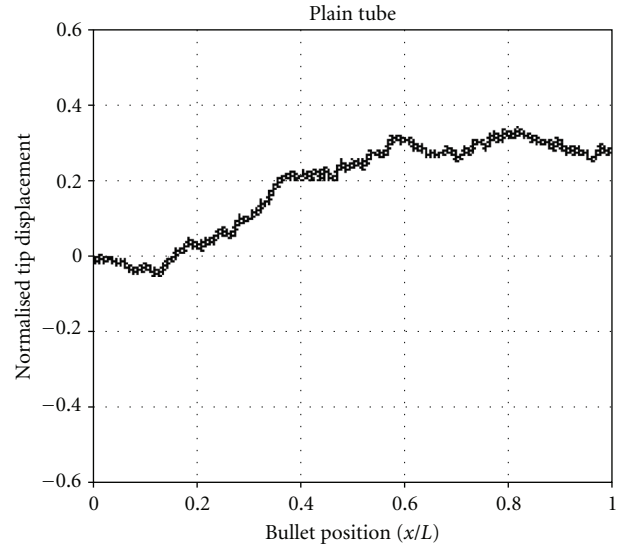

(a) Plain Tube

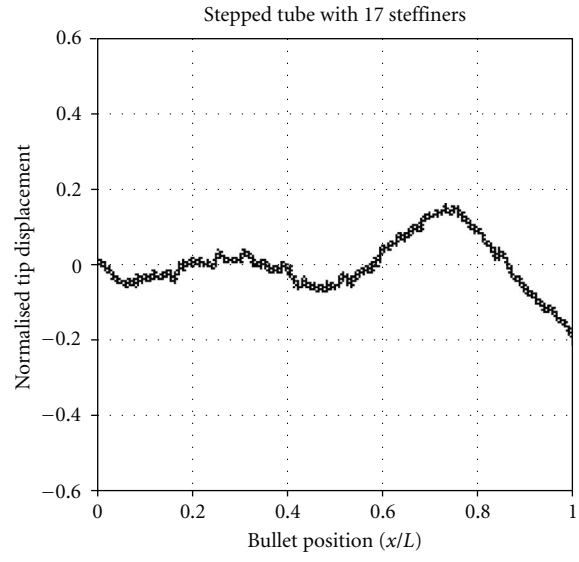

(b) Stiffened tube

Figure 30: Output signals at location number 2.

4. Conclusion

The load acting on a cylindrical shell, with added periodic stiffeners, under a transient pressure pulse propelling a pullet has been experimentally studied.

The study comprises of two modes of velocity, the first is subcritical velocity mode and the second is the supercritical velocity mode. The measured time domain strain signals have been analyzed in order to get the frequency domain modes of vibration using "wavelet transform (WT) package" instead of "fast Fourier transform (FFT)," the package is found to be very powerful, and the decomposition of the signals by this way gave us a clear and good knowledge about the phenomena that we are looking for.

Adding periodic stiffeners has a significant effect on the damping of the shell vibrations; it reaches to values between 38 and 75% for subcritical and critical velocity modes. The critical frequency of the stiffened shell is increased to about the running velocity, so the supercritical mode is changed to subcritical.

The critical velocity of the stiffened tube is increased to about 1190 m/s and the critical frequency is increased to about 200 kHz, by ratios of about 113.9% and 174.5%, respectively, when adding stiffeners which have a mass ratio of 5.6% of the mass of the plain tube.

The amplification and dispersion factors are determined and constructed; they indicated that the corresponding speed and frequencies are shifted to lower values by about 10%, less than that plain tube for subcritical velocity modes.

The radial-bending vibrations and tube muzzle motions are detected at muzzle velocity ratio of 0.99%; the results indicated that there is a possibility of significant increase in the number of rounds per second by about 36% and also increasing the pointing precision by about 47%.

Acknowledgments

This experimental work is done under the supervision of Prof. Dr. Amr Baz during the author's work as a Research Associate in University of Maryland at College Park, USA (2000–2002). This work is funded by The US Army Research Office (Grant no. DAAD199910200). Special thanks are due to Dr. Gary Anderson, the Technical Monitor, for his invaluable technical inputs.

References

[1] L. Fryba, *Vibration of Solids and Structures Under Moving Loads*, Noordhoff, Groningen, The Netherlands, 1977.

[2] D. F. Finlayson, "Characterization of the dynamic strain excitation force in gun tubes," in *Proceedings of the 9th Symposium of Gun Dynamics (SAVIAC '00)*, pp. 12.1–12.16, Baltimore, Md, USA, November 2000.

[3] T. E. Simkins, "Amplification of flexural waves in gun tubes," *Journal of Sound and Vibration*, vol. 172, no. 2, pp. 145–154, 1994.

[4] T. E. Simkins, G. A. Pflegl, and E. G. Stilson, "Dynamic strains in a 60 mm gun tube: an experimental study," *Journal of Sound and Vibration*, vol. 168, no. 3, pp. 549–557, 1993.

[5] W. M. Beltman, E. N. Burcsu, J. E. Shepherd, and L. Zuhal, "The structural response of cylindrical shells to internal shock loading," *Journal of Pressure Vessel Technology*, vol. 121, no. 3, pp. 315–322, 1999.

[6] G. O. Thomas, "The response of pipes and supports to internal pressure loads generated by gaseous detonations," *Journal of Pressure Vessel Technology*, vol. 124, no. 1, pp. 66–73, 2002.

[7] A. Baz, K. Saadeldin, and A. A. Elzahaby, "The structural response of cylindrical shells under internal moving pressure and mass," in *Proceedings of the 11th International Conference On Applied Mechanics and Mechanical Engineering (AMME '04)*, Military Technical College, Kobry Elkobbah, Cairo, Egypt, May 2004.

[8] M. Abu-Hilal and M. Mohsen, "Vibration of beams with general boundary conditions due to a moving harmonic load," *Journal of Sound and Vibration*, vol. 232, no. 4, pp. 703–717, 2000.

[9] Y.-H. Lin and M. W. Trethewey, "Finite element analysis of elastic beams subjected to moving dynamic loads," *Journal of Sound and Vibration*, vol. 136, no. 2, pp. 323–342, 1990.

[10] H. D. Nelson and R. A. Conover, "Dynamic stability of a beam carrying moving masses," *Journal of Applied Mechanics*, vol. 38, no. 4, pp. 1003–1006, 1971.

[11] C. R. Steele, "The finite beam with a moving load," *Journal of Applied Mechanics*, vol. 34, pp. 111–488, 1967.

[12] C. R. Steele, "The timoshenko beam with a moving load," *Journal of Applied Mechanics*, vol. 40, pp. 481–488, 1973.

[13] V. V. Bolotin, *The Dynamic Stability of Elastic Systems*, Holden Day, San Francisco, Calif, USA, 1964.

[14] M. Ruzzene and A. Baz, "Dynamic stability of periodic shells with moving loads," *Journal of Sound and Vibration*, vol. 296, no. 4-5, pp. 830–844, 2006.

[15] M. Ruzzene and A. Baz, "Response of periodically stiffened shells to a moving projectile propelled by an internal pressure wave," *Mechanics of Advanced Materials and Structures*, vol. 13, no. 3, pp. 267–284, 2006.

[16] O. J. Aldraihem and A. Baz, "Moving-loads-induced instability in stepped tubes," *Journal of Vibration and Control*, vol. 10, no. 1, pp. 3–23, 2004.

[17] O. J. Aldraihem and A. Baz, "Dynamic stability of stepped beams under moving loads," *Journal of Sound and Vibration*, vol. 250, no. 5, pp. 835–848, 2002.

[18] R. D. Blevins, *Formulas for Natural Frequency and Mode Shapes*, Krieger, 1995.

[19] M. L. Baron and H. H. Bleich, "Tables of frequencies and mode shapes of infinitely long thin cylindrical shells," *Journal of Applied Mechanics*, vol. 76, pp. 178–184, 1954.

[20] H. H. Bleich and M. L. Baron, "Free and long vibrations of an infinitely long cylindrical shell in an infinite acoustic medium," *Journal of Applied Mechanics*, vol. 19, pp. 167–176, 1954.

[21] S. Tang, "Dynamic response of a tube under moving pressure," *ASCE: Journal of the Engineering Mechanics*, vol. 91, no. 5, pp. 97–121, 1965.

Hindawi Publishing Corporation
Advances in Acoustics and Vibration
Volume 2009, Article ID 508076, 10 pages
doi:10.1155/2009/508076

Research Article

Dynamic Modal Analysis of Vertical Machining Centre Components

Anayet U. Patwari,[1] Waleed F. Faris,[2] A. K. M. Nurul Amin,[1] and S. K. Loh[3]

[1] *Department of Manufacturing and Materials Engineering, Faculty of Engineering, International Islamic University Malaysia (IIUM), P.O. Box 10, 50728 Kuala Lumpur, Malaysia*
[2] *Department of Mechanical Engineering, Faculty of Engineering, International Islamic University Malaysia (IIUM), P.O. Box 10, 50728 Kuala Lumpur, Malaysia*
[3] *OYL R & D Research, Faculty of Engineering, International Islamic University Malaysia (IIUM), P.O. Box 10, 50728 Kuala Lumpur, Malaysia*

Correspondence should be addressed to Waleed F. Faris, waleed@iiu.edu.my

Received 26 March 2009; Accepted 13 October 2009

Recommended by Mohammad Tawfik

The paper presents a systematic procedure and details of the use of experimental and analytical modal analysis technique for structural dynamic evaluation processes of a vertical machining centre. The main results deal with assessment of the mode shape of the different components of the vertical machining centre. The simplified experimental modal analysis of different components of milling machine was carried out. This model of the different machine tool's structure is made by design software and analyzed by finite element simulation using ABAQUS software to extract the different theoretical mode shape of the components. The model is evaluated and corrected with experimental results by modal testing of the machine components in which the natural frequencies and the shape of vibration modes are analyzed. The analysis resulted in determination of the direction of the maximal compliance of a particular machine component.

1. Introduction

The dynamic behavior of a structure in a given frequency range can be modeled as a set of individual modes of vibration. The parameters that describe each mode are natural frequency or resonance frequency (modal) damping mode shape; these are called the modal parameters. By using the modal parameters to model the structure, vibration problems caused by these resonances (modes) can be examined and understood [1–4]. In addition, the model can subsequently be used to come up with possible solutions to individual problems. Vibration occurring on machine tools has been being a serious problem for engineers for more than one century. Undesired relative vibrations between the tool and the work-piece jeopardize the quality of the machine surfaces during cutting.

Modal analysis is a process whereby a structure may be defined in terms of its natural characteristics which are the frequency, damping, and mode shapes—its dynamic properties. Since all bodies have both mass and elasticity, they are capable of vibration. Therefore, most engineering structures and machines experience some form of oscillatory motion. To better understand any structural vibration problem, the resonances of a structure need to be identified and quantified. A common way of doing this is to define the structure's modal parameters. Static and dynamic deformations of machine tool, tool holder, and cutting tool play an important role in tolerance integrity and stability in a machining process affecting part quality and productivity. Experimental modal analysis has rapidly developed as an area of science in last few years and has become as efficient as the finite element method. It is an experimental approach for solving technical problems which is a means to estimate or evaluate modal properties of a mechanical structure. Modal analysis is vital to understanding and optimizing the inherent dynamic behavior of

structures, leading to lighter, stronger, and safer structure with better performance. In modal analysis, a mathematical model of a structure's dynamic behavior is obtained. The mathematical model consists of a set of mode shapes each with an associated natural frequency and modal damping. These modal parameters provide a complete description of the structure's dynamic behavior. Baker and his coresearchers used finite element method to analyze the instability of machining process [5]. They created a structural model of machine tool system using the commercial FE code, ANSYS, without any experimental tests. In this model the bed of machine tool, spindle, and tool holder, as steel blocks, are modeled. The integrity of these models is not confirmed by experimental results. In another research with the aim of analysis of chatter phenomena, the tool's natural frequencies and the shape of their vibration modes were obtained by modal testing results. In this case the variations of acoustic emission signal during chatter are analyzed, so that it can be used for chatter detection in machining duration [6]. Many researchers [7–9] tried to analyze the static and dynamic analysis of the structure involved in machining system by resting using stiffness measurements and modal analysis. Talantov and Amin have observed that chatter arising during turning is a result of resonance, caused by mutual interaction of the vibrations due to serrated elements of the chip and the natural vibrations of the system components, for example, the spindle and the tool holder [10–12]. The chatter phenomena were indicated by the some of the researchers as a resonance effect where system components played a vital role. So it is important to extract the accurate mode shape of the dominating components of machine structure to identify the chatter formation causes. The paper is focused at dynamic properties of a vertical milling machine, namely, at the resonance frequencies and vibration shapes of a vertical machining centre components. All this properties are identified by measurements. The machine tool vibration was excited by impulse force and a response of excited vibration was recorded. The measurement points for vibration were selected at the different location of spindle, tool, and collet.

2. Simplified Modal Analysis of Milling Machine

Aiming to investigate the vibration phenomena occurring occasionally at the different components of milling machine experimental and analytical modal analyses were performed. The study focused on extracting the mode shape of the dominating components of the milling machine in order to ensure resonance phenomena as a cause of chatter. In a first step the significant eigen-frequencies with corresponding mode shapes were obtained by means of an experimental modal analysis (EMA). Subsequently, the dynamic behavior of the machine components was simulated using an ABAQUS FE model. The comparison of the eigen-frequencies based on FE calculations with their experimental counterparts proved in general quite satisfactory correlation.

3. Experimental Modal Analysis

3.1. Measurement Hardware. A vibration measurement generally requires several hardware components. The basic hardware elements required consist of a source of excitation, called an exciter (Impulse hammer), for providing a known or controlled input force to the structure, a transducer to convert the mechanical motion of the structure into a electrical signal, a signal conditioning amplifier, and an analysis system in which modal analysis program resides.

The schematic diagram of hardware used performing in a vibration test is shown in Figure 1. The different equipments that have been used are listed as follows: Pulse Front-end (Data Acquisition), Impact Hammer, USB Dongle, Accelerometers, Impact Hammer cable, Accelerometer cables, Pulse Front-End Power Supply, TCP/IP Cross Cable, and Bee's wax.

3.2. Test Procedures. The different milling machine components were identified which play a dominating role for the chatter generation. The natural frequency of the different components was measured using modal analysis under static and dynamic conditions and consequently the different mode shapes were identified. Initially excited frequencies were monitored during the operational mode under no-load condition. It is easy to record a response in vibration during machining but almost impossible to measure the mentioned dynamic force. Therefore, the force measurement was replaced by measurement of impulse response to the impact force excited by a hammer, whose tip was fitted by a force sensor. As the goal of these measurements was to evaluate frequency transfer function, the responses at various machine points with respect to a reference point were recorded and analyzed. The reference point was selected at the different location shown in Figure 2.

(i) *Knocking test.* The natural frequencies of the different components were extracted from the recorded FFT diagram. One accelerometer was connected to the component; the natural frequency data from the FFT graph was recorded by knocking the different components using the impact hammer.

(ii) *Operational test.* The dominating frequencies were identified considering high values based on the natural frequencies obtain from the knocking test during no-load operating condition. Accelerometers are connected to the components and data were recorded in Auto spectrum graph. The time excitation, the coherence response excitation, and time response excitation were also recorded to investigate the quality of the signal as shown in Figure 3.

Experimental Modal Analysis is based on determining the modal parameters by testing, unlike Analytical Modal Analysis, where the modal parameters are derived from Finite Element Models (FEMs). There are two ways of doing Experimental Modal Analysis: Classical Modal Analysis and

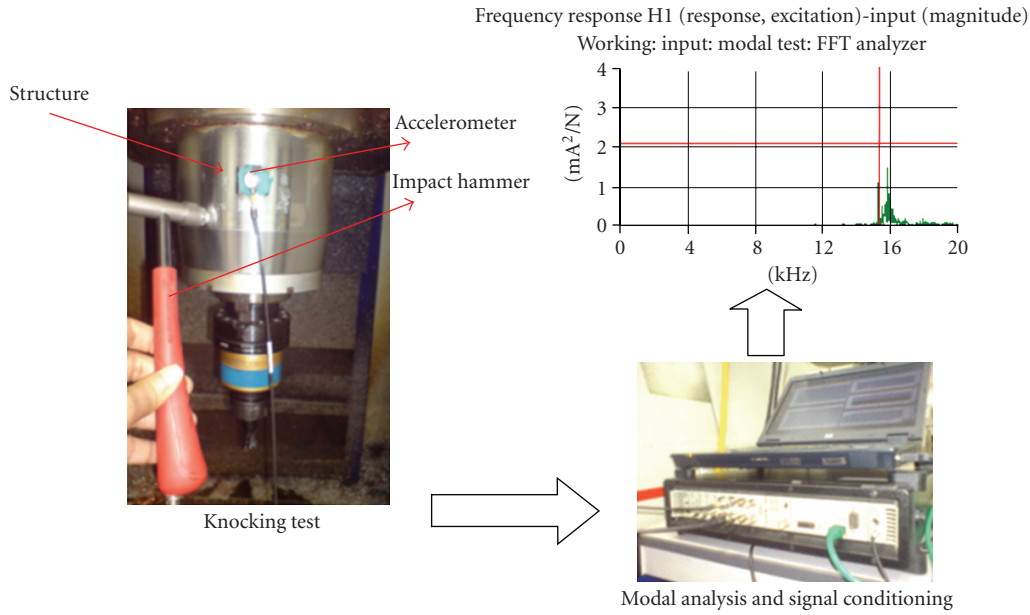

Figure 1: Experimental modal analysis test set-up.

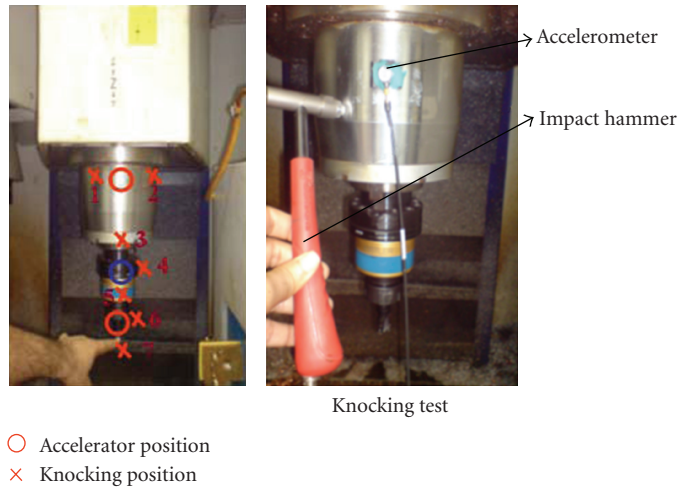

Figure 2: Position of Accelerometer and knocking point at different components of milling machine.

Operational Modal Analysis. In Classical Modal Analysis frequency response functions (or impulse response functions) are calculated from measured input forces and output responses of a structure shown in Figures 3-4. Much of the analysis in modal testing is performed in the frequency domain inside the analyzer. The analyzer task is to convert analog time domain signal into digital frequency domain information compatible with digital computing and then to perform the required computations with these signals. Figures 3-4 indicate the frequency domain information by Fast Fourier Transform for the domination components of vertical machining centre like tool-holder and collet and spindle casing. As it is very difficult to extract the inner spindle mode shape, so operational modal analysis was done for inner spindle.

4. Operational Modal Analysis

Operational Modal Analysis is based on measuring only the output of a structure and using the ambient and operating forces as unmeasured input. It is used instead of classical mobility-based modal analysis for accurate modal identification under actual operating conditions, and in situations where it is difficult or impossible to control an artificial excitation of the structure.

In the milling machine structure the inner spindle is surrounded by the outer spindle; as a result it is not possible to extract the mode shape using knocking test. Operational modal analysis was carried out to find out the mode shape of the inner spindle using load and no-load conditions as shown in Figure 5.

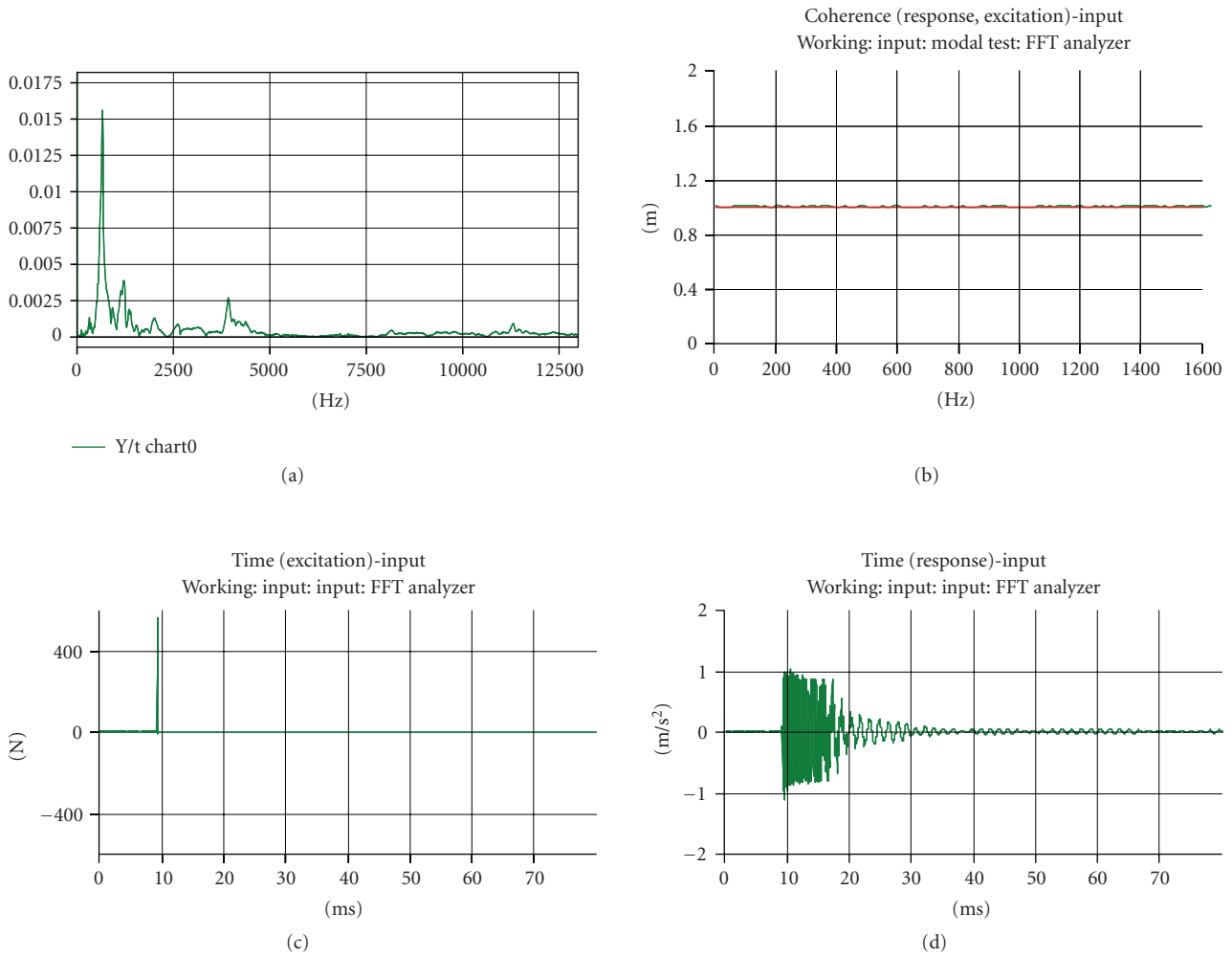

Figure 3: Experimental modal analysis responses of tool holder.

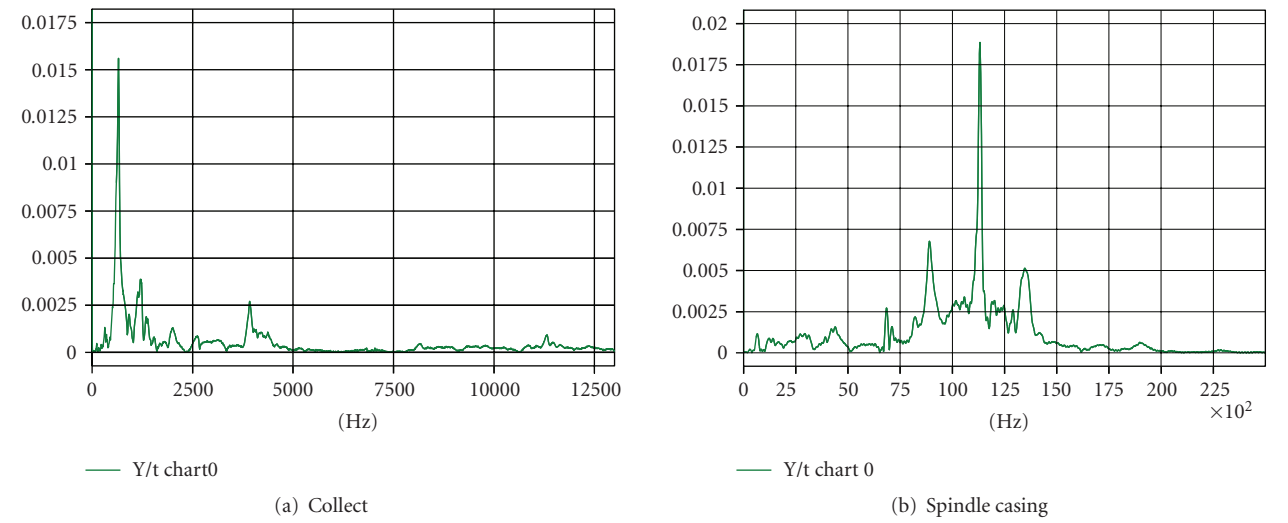

Figure 4: Experimental modal analysis power spectrum responses (FFT); (a) Collet and (b) Spindle casing of vertical machining centre.

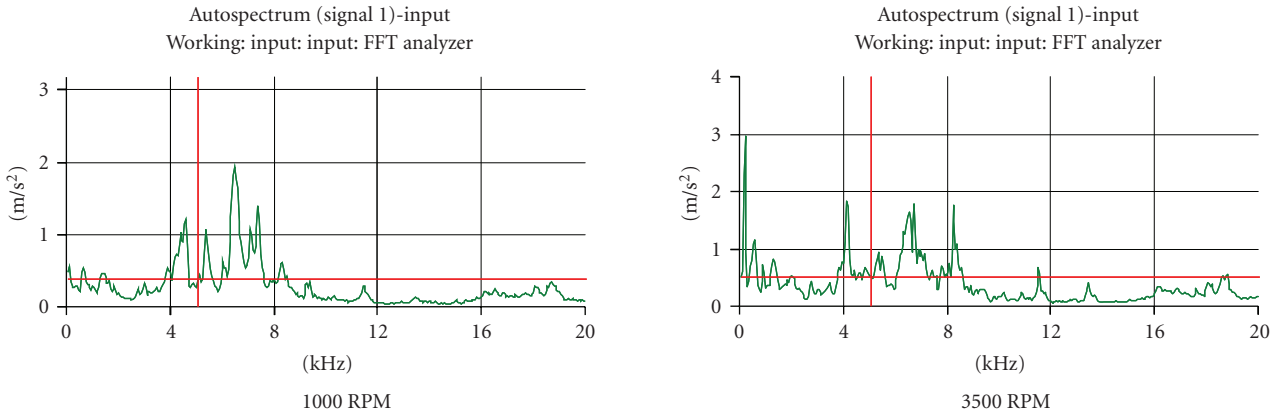

(a) Inner spindle operational deflection shape with no load. Spindle mode shape: 4394 Hz, 6866 Hz, 8294 Hz

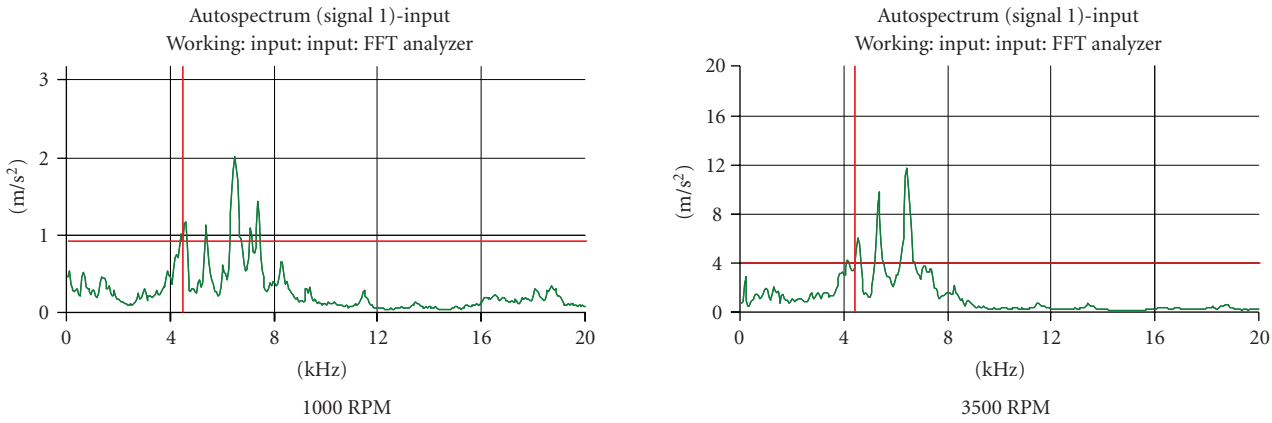

(b) Inner spindle operational deflection shape with load. Spindle mode shape: 4394 Hz, 6866 Hz, 8294 Hz

Figure 5: Operational Modal analysis of inner spindle with no-load and load conditions.

5. Procedures: FE Modeling

In order to make a finite element model, a three-dimensional geometrical model of machine's structure with CATIA software has been developed and then converted to igs. format for further analysis by ANSYS software. This model provides natural values and response frequency extraction. The observation of vibration modes of machine tool components is three-dimensional shapes which provides better capability to the analysis of vibration model. The model is applied on vertical machining centre. The different components of the machine were measured and designed by CATIA software. The designed models were three-dimensional models. The geometrical model of the machine components is shown in Figure 6. After modeling selection, the necessary input data as material properties such as modulus of elasticity, Poisson ratio, and density are applied. The elements used in the FEM model for mesh generation is quadratic tetrahedral element. The element distribution is uniform to exceed boundary and it is so that in the parts with relatively small dimensions like spindle, tool holder, collet, and so forth. the element dimensions are finer and controlled. Afterwards, boundary conditions on supporting are applied on the earth connection of machine tool and finally modal analysis has been done to obtain natural frequencies. In continuation, fine screening of the finite element model is accomplished to match the natural frequencies results from experimental modal analysis.

6. FE Modal Analysis

Modal analysis has been done on the three different components of vertical machining centre using finite element model to determine the natural frequency of machine tool structure elements and to discrete them from each other. These models are as follows:

(i) model number 1: complete model of spindle both outer and inner.

(ii) model number 2: complete model of collet with chuck case.

(iii) model number 3: complete model of tool holder.

7. Results and Discussion

A comparison of calculated modes with their measured counterparts is very helpful in general to verify the quality

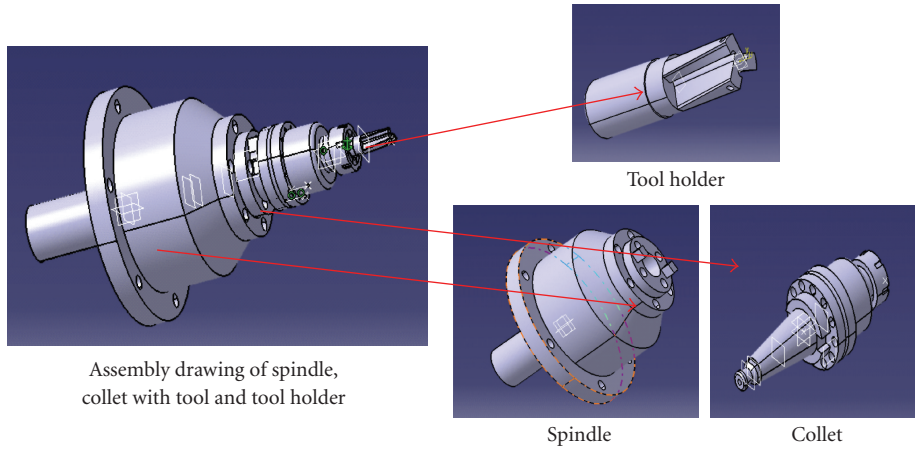

Figure 6: CATIA model of the different components of vertical machining centre.

of an FE model for dynamic simulation purposes and to detect any possible improvements. The modal-analyzed natural frequencies of these models via ABAQUS software of different components at different mode shapes are shown in Figures 5–7. The results of analysis of the calculated and experimental mode shape are mentioned in the result analysis section.

Model Number 1: Complete Model of Spindle Both Outer and Inner of Eigen-Frequency Analysis. Finite element analysis of the inner and outer spindle is performed using ABAQUS. The calculated distortions of the each element are shown in Figure 7 at different mode shapes. The elements used in the FEM model for mesh generation are quadratic tetrahedral element. It has been observed from the calculated results that there are five prominent mode shape of the spindle. In most of the mode shape the distortion in the inner spindle is more significant than the outer spindle.

Model Number 2: Complete Model of Collet for Eigen-Frequency Analysis. Finite element analysis of the collet is again performed using ABAQUS. The calculated distortions of the each element are shown in Figure 8 at different mode shapes.

Model Number 3: The Model of Tool Holder and Selected Eigenmodes of the Components. Finite element analysis of the tool holder was performed using ABAQUS. The calculated distortions of each element are shown in Figure 9 at different mode shapes.

8. Correlation EMA/FEA

The natural frequencies obtained from modal analysis of system testing results and FEM are shown in the Tables 1–3. Table 1 shows natural frequencies obtained from the modal analysis of finite element models and modal testing results of spindle both inner and outer and the amount percent of their errors in the different cases.

Table 1: Natural frequencies analysis of spindle.

	Different major mode shape (Hz)				
Spindle	Inner Spindle			Outer spindle	
Condition	1st	2nd	3rd	1st	2nd
Experimental	4394	6866	8294	9009	11371
Theoretical	4322	6389	8004	9520	10291
Error (%)	1.67	7.47	3.62	5.37	10.49

Table 2: Natural frequencies analysis of Collet.

Collet	Different major mode shape (Hz)			
Condition	1st	2nd	3rd	4th
Experimental	659	2032	3955	5169.7
Theoretical	770.77	2318.9	3673.6	5318.2
Error(%)	14.50	12.37	7.66	2.79

Table 3: Natural frequencies analysis of Tool Holder.

Tool Holder	Different major mode shape (Hz)		
Condition	1st	2nd	3rd
Experimental	2081	8892	11352
Theoretical	2944	10099	10454
Error (%)	29.31	11.95	8.59

Table 2 shows natural frequencies obtained from the modal analysis of finite element models and modal testing results of collet and the amount percent of their errors in the different cases.

Table 3 shows natural frequencies obtained from the modal analysis of finite element models and modal testing results of tool holder and the amount percent of their errors in the different cases.

The first and second vibration modes of outer spindle are almost similar to the second and third vibration modes of tool holder, respectively. The vibration frequency region of spindle model is much higher than the vibration frequencies of collet model. The percentage error levels for all the

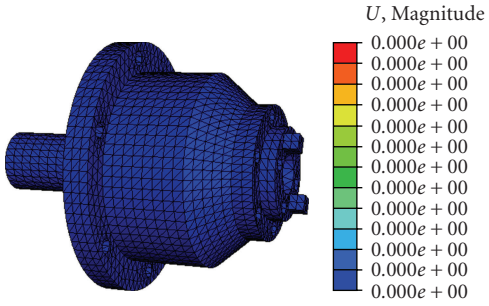

ODB: spindle.odb ABAQUS/standard version 6.6 × 1
Wed Jun 04 12:12:56 malay peninsula

Step: Frequency, frequency analysis
Increment 0: Base state
Primary var: U, magnitude
Deformed var: U deformation scale factor: $1.000e + 00$

(a) Base state

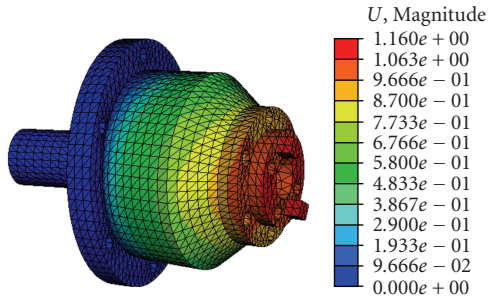

ODB: spindle.odb ABAQUS/standard version 6.6 × 1
Wed Jun 04 12:12:56 malay peninsula standard

Step: Frequency, frequency analysis
Mode 4: Value = $7.37518E + 08$ Freq = 4322.2 cycles/time
Primary var: U, magnitude
Deformed var: U deformation scale factor: $3.102e + 01$

(b) Mode: 4322 Hz

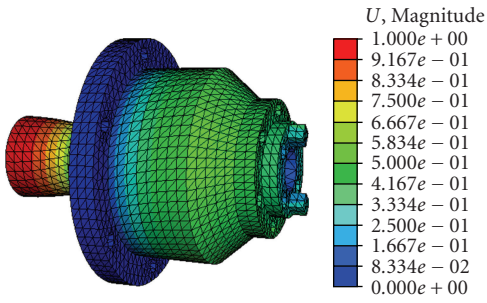

ODB: spindle.odb ABAQUS/standard version 6.6 × 1
Wed Jun 04 12:12:56 malay peninsula standard

Step: Frequency, frequency analysis
Mode 6: Value = $1.61157E + 09$ Freq = 6389.2 cycles/time
Primary var: U, magnitude
Deformed var: U deformation scale factor: $3.102e + 01$

(c) Mode: 6389 Hz

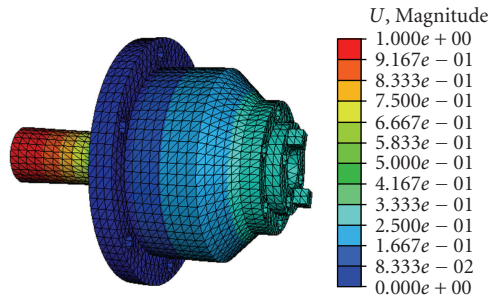

ODB: spindle.odb ABAQUS/standard version 6.6 × 1
Wed Jun 04 12:12:56 malay peninsula standard

Step: Frequency, frequency analysis
Mode 7: Value = $2.52912E + 09$ Freq = 8004 cycles/time
Primary var: U, magnitude
Deformed var: U deformation scale factor: $3.102e + 01$

(d) Mode: 8004 Hz

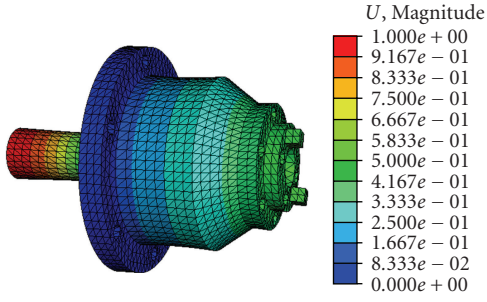

ODB: spindle.odb ABAQUS/standard version 6.6 × 1
Wed Jun 04 12:12:56 malay peninsula standard

Step: Frequency, frequency analysis
Mode 10: Value = $3.57864E + 09$ Freq = 9520.9 cycles/time
Primary var: U, magnitude
Deformed var: U deformation scale factor: $3.102e + 01$

(e) Mode: 9520 Hz

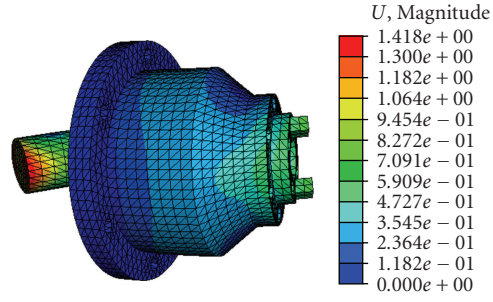

ODB: spindle.odb ABAQUS/standard version 6.6 × 1
Thu Jun 05 12:19:22 malay peninsula standard

Step: Frequency, frequency analysis
Mode 12: Value = $4.18066E + 09$ Freq = 10291 cycles/time
Primary var: U, magnitude
Deformed var: U deformation scale factor: $3.102e + 01$

(f) Mode: 10291 Hz

Figure 7: Selected Eigenmodes of the Spindle by FE Analysis.

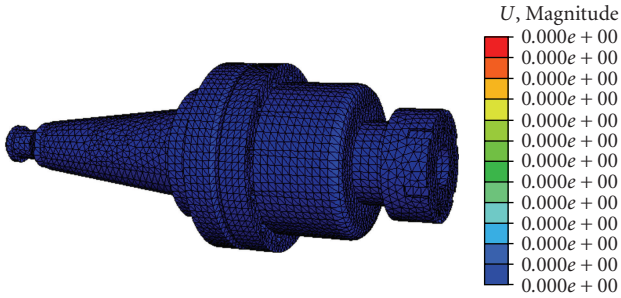

ODB: assembly_spindle.odb ABAQUS/standard version 6.6 × 1
Mon Jun 09 18:11:02 malay peninsula standard

Step: Frequency, frequency analysis
Increment 0: Base state
Primary var: U, magnitude
Deformed var: U deformation scale factor: 1.000e + 00

(a) Base state

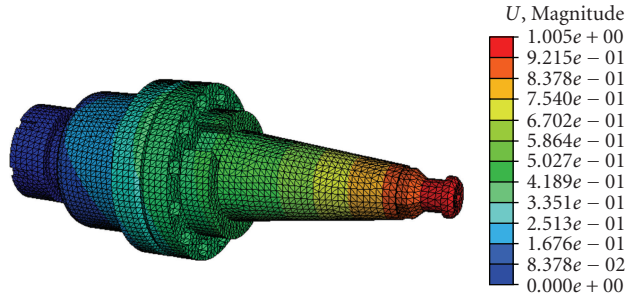

ODB: collet.odb ABAQUS/standard version 6.6 × 1
Thu May 22 15:18:55 malay peninsula standard

Step: Frequency analysis, frequency analysis
Mode 1: Value = 2.34537E + 07 Freq = 770.77 cycles/time
Primary var: U, magnitude
Deformed var: U deformation scale factor: 2.300e + 01

(b) Mode: 770.77 Hz

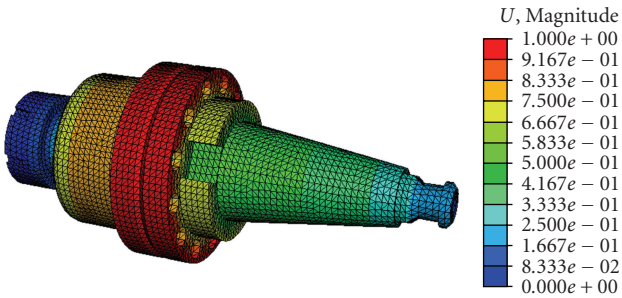

ODB: collet.odb ABAQUS/standard version 6.6 × 1
Thu May 22 15:18:55 malay peninsula standard

Step: Frequency analysis, frequency analysis
Mode 3: Value = 2.12287E + 08 Freq = 2318.9 cycles/time
Primary var: U, magnitude
Deformed var: U deformation scale factor: 2.300e + 01

(c) Mode: 2318.9 Hz

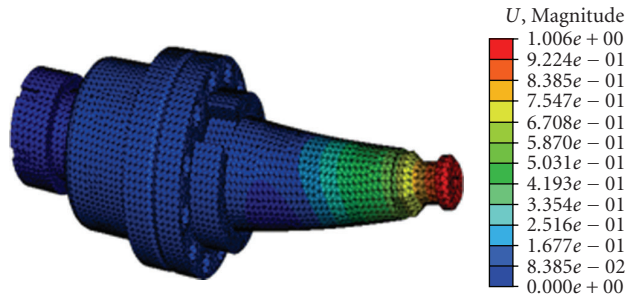

ODB: collet.odb ABAQUS/standard version 6.6 × 1
Thu May 22 15:18:55 malay peninsula standard

Step: Frequency analysis, frequency analysis
Mode 4: Value = 5.32789E + 08 Freq = 3673.6 cycles/time
Primary var: U, magnitude
Deformed var: U deformation scale factor: 2.300e + 01

(d) Mode: 3673.6 Hz

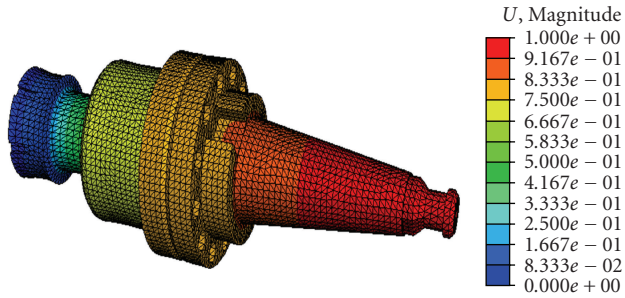

ODB: collet.odb ABAQUS/standard version 6.6 × 1
Thu May 22 15:18:55 malay peninsula standard

Step: Frequency analysis, frequency analysis
Mode 6: Value = 1.11659E + 09 Freq = 5318.2 cycles/time
Primary var: U, magnitude
Deformed var: U deformation scale factor: 2.300e + 01

(e) Mode: 5318.2 Hz

Figure 8: Selected Eigenmodes of the Collet by FE Analysis.

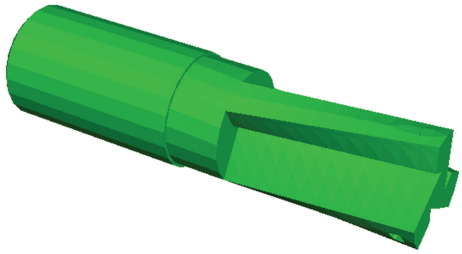

ODB: tool_holder.odb ABAQUS/standard version 6.6 × 1
Wed Mar 05 13:26:05 malay peninsula

Step: Frequency, frequency extraction
Increment 0: Base state
Deformed var: U deformation scale factor: 1.000e + 0

(a) Base state

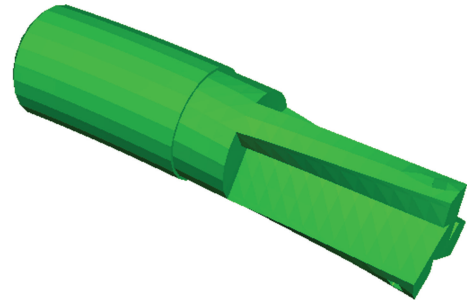

ODB: tool_holder.odb ABAQUS/standard version 6.6 × 1
Wed Mar 05 13:26:05 malay peninsula

Step: Frequency, frequency extraction
Mode 1: Value = 3.42154E + 08 freq = 2944 cycles/time
Deformed var: U deformation scale factor: 8.000e + 0

(b) Mode: 2944 Hz

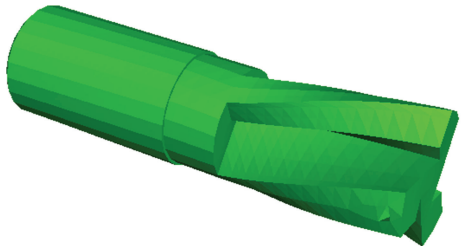

ODB: tool_holder.odb ABAQUS/standard version 6.6 × 1
Wed Mar 05 13:26:05 malay peninsula

Step: Frequency, frequency extraction
Mode 3: Value = 4.02660E + 09 freq = 10099 cycles/time
Deformed var: U deformation scale factor: 8.000e + 0

(c) Mode: 10099 Hz

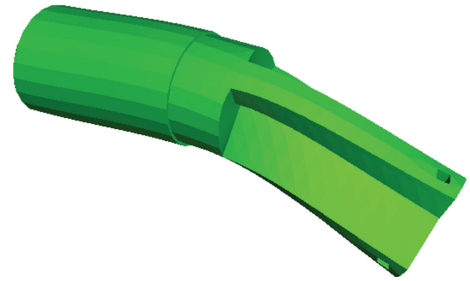

ODB: tool_holder.odb ABAQUS/standard version 6.6 × 1
Wed Mar 05 13:26:05 malay peninsula

Step: Frequency, frequency extraction
Mode 4: Value = 4.31477E + 09 freq = 10454 cycles/time
Deformed var: U deformation scale factor: 8.000e + 0

(d) Mode: 10454 Hz

Figure 9: Selected Eigenmodes of the Tool Holder by FE Analysis.

components are within the accepted ranges and the high error in some of them might be referred to the boundary conditions specification, because it is not easy to simulate the realistic boundary conditions for such complicated system.

9. Conclusion

In this paper a finite element model is used to analyze the mode frequencies and shapes of different machining components and hence compare the results with the experimental one. This model is produced in CATIA software based on the real dimensions of vertical machining centre (model: MCFV 1060LR) machine and analysis was done by ABAQUS software. According to the model analysis, the natural frequencies and vibration modes shape of the model in spindle, collet, and tool holder cases were determined and evaluated. The comparison between natural frequencies of finite element modeling and model testing shows the closeness of the results. From the results, it has been observed that the suitable frequency ranges for end milling will be up to 12000 Hz. This research work will help to find out the natural frequencies of the components and hence predicting the chatter formation zone as resonance phenomena.

References

[1] D. J. Inman, *Engineering Vibration*, Prentice-Hall, Englewood Cliffs, NJ, USA, 3rd edition, 2007.

[2] T. C. Huang, *Modal Analysis Modeling, Diagnostics and Control-Analytical and Experimental*, ASME, New York, NY, USA, 1991.

[3] C. W. de Silva, *Vibration and Shock Hand Book*, Taylor & Francis, Boca Raton, Fla, USA, 2005.

[4] N. M. M. Maia and J. M. M. E. Silva, *Theoretical and Experimental Modal Analysis*, John Wiley & Sons, New York, NY, USA, 1997.

[5] J. R. Baker and K. E. Rouch, "Use of finite element structural models in analyzing machine tool chatter," *Finite Elements in Analysis and Design*, vol. 38, no. 11, pp. 1029–1046, 2002.

[6] J. Lee and D.-H. Kim, "Experimental modal analysis and vibration monitoring of cutting tool support structure," *International Journal of Mechanical Sciences*, vol. 37, no. 11, pp. 1133–1146, 1995.

[7] Y. Altintas, *Manufacturing Automation*, Cambridge University Press, London, UK, 2000.

[8] E. Budak and Y. Altintas, "Identification of peripheral milling conditions for improved dimensional accuracy," *International Journal of Machine Tools and Manufacture*, vol. 34, no. 7, pp. 907–918, 1994.

[9] J. Tlusty and M. Polacek, "The stability of machine tools against self excited vibration in machining," in *Proceedings of International Research in Production Engineering*, pp. 465–474, ASME, Pittsburgh, Pa, USA, 1963.

[10] N. V. Talantov, A. K. M. N. Amin, and N. P. Chereomushnikov, "Temperature deformation laws of chatter formation during metal cutting process," in *Proceedings of the 5th Soviet National Conference "Teplophysika Technologichieskikh Processov,"*, p. 92, Volgograd, Russia, 1980.

[11] A. K. M. N. Amin, "Investigation of the mechanism of chatter formation during metal cutting process," *Mechanical Engineering Bulletin*, vol. 6, no. 1, pp. 11–18, 1983.

[12] A. K. M. N. Amin, *Investigation of the laws governing the formation of chatter during metal cutting processes and the influence of chatter on tool wear*, Ph.D. thesis, Georgian Polytechnic Institute, Atlanta, Ga, USA, 1982.

Hindawi Publishing Corporation
Advances in Acoustics and Vibration
Volume 2009, Article ID 317890, 7 pages
doi:10.1155/2009/317890

Research Article

Designing 2D Phononic Crystal Slabs with Transmission Gaps for Solid Angle as well as Frequency Variation

Sven M. Ivansson

Department of Underwater Research, Swedish Defence Research Agency, FOI Kista, 16490 Stockholm, Sweden

Correspondence should be addressed to Sven M. Ivansson, sven.ivansson@foi.se

Received 29 January 2009; Accepted 15 June 2009

Recommended by Mohammad Tawfik

Phononic crystals (PCs) can be used as acoustic frequency selective insulators and filters. In a two-dimensional (2D) PC, cylindrical scatterers with a common axis direction are located periodically in a host medium. In the present paper, the layer multiple-scattering (LMS) computational method for wave propagation through 2D PC slabs is formulated and implemented for general 3D incident-wave directions and polarizations. Extensions are made to slabs with cylindrical scatterers of different types within each layer. As an application, the problem is considered to design such a slab with small sound transmittance within a given frequency band and solid angle region for the direction of the incident plane wave. The design problem, with variable parameters characterizing the scatterer geometry and material, is solved by differential evolution, a global optimization algorithm for efficiently navigating parameter landscapes. The efficacy of the procedure is illustrated by comparison to a direct Monte Carlo method.

1. Introduction

Just as photonic crystals can be used to manipulate light, phononic crystals (PCs) with inclusions in a lattice with single, double, or triple periodicity can be used to manipulate sound [1]. When a sound wave of a certain frequency penetrates the PC, the energy is scattered by the inclusions. According to Bragg's law, constructive and destructive interference appears in certain directions. It follows that transmission and/or reflection for certain frequencies can be absent (band gaps), even for all angles of incidence (absolute band gaps). The band gaps are ideal and fully developed only in space-filling PCs. In a PC slab with finite thickness, the "band-gap wavefields" are reduced significantly but they do not vanish throughout the gap. Acoustic frequency selective insulators and filters are possible applications.

Several computational methods have been adapted and developed to study wave propagation through PCs. Two such methods are the purely numerical finite-difference time domain (FDTD) method and the semianalytical layer multiple-scattering (LMS) method, which is developed from Korringa-Kohn-Rostoker theory [2]. These methods complement each other. Advantages with the LMS method are its computational speed, which makes it useful for forward modeling in connection with extensive optimization computations, and the physical insight it provides. It appears that the LMS method was first developed for the 3D case with spherical scatterers [3, 4], and recent review papers include Sigalas et al. [5] and Sainidou et al. [6].

The LMS method has also been applied to the 2D case with infinite cylindrical scatterers. It is mainly the in-plane propagation case that has been considered [7–11], for which one space dimension can be eliminated in the wave equations. Out-of-plane propagation has been treated by Mei et al. [12] and, for band structure calculations, somewhat earlier by Wilm et al. [13] (using the plane-wave method) and by Guenneau et al. [14].

In the present paper, basic LMS equations for propagation of plane waves of any direction through a 2D PC slab are first provided in Section 2. The Poisson summation formula and the Graf addition theorem are utilized. As shown in Section 3, different types of scatterers at the same interface can be allowed, which represents an extension as compared to the treatment in [12]. Coupled equation systems are derived for the different scatterer types. For 3D PC slabs, a corresponding extension has recently proved useful for applications to design of anechoic coatings [15].

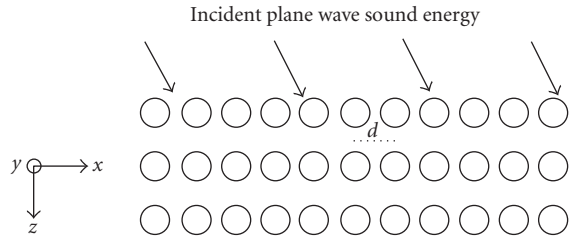

Figure 1: Horizontal xy coordinates and a z depth coordinate axis are introduced. There are three scatterer interfaces in this illustration. The medium is periodic with period d in the x direction, although only finitely many cylindrical scatterers are shown at each interface, and the cylinder axes are parallel to the y-axis.

Applications to design of 2D PC slabs with broad transmission gaps for incident waves of in-plane as well as out-of-plane directions are presented in Section 4. The design problem is equivalent to a nonlinear optimization problem, and differential evolution [16], a global optimization technique from inverse theory, is used. A 2D PC slab example from Mei et al. [12], with lead cylinders in an epoxy host, is revisited. Geometrical and material parameter values are varied to position and widen its band gap.

2. Basic 2D Layer Multiple-Scattering Computational Method

As in Figure 1, a right-hand Cartesian xyz coordinate system is introduced in a fluid-solid medium surrounded by homogeneous half-spaces. The horizontal directions are x and y. The medium is periodic with period d in the x direction and uniform in the y direction.

Sound waves with time dependence $\exp(-i\omega t)$, to be suppressed in the formulas, are considered, where ω is the angular frequency. It follows that an incident plane wave with horizontal wavenumber vector $\mathbf{k}_{\|} = (k_{\|}, \kappa, 0)$ will give rise to a linear combination of reflected and transmitted plane waves with displacement vectors

$$\mathbf{u}(\mathbf{r}) = \exp\left(i\,\mathbf{K}^{s}_{\mathbf{g}j}\cdot\mathbf{r}\right)\cdot\mathbf{e}_j. \tag{1}$$

Here, $\mathbf{r} = (x, y, z)$, $j = 1, 2, 3$ for a wave of type P,SV,SH, respectively, $s = +(-)$ for a wave in the positive (negative) z direction, and

$$\begin{aligned}\mathbf{K}^{\pm}_{\mathbf{g}j} &= \mathbf{k}_{||} + \mathbf{g} \pm \left[\left(\frac{\omega}{c_j}\right)^2 - \left|\mathbf{k}_{||} + \mathbf{g}\right|^2\right]^{1/2}\cdot(0,0,1)\\ &= \frac{\omega}{c_j}\cdot(\sin\theta\cos\varphi, \sin\theta\sin\varphi, \cos\theta),\end{aligned} \tag{2}$$

where $\mathbf{g}$ belongs to the reciprocal lattice

$$\mathbf{g} = \left(k_x, k_y, 0\right) = \left(\frac{2\pi m}{d}, 0, 0\right) \tag{3}$$

with m running over the integers. Furthermore, c_1 is the compressional-wave velocity α and $c_2 = c_3$ are the shear-wave velocity β. The angular variables θ, φ of $\mathbf{K}^{\pm}_{\mathbf{g}j}$ are defined by (2), with a possibly complex $\cos\theta$. The vectors $\mathbf{e}_j = \mathbf{e}_j(\mathbf{K}^{\pm}_{\mathbf{g}j})$ are defined by $\mathbf{e}_1 = (\sin\theta\cos\varphi, \sin\theta\sin\varphi, \cos\theta)$, $\mathbf{e}_2 = (\cos\theta\cos\varphi, \cos\theta\sin\varphi, -\sin\theta)$, $\mathbf{e}_3 = (-\sin\varphi, \cos\varphi, 0)$. It is convenient also to introduce the compressional- and shear-wave wavenumbers $k_p = \omega/\alpha$ and $k_s = \omega/\beta$.

As detailed in [17], for example, and references therein, reflection and transmission matrices R_B,T_B and R_A,T_A can now be introduced, for the discrete set of waves specified by (1)–(3). The mentioned reference concerns the doubly periodic case for a 3D PC, with periodicity in the y direction as well, but the R/T matrix formalism is the same. There are three scatterer interfaces in the illustration of Figure 1. Individual R/T matrices can be combined recursively [18, 19]. Layer thicknesses, as well as translations of individual scatterer interfaces in the x direction, are conveniently accounted for by phase shifts of the complex amplitudes of the plane-wave components.

2.1. Interface with Periodically Distributed Scatterers of a Common Type. Explicit expressions for the R/T matrices are well known for an interface between two homogeneous half-spaces [19]. To handle an interface with periodically distributed scatterers, as one of the three in Figure 1, the following cylindrical vector solutions to the wave equations can be used [12]:

$$\mathbf{u}^{L}_{l\kappa}(\mathbf{r}) = \frac{i}{k_p}\,\nabla\,\left[f_l(pr)\,\exp(i\,l\,\eta)\exp(i\,\kappa\,y)\right], \tag{4}$$

$$\mathbf{u}^{M}_{l\kappa}(\mathbf{r}) = \frac{1}{k_s}\,\nabla\times\mathbf{u}^{N}_{l\kappa}(\mathbf{r}), \tag{5}$$

$$\mathbf{u}^{N}_{l\kappa}(\mathbf{r}) = \frac{1}{k_s}\,\nabla\times\left[f_l(qr)\exp(i\,l\,\eta)\exp(i\,\kappa\,y)\mathbf{e}_y\right], \tag{6}$$

where cylindrical coordinates r, η, y are used according to $\mathbf{r} = (r\sin\eta, y, r\cos\eta)$, and $\mathbf{e}_y = (0, 1, 0)$. The index $l = 0, \pm1, \pm\ldots$, and κ is a real number. Residual wavenumbers p, q are defined by

$$p = \left(k_p^2 - \kappa^2\right)^{1/2}, \qquad q = \left(k_s^2 - \kappa^2\right)^{1/2}. \tag{7}$$

The notation $\mathbf{u}^{0L}_{l\kappa}(\mathbf{r})$, $\mathbf{u}^{0M}_{l\kappa}(\mathbf{r})$, $\mathbf{u}^{0N}_{l\kappa}(\mathbf{r})$ and $\mathbf{u}^{+L}_{l\kappa}(\mathbf{r})$, $\mathbf{u}^{+M}_{l\kappa}(\mathbf{r})$, $\mathbf{u}^{+N}_{l\kappa}(\mathbf{r})$ is used for the two basic cases with f_l as the Bessel function J_l and f_l as the Hankel function $H^{(1)}_l$, respectively.

For scatterers at

$$\mathbf{R} = (x, y, z) = (md, 0, 0), \tag{8}$$

where d is the lattice period and m runs over the integers, and for an incident plane wave as in (1), the total scattered field $\mathbf{u}_{\mathrm{sc}}$ can be written as (cf. [3])

$$\mathbf{u}_{\mathrm{sc}}(\mathbf{r}) = \sum_{Pl}\left[b^{+P}_l\sum_{\mathbf{R}}\exp(i\,\mathbf{k}_{||}\cdot\mathbf{R})\cdot\mathbf{u}^{+P}_{l\kappa}(\mathbf{r}-\mathbf{R})\right], \qquad P = L, M, N, \tag{9}$$

where κ is the y component of $\mathbf{k}_{||}$.

The vector $\mathbf{b}^+ = \{b_l^{+P}\}$ is determined by solving the equation system

$$(\mathbf{I} - T \cdot \Omega) \cdot \mathbf{b}^+ = T \cdot \mathbf{a}^0, \tag{10}$$

where $\mathbf{I}$ is the appropriate identity matrix, $\mathbf{a}^0 = \{a_l^{0P}\}$ gives the coefficients for expansion of the incident plane wave in regular cylindrical waves $\mathbf{u}_{l\kappa}^{0P}(\mathbf{r})$, $\Omega = \Omega(k_\parallel d, pd, qd)$ is the lattice translation matrix $\{\Omega_{l;l'}^{PP'}\}$, and $T = \{T_{l;l'}^{PP'}\}$ is the transition matrix for an individual scatterer. Specifically, $\mathbf{b}' = \Omega \cdot \mathbf{b}^+$ and $\mathbf{b}^+ = T \cdot (\mathbf{a}^0 + \mathbf{b}')$ where $\mathbf{b}' = \{b_l'^P\}$ gives the coefficients for expansion in regular cylindrical waves $\mathbf{u}_{l\kappa}^{0P}(\mathbf{r})$ of the scattered field from all scatterers except the one at the origin.

The R/T matrices are obtained, finally, by transforming the expansion (9) to plane waves of the type (1). Specifically, (9) can be rewritten as

$$\mathbf{u}_{\mathrm{sc}}(\mathbf{r}) = \sum_{\mathbf{g}} \sum_{j=1,2,3} \Delta(d\mathbf{g}, j; k_\parallel d, \kappa d, pd, qd, \mathbf{b}^+) \times \exp\left(i\, \mathbf{K}_{\mathbf{g}j}^{\pm} \cdot \mathbf{r}\right) \cdot \mathbf{e}_j. \tag{11}$$

The sign in $\mathbf{K}_{\mathbf{g}j}^{\pm}$ is given by the sign of z.

Explicit expressions for the Δ coefficients in (11) are readily obtained from (9) and (4)–(6) by invoking, for $k = p$ and $k = q$, the relation

$$\begin{aligned}
&\sum_m \exp(imdk_{||}) \left[\frac{(z + i(x - md))}{\left((x - md)^2 + z^2\right)^{1/2}}\right]^l \times H_l^{(1)}\left(k\left((x - md)^2 + z^2\right)^{1/2}\right) \\
&= 2(-k)^{-l} \times \sum_m (\gamma_m d)^{-1} \left[-\left(k_{||} + \frac{2\pi m}{d}\right) + i\, \gamma_m\, \mathrm{sgn}(z)\right]^l \times \exp\left[i\left(k_{||} + \frac{2\pi m}{d}\right)x + i\,|z|\,\gamma_m\right],
\end{aligned} \tag{12}$$

where $\gamma_m = [k^2 - (k_{||} + 2\pi m/d)^2]^{1/2}$ with $\mathrm{Im}\,\gamma_m \geq 0$. The relation (12) is valid for $z \neq 0$, and it can be verified using the Poisson summation formula.

2.2. Computation of the Expansion Coefficients $\mathbf{a^0}$*, the Matrices* Ω*, and the Matrices* T. An incident plane compressional wave $\mathbf{u}_{\mathrm{inc}}(\mathbf{r}) = \exp(i\, k_p\, \mathbf{e}_{\mathrm{inc}} \cdot \mathbf{r})\mathbf{e}_{\mathrm{inc}}$, where $\mathbf{e}_{\mathrm{inc}} = k_p^{-1}(p \sin\eta_{\mathrm{inc}}, \kappa, p\cos\eta_{\mathrm{inc}})$, can be expanded as

$$\mathbf{u}_{\mathrm{inc}}(\mathbf{r}) = -\sum_l \mathrm{i}^l\, \exp(-\mathrm{i}l\eta_{\mathrm{inc}})\, \mathbf{u}_{l\kappa}^{0L}(\mathbf{r}). \tag{13}$$

Noting that $\mathbf{u}_{\mathrm{inc}}(\mathbf{r}) = \nabla[\exp(i\, k_p\, \mathbf{e}_{\mathrm{inc}} \cdot \mathbf{r})]/ik_p$, this follows readily from the well-known Bessel function relation $\exp(i\,\gamma \sin\eta) = \sum_l J_l(\gamma)\, \exp(il\eta)$.

An incident plane shear wave of SV or SH type can be expanded by a superposition of two cases. The first case, $\mathbf{u}_{\mathrm{inc}}(\mathbf{r}) = \exp(i\, k_s\, \mathbf{e}_{\mathrm{inc}} \cdot \mathbf{r})\mathbf{e}_{\mathrm{inc}}^{\perp} = -(k_s\, q)^{-1} \nabla \times \{\nabla \times [\exp(i\, k_s\, \mathbf{e}_{\mathrm{inc}} \cdot \mathbf{r})\, \mathbf{e}_y]\}$ with $\mathbf{e}_{\mathrm{inc}} = k_s^{-1}(q\ \sin\ \eta_{\mathrm{inc}}, \kappa, q\cos\eta_{\mathrm{inc}})$ and $\mathbf{e}_{\mathrm{inc}}^{\perp} = k_s^{-1}(\kappa \sin\eta_{\mathrm{inc}}, -q, \kappa\cos\eta_{\mathrm{inc}})$, can be expanded as

$$\mathbf{u}_{\mathrm{inc}}(\mathbf{r}) = -\frac{k_s}{q} \sum_l i^l \exp(-\mathrm{i}l\eta_{\mathrm{inc}})\, \mathbf{u}_{l\kappa}^{0M}(\mathbf{r}). \tag{14}$$

The second case, $\mathbf{u}_{\mathrm{inc}}(\mathbf{r}) = \exp(i\, k_s\, \mathbf{e}_{\mathrm{inc}} \cdot \mathbf{r})\, \mathbf{e}_{\mathrm{inc}}^{\perp} = i/q\, \nabla \times [\exp(i\, k_s\, \mathbf{e}_{\mathrm{inc}} \cdot \mathbf{r})\mathbf{e}_y]$ with $\mathbf{e}_{\mathrm{inc}}$ as before and $\mathbf{e}_{\mathrm{inc}}^{\perp} = (\cos\eta_{\mathrm{inc}}, 0, -\sin\eta_{\mathrm{inc}})$, has the expansion

$$\mathbf{u}_{\mathrm{inc}}(\mathbf{r}) = \frac{k_s}{q} \sum_l i^{l+1} \exp(-il\eta_{\mathrm{inc}})\, \mathbf{u}_{l\kappa}^{0N}(\mathbf{r}). \tag{15}$$

The lattice translation matrix $\Omega(k_{||}d, pd, qd)$ can be determined by applying, for $k = p$ and $k = q$, the relation

$$\begin{aligned}
&\sum_{m \neq 0} \exp(imdk_\parallel) \left[\frac{(z + i(x - md))}{\left((x - md)^2 + z^2\right)^{1/2}}\right]^l \times \mathrm{H}_l^{(1)}\left(k\left((x - md)^2 + z^2\right)^{1/2}\right) \\
&= \sum_n \left[\frac{(z + ix)}{(x^2 + z^2)^{1/2}}\right]^n \Theta_{l-n}(k_\parallel d, kd) J_n(kr),
\end{aligned} \tag{16}$$

where the last sum is taken over all integers n and

$$\begin{aligned}
\Theta_l(k_\parallel d, kd) &= i^{-l} \sum_{m>0} \exp(imdk_\parallel) \mathrm{H}_l^{(1)}(mkd) \\
&\quad + i^l \sum_{m>0} \exp(-imdk_\parallel) \mathrm{H}_l^{(1)}(mkd).
\end{aligned} \tag{17}$$

This relation follows from the Graf addition theorem [20] for Bessel functions. The elements $\{\Omega_{l;l'}^{PP'}\}$ of the lattice translation matrix $\Omega(k_\parallel d, pd, qd)$ vanish unless $P = P'$. The remaining elements depend on l and l' through $|l - l'|$ only. Explicitly,

$$\begin{aligned}
\Omega_{l;l'}^{LL'} &= \Theta_{l-l'}(k_\parallel d, pd), \\
\Omega_{l;l'}^{MM'} &= \Omega_{l;l'}^{NN'} = \Theta_{l-l'}(k_{||} d, qd).
\end{aligned} \tag{18}$$

Moroz [21] has published a representation of lattice sums in terms of exponentially convergent series, which has been used in the present work for numerical evaluation of the Θ quantities defined in (17).

For a homogeneous cylindrical scatterer, the interior field and the exterior field can be expanded in cylindrical waves $\mathbf{u}_{l\kappa}^{0P}(\mathbf{r})$ and $\mathbf{u}_{l\kappa}^{0P}(\mathbf{r}), \mathbf{u}_{l\kappa}^{+P}(\mathbf{r})$, respectively. An equation system for the T-matrix elements $T = \{T_{l;l'}^{PP'}\}$, which depend on κ, is then readily obtained from the standard boundary conditions concerning continuity of displacement and traction at the cylinder surface. The scatterer as well as the host medium can be either fluid or solid. Because of the circular symmetry with a cylindrical scatterer, scattering only appears to the same l component ($l' = l$). Details concerning the case $\kappa = 0$, for which the P-SV ($P, P' \neq M$) and SH ($P = P' = M$) solutions decouple, are given by Mei et al. [9].

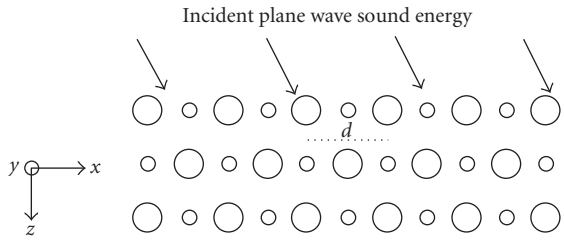

Figure 2: The configuration from Figure 1 is extended here, by allowing two types of cylindrical scatterers to appear in an alternating fashion at the same interface depth. The medium is periodic with period d in the x direction, and the cylinder axes are still parallel to the y-axis.

3. Different Types of Scatterers at the Same Interface

The LMS method is commonly applied for lattices with identical cylindrical scatterers within the same layer. As shown below, however, different types of scatterers within the same layer can also be accommodated. A similar extension for the restriction to in-plane wave propagation is made in Ivansson [22].

An illustration is given in Figure 2. Centered at the same z level, at each of the three scatterer interfaces, there are two types of cylindrical scatterers. Each scatterer interface is treated separately. Choosing coordinates appropriately, scatterers of the first type, with transition matrix T and scattered-field expansion coefficients denoted $\mathbf{b}^+$, appear at $\mathbf{R} = m \cdot (d, 0, 0)$, for integers m. Scatterers of the second type, with transition matrix U and scattered-field expansion coefficients denoted $\mathbf{c}^+$, appear at points $\mathbf{S}$ in between, that is, $\mathbf{S} = (m+1/2) \cdot (d, 0, 0)$. The reciprocal lattice vectors become $\mathbf{g} = (2\pi m/d, 0, 0)$, where m runs over the integers.

The generalization of the expression (9) for the scattered field becomes

$$\mathbf{u}_{\mathrm{sc}}(\mathbf{r}) = \sum_{Pl} \left[b_l^{+P} \sum_{\mathbf{R}} \exp(i\,\mathbf{k}_{\|} \cdot \mathbf{R}) \cdot \mathbf{u}_{l\kappa}^{+P}(\mathbf{r} - \mathbf{R}) \right] + \sum_{Pl} \left[c_l{}^{+P} \sum_{\mathbf{S}} \exp(i\,\mathbf{k}_{\|} \cdot \mathbf{S}) \cdot \mathbf{u}_{l\kappa}^{+P}(\mathbf{r} - \mathbf{S}) \right]. \tag{19}$$

It follows that

$$\mathbf{b}^+ = T \cdot (\mathbf{a}^0 + \mathbf{b}' + \mathbf{b}''), \qquad \mathbf{c}^+ = U \cdot (\mathbf{a}^0 + \mathbf{c}' + \mathbf{c}''), \tag{20}$$

where, for a scatterer of the first type at $\mathbf{R}$, $\exp(i\,\mathbf{k}_{\|} \cdot \mathbf{R})\mathbf{b}'$ and $\exp(i\,\mathbf{k}_{\|} \cdot \mathbf{R})\mathbf{b}''$ give the coefficients for expansion in regular cylindrical waves $\mathbf{u}_{l\kappa}^{0P}(\mathbf{r} - \mathbf{R})$ of the scattered field from all other scatterers of the first and the second types, respectively. The vectors $\mathbf{c}'$ and $\mathbf{c}''$ are defined analogously. For a scatterer of the second type at $\mathbf{S}$, $\exp(i\,\mathbf{k}_{\|} \cdot \mathbf{S})\mathbf{c}'$ and $\exp(\mathrm{i}\,\mathbf{k}_{||} \cdot \mathbf{S})\mathbf{c}''$ thus give the coefficients for expansion in regular cylindrical waves $\mathbf{u}_{l\kappa}{}^{0P}(\mathbf{r} - \mathbf{S})$ of the scattered field from all other scatterers of the second and the first types, respectively.

With $\Omega^0 = \Omega(k_{||}d, pd, qd)$, it follows that $\mathbf{b}' = \Omega^0 \cdot \mathbf{b}^+$ and $\mathbf{c}' = \Omega^0 \cdot \mathbf{c}^+$. For a certain matrix Ω^{dif}, to be determined, $\mathbf{b}'' = \Omega^{\mathrm{dif}} \cdot \mathbf{c}^+$ and $\mathbf{c}'' = \Omega^{\mathrm{dif}} \cdot \mathbf{b}^+$. The equation system for determination of $\mathbf{b}^+$ and $\mathbf{c}^+$ becomes

$$\begin{aligned} (\mathbf{I} - T \cdot \Omega^0) \cdot \mathbf{b}^+ - T \cdot \Omega^{\mathrm{dif}} \cdot \mathbf{c}^+ &= T \cdot \mathbf{a}^0, \\ -\,U \cdot \Omega^{\mathrm{dif}} \cdot \mathbf{b}^+ + (\mathbf{I} - U \cdot \Omega^0) \cdot \mathbf{c}^+ &= U \cdot \mathbf{a}^0. \end{aligned} \tag{21}$$

In order to form the R/T matrices, incident plane waves with different horizontal wavenumber vectors $\mathbf{k}_{\|} + \mathbf{g}_{\mathrm{inc}} = (k_{\|} + g_{\mathrm{inc}}, \kappa, 0)$ have to be considered, where g_{inc} belongs to the set $\{2\pi m/d\}$ providing the reciprocal lattice. Noting that the union of the scatterer positions is a small square lattice with period $d/2$, the following expression for Ω^{dif} as a difference of Ω matrices is directly obtained

$$\Omega^{\mathrm{dif}} = \Omega\left(\frac{(k_{||} + g_{\mathrm{inc}})d}{2}, \frac{pd}{2}, \frac{qd}{2}\right) - \Omega^0. \tag{22}$$

Only those $\mathbf{g}_{\mathrm{inc}}$ in $\{(2\pi m/d, 0, 0)\}$ for which m is even are reciprocal vectors for the small lattice with period $d/2$. Since a lattice translation matrix Ω is periodic in its first argument with period 2π, there will be two groups of $\mathbf{g}_{\mathrm{inc}}$ with different Ω^{dif} matrices according to (22). Specifically,

$$\Omega^{\mathrm{dif,even}} = \Omega\left(\frac{k_{||}d}{2}, \frac{pd}{2}, \frac{qd}{2}\right) - \Omega^0 \tag{23}$$

pertains to $\mathbf{g}_{\mathrm{inc}} = (2\pi m/d, 0, 0)$ with even m, and

$$\Omega^{\mathrm{dif,odd}} = \Omega\left(\frac{k_{||}d}{2} + \pi, \frac{pd}{2}, \frac{qd}{2}\right) - \Omega^0 \tag{24}$$

pertains to $\mathbf{g}_{\mathrm{inc}} = (2\pi m/d, 0, 0)$ with odd m.

The transformation of the expansion (19) to plane waves of the type (1) can be done separately for each of the $\mathbf{R}$ and $\mathbf{S}$ sums. In the latter case, the translation from the origin causes a sign change for some combinations of incident ($\mathbf{g}_{\mathrm{inc}}$) and scattered ($\mathbf{g}_{\mathrm{sc}}$) reciprocal lattice vectors. Specifically, with $\mathbf{g}_{\mathrm{inc}} = (2\pi m_{\mathrm{inc}}/d, 0, 0)$ and $\mathbf{g}_{\mathrm{sc}} = (2\pi m_{\mathrm{sc}}/d, 0, 0)$, the double sum corresponding to the one in (11) appears as

$$\mathbf{u}_{\mathrm{sc}}(\mathbf{r}) = \sum_{\mathbf{g}_{\mathrm{sc}}} \sum_{j=1,2,3} (-1)^{m_{\mathrm{inc}} - m_{\mathrm{sc}}} \Delta(d\mathbf{g}_{\mathrm{sc}}, j; k_{\|}d, \kappa d, pd, qd, \mathbf{c}^+) \times \exp\left(i\mathbf{K}_{\mathbf{g}_{\mathrm{sc}}j}^{\pm} \cdot \mathbf{r}\right) \cdot \mathbf{e}_j. \tag{25}$$

4. Designing 2D PC Slabs with a Transmission Gap

It is well known that band gaps can appear when scatterers with a large density are arranged periodically in a host with a small density. A particular 2D PC slab example with lead cylinders in epoxy was considered in Mei et al. [12]. The epoxy parameters were 2540 and 1159.817 m/s for the compressional- and shear-wave velocities, respectively, and 1.18 kg/dm^3 for the density. Corresponding lead material parameters were 2160 and 860.568 m/s, and 11.4 kg/dm^3.

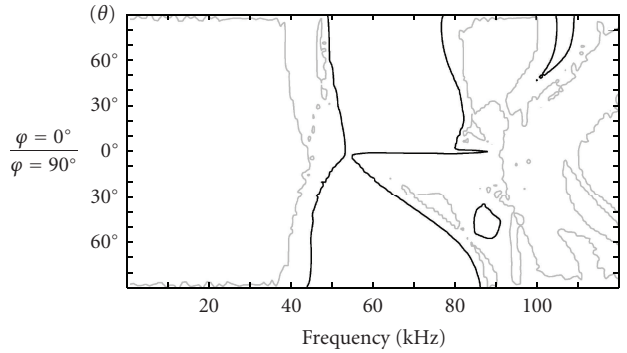

Figure 3: Contour plot of transmittance for a PC slab with lead cylinders in an epoxy host. Parameters of the slab are given in the text. The direction vector of the incident compressional wave is (sin θ cos φ, sin θ sin φ, cos θ). The black and gray contours are at -150 dB and -10 dB, respectively.

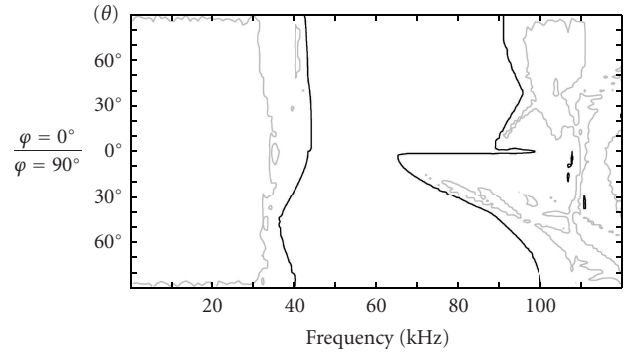

Figure 4: Contour plot of transmittance as in Figure 3 but for the optimized PC slab specified in Table 1.

Table 1: Specification of a PC slab that has been optimized by DE to produce small transmittance in the band 45–65 kHz. Corresponding transmittance results are shown in Figures 4 and 5.

Optimum	-163.0 dB
Scatterer compressional-wave velocity α	2995.6 m/s
Scatterer shear-wave velocity β	1200.0 m/s
Scatterer density ρ	14.000 kg/dm^3
Layer thickness h	13.292 mm
Largest scatterer radius $r_{\max}$	4.2702 mm
Smallest scatterer radius $r_{\min}$	4.2300 mm
Lattice period d	22.670 mm

The slab was formed by sixteen layers of lead cylinders, each with a radius of 3.584 mm, with a spacing between cylinder centers of 11.598 mm in the x as well as z directions, cf. Figure 1 where there are three layers. A band gap centered at about 60 kHz was found. (Dimensionless frequencies and distances were actually used in the paper, but a specialization is made here.)

Figure 3 is a contour plot of the transmittance, that is, time- (and space-) averaged transmitted energy flux relative to the incident one, up to 120 kHz. The vertical axis is for the angle θ, where the direction vector of the incident compressional plane wave is $(\sin\theta\cos\varphi, \sin\theta\sin\varphi, \cos\theta)$. In-plane and out-of-plane incidence angles are considered together in Figure 3, where the upper half with $\varphi = 0^\circ$ concerns incidence in the xz plane (in-plane propagation) and the lower half with $\varphi = 90^\circ$ concerns incidence in the yz plane. Only the first Brillouin zone is involved, since $k_x = \omega/\alpha \sin\theta \cos\varphi < 2\pi/d$ when α equals the epoxy compressional-wave velocity 2540 m/s, $d = 11.598$ mm, and the frequency is less than $\alpha/d = 219$ kHz. Of course, the band gap from Mei et al. [12], at about 60 kHz, shows up clearly in this kind of plot. One might wonder how the geometrical and/or material parameters of the slab should be modified to achieve a prescribed desired change of the appearance of the gap.

Global optimization methods can be used to design PC slabs with desirable properties. Simulated annealing, genetic algorithms and differential evolution (DE) are three kinds of such methods, that have become popular during the last fifteen years. DE, to be applied here, is related to genetic algorithms, but the parameters are not encoded in bit strings, and genetic operators such as crossover and mutation are replaced by algebraic operators [16].

As a very simple example, to try to position and widen the gap in Figure 3, an objective function for DE minimization is specified as the maximum transmittance in the frequency band 45–65 kHz when the incidence angle θ is varied between 0° and 20° for the two azimuthal angles $\varphi = 0^\circ$ (in-plane propagation in the xz plane) and $\varphi = 90^\circ$ (propagation in the yz plane). A configuration with cylinders of two alternating sizes is allowed, as depicted in Figure 2. Still, the slab is formed by sixteen layers of cylinders. The following seven parameters are varied within the indicated search space: scatterer compressional-wave velocity α [1500 m/s $\le \alpha \le$ 3000 m/s], scatterer shear-wave velocity β [650 m/s $\le \beta \le$ 1200 m/s], scatterer density ρ [7 kg/dm^3 $\le \rho \le$ 14 kg/dm^3], layer thickness h [$8 \le h \le 16$ mm], the largest scatterer radius $r_{\max}$ [$0.225\,h \le r_{\max} \le 0.4\,h$], the smallest scatterer radius $r_{\min}$ [$0.45\,r_{\max} \le r_{\min} \le r_{\max}$], the lattice period d[$8(r_{\max} + r_{\min})/3 \le d \le 4\,(r_{\max} + r_{\min})$]. The layer thickness h is the z distance between subsequent scatterer interfaces (cf. Figure 2).

Table 1 shows the optimum obtained with DE, along with corresponding parameter values. A reduction of the transmitted field with more than 160 dB is achieved throughout the band 45–65 kHz and throughout the solid angle intervals $0^\circ < \theta < 20^\circ$ for $\varphi = 0^\circ$, $\varphi = 90^\circ$ for the direction of incidence. High-velocity high-density cylinders seem preferable, since the lead velocities and density are all increased to values close to the upper ends of the corresponding search intervals. In this case, as large as possible values of α, β, and ρ could in fact have been fixed from the start. Moreover, the cylinders are almost as densely packed horizontally as allowed by the search interval for d. Hence, the optimization could in fact have been simplified considerably. With only a few free parameters, a complete search, for example, can be a feasible alternative.

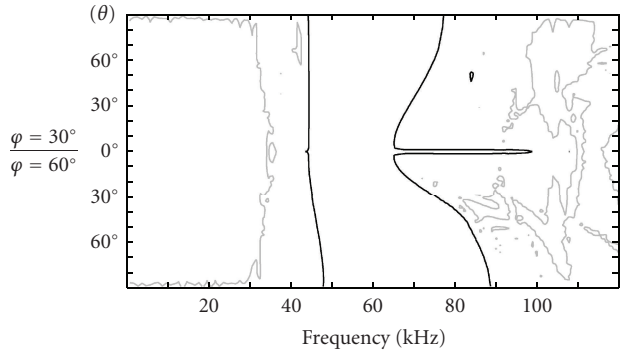

Figure 5: Contour plot of transmittance for the optimized PC slab specified in Table 1. The difference to Figure 4 is that two other φ angles are considered for the direction of the incident compressional wave.

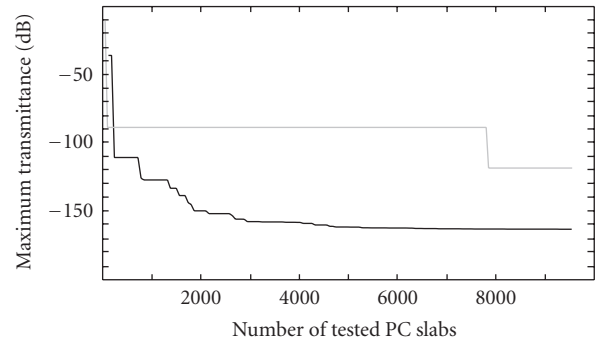

Figure 6: Evolution of the maximum transmittance with the number of tested parameter combinations for the DE optimization leading to the PC slab specified in Table 1. A corresponding curve for a brute force Monte Carlo method is also included (gray).

Compared to Figure 3, the contour plot in Figure 4 of the transmittance for the optimized PC slab shows a band gap around 60 kHz that has become significantly wider and also deeper. The allowed increases of α, β, ρ, and $(r_{\max} + r_{\min})/d$ are certainly essential for producing this effect. Variation of h, $r_{\max}$, and $r_{\min}$ is needed to position the band gap at the desired frequency interval. Although the optimization was performed with the restriction $0^\circ < \theta < 20^\circ$, small transmittance is apparently achieved for all angles θ ($0^\circ < \theta < 90^\circ$).

It turns out that the transmittance for the optimized PC slab remains small within the 45–65 kHz band for all out-of-plane incidence angles (an "absolute" band gap). Figure 5 shows the transmittance in the same way as Figure 4, but for $\varphi = 0^\circ$ changed to $\varphi = 30^\circ$ and $\varphi = 90^\circ$ changed to $\varphi = 60^\circ$. The upper and lower halves exhibit increased symmetry, since the φ angles involved are closer to one another.

Apparently, the optimized PC slab has large transmittance below about 30 kHz and there are regions with large transmittance above 80 kHz as well. The band gap with small transmittance extends to higher frequencies, than those in the band 45–65 kHz, for plane-wave incidence directions with either large θ or small φ.

The efficacy of the DE technique can be illustrated by showing the decrease of the maximum transmittance within the specified frequency/angle region as the number of tested parameter settings for the PC slab evolves. Figure 6 shows this decrease for the example from Figure 4. A comparison to the much less efficient MonteCarlo method, with random selection of parameters from the search space, is included. The low efficiency of the MonteCarlo approach shows that the desired PC slabs with small transmittance only appear in a small portion of the search space. For example, only about 0.15% of the random slab selections had a maximum transmittance below −20 dB within the specified frequency/angle region. About 0.01% had a maximum transmittance below −100 dB.

The difference between $r_{\max}$ and $r_{\min}$ in Table 1 is rather small. Optimization was also tried with all cylinders of exactly the same radius, as in Figure 1. The obtained optimum, with cylinders of radius 4.2503 mm and slightly modified values for the other parameters, was almost as good as the one presented in Table 1. The advantages with cylinders of different sizes are expected to be more significant in more complicated filtering cases, involving, for example, more than one frequency band.

5. Conclusions

The layer multiple-scattering (LMS) method is a fast semi-analytical technique for computing scattering from layers including periodic scatterer lattices. For the 2D case with cylindrical scatterers and any solid angle direction of an incident plane wave, an extension has been made to scatterer lattices with cylindrical scatterers of two different sizes in the same horizontal plane.

Global optimization methods from inverse theory are useful for designing PC slabs with desirable properties. A differential evolution algorithm has been applied here to position and widen an "absolute" band gap for a certain 2D PC slab. Although only limited angle intervals for the direction of incidence were included for the optimization, small transmittance was achieved for all solid angles specifying the direction of the incident wave.

The possibility to include cylindrical scatterers of two different sizes in the same horizontal plane provides an additional degree of freedom that can be useful for PC design purposes. In the presented example, with its specification of objective function and search intervals for the parameters, however, the difference between the optimal cylinder radii was rather small and the improvement only marginal. The additional flexibility is expected to be more important in more complicated filtering applications. For example, specified regions in frequency-angle space with large transmittance could be desired in addition to specified regions with small transmittance.

Acknowledgment

Alexander Moroz kindly provided his Fortran routine for calculation of lattice sums.

References

[1] T. Miyashita, "Sonic crystals and sonic wave-guides," *Measurement Science and Technology*, vol. 16, no. 5, pp. R47–R63, 2005.

[2] N. Papanikolaou, R. Zeller, and P. H. Dederichs, "Conceptual improvements of the KKR method," *Journal of Physics: Condensed Matter*, vol. 14, no. 11, pp. 2799–2823, 2002.

[3] I. E. Psarobas, N. Stefanou, and A. Modinos, "Scattering of elastic waves by periodic arrays of spherical bodies," *Physical Review B*, vol. 62, no. 1, pp. 278–291, 2000.

[4] Z. Liu, C. T. Chan, P. Sheng, A. L. Goertzen, and J. H. Page, "Elastic wave scattering by periodic structures of spherical objects: theory and experiment," *Physical Review B*, vol. 62, no. 4, pp. 2446–2457, 2000.

[5] M. Sigalas, M. S. Kushwaha, E. N. Economou, M. Kafesaki, I. E. Psarobas, and W. Steurer, "Classical vibrational modes in phononic lattices: theory and experiment," *Zeitschrift für Kristallographie*, vol. 220, no. 9-10, pp. 765–809, 2005.

[6] R. Sainidou, N. Stefanou, I. E. Psarobas, and A. Modinos, "The layer multiple-scattering method applied to phononic crystals," *Zeitschrift für Kristallographie*, vol. 220, no. 9-10, pp. 848–858, 2005.

[7] S. B. Platts, N. V. Movchan, R. C. McPhedran, and A. B. Movchan, "Two-dimensional phononic crystals and scattering of elastic waves by an array of voids," *Proceedings of the Royal Society of London A*, vol. 458, no. 2026, pp. 2327–2347, 2002.

[8] S. B. Platts, N. V. Movchan, R. C. McPhedran, and A. B. Movchan, "Transmission and polarization of elastic waves in irregular structures," *Transactions of the ASME*, vol. 125, no. 1, pp. 2–6, 2003.

[9] J. Mei, Z. Liu, J. Shi, and D. Tian, "Theory for elastic wave scattering by a two-dimensional periodic array of cylinders: an ideal approach for band-structure calculations," *Physical Review B*, vol. 67, Article ID 245107, 7 pages, 2003.

[10] C. Qiu, Z. Liu, J. Mei, and M. Ke, "The layer multiple-scattering method for calculating transmission coefficients of 2D phononic crystals," *Solid State Communications*, vol. 134, no. 11, pp. 765–770, 2005.

[11] S. Robert, J.-M. Conoir, and H. Franklin, "Propagation of elastic waves through two-dimensional lattices of cylindrical empty or water-filled inclusions in an aluminum matrix," *Ultrasonics*, vol. 45, no. 1–4, pp. 178–187, 2006.

[12] J. Mei, Z. Liu, and C. Qiu, "Multiple-scattering theory for out-of-plane propagation of elastic waves in two-dimensional phononic crystals," *Journal of Physics: Condensed Matter*, vol. 17, no. 25, pp. 3735–3757, 2005.

[13] M. Wilm, A. Khelif, S. Ballandras, V. Laude, and B. Djafari-Rouhani, "Out-of-plane propagation of elastic waves in two-dimensional phononic band-gap materials," *Physical Review E*, vol. 67, no. 6, Article ID 065602, 4 pages, 2003.

[14] S. Guenneau, C. G. Poulton, and A. B. Movchan, "Oblique propagation of electromagnetic and elastic waves for an array of cylindrical fibres," *Proceedings of the Royal Society of London A*, vol. 459, no. 2037, pp. 2215–2263, 2003.

[15] S. M. Ivansson, "Numerical design of Alberich anechoic coatings with superellipsoidal cavities of mixed sizes," *Journal of the Acoustical Society of America*, vol. 124, no. 4, pp. 1974–1984, 2008.

[16] K. Price, R. Storn, and J. Lampinen, *Differential Evolution—A Practical Approach to Global Optimization*, Springer, New York, NY, USA, 2005.

[17] S. M. Ivansson, "Sound absorption by viscoelastic coatings with periodically distributed cavities," *Journal of the Acoustical Society of America*, vol. 119, no. 6, pp. 3558–3567, 2006.

[18] J. B. Pendry, *Low Energy Electron Diffraction*, Academic Press, New York, NY, USA, 1974.

[19] B. L. N. Kennett, *Seismic Wave Propagation in Stratified Media*, Cambridge University Press, Cambridge, UK, 1983.

[20] M. Abramowitz and I. A. Stegun, *Handbook of Mathematical Functions*, National Bureau of Standards, 1965.

[21] A. Moroz, "Exponentially convergent lattice sums," *Optics Letters*, vol. 26, no. 15, pp. 1119–1121, 2001.

[22] S. M. Ivansson, "Extended layer multiple-scattering and global optimization techniques for 2D phononic crystal insulator design," in *Photonics Research Developments*, V. P. Nilsson, Ed., chapter 7, pp. 225–245, Nova, 2008.